POLITECNICO DI MILANO
DEPARTMENT OF ENERGY
DOCTOR PROGRAM IN SCIENCE AND TECHNOLOGY
OF ENERGY AND NUCLEAR

A STUDY OF GASEOUS TRANSVERSE INJECTION AND MIXING PROCESS IN A SIMULATED ENGINE INTAKE PORT

Doctor Dissertation of:
Hua WANG

Supervisor:
Prof. Aldo COGHE

Tutor:
Prof. Angelo ONORATI

The Chair of the Doctor Program:
Prof. Carlo BOTTANI

2013 – XXV cycle

ABSTRACT

The flow field resulting from injecting a gas jet into a crossflow confined in a narrow square duct has been studied under steady regime using both experimental and numerical methods. A transparent duct is built, intended to simulate the intake port of an internal combustion engine fueled by gaseous mixture, and the jet is issued from a round nozzle. Schlieren imaging, laser Doppler velocimetry (LDV) have been applied for the experimental study as well as hot wire anemometry (HWA).

The schlieren images show that the relative small size of the duct would confine the development of the transverse jet, and the interaction among jet and sidewalls strongly influences the mixing process between jet and crossflow. The mean velocity and turbulence fields have been studied in detail through LDV and HWA measurements, at both the center plane and several cross sections. Several important phenomena have been identified with these techniques and analyzed in depth, including the well-known counter rotating vortex pair (CVP), which starts to appear at the jet exit section and persists far downstream contributing to enhancing mixing process.

In addition, jets of different gases have been investigated with various injection orientations, aiming to fully understand the behaviors of transverse jet and the mixing process in the simulated intake port under wide practical conditions. Particularly, the jet injection against crossflow has been found favorable in this study. The results show that the injection direction can influence the flow field remarkably, while the effect of injected gas is negligible, when the appropriate scaling is applied.

Moreover, a numerical study has been performed as well with FLUENT, which shows well agreement with the experimental results acquired. The numerical results could

present the concentration field, and consequently directly show the mixing process between the jet and the crossflow. Finally, a detailed description of the flow field inside a model intake port of an engine fueled with gaseous fuel is provided by the presented study and can be the basis for future comparison with computations.

ACKNOWLEDGEMENTS

I am grateful to my supervisor, Professor Aldo Coghe, for making this research possible. His patience and support for my work and ideas are appreciated. I also thank him for his constant help on my study and life in Milan.

In addition, I acknowledge Professor Lucio Araneo, for his guide on the experimental set up as well as data processing. Professionally, I am thankful for his insights into the fuel injection as well as optical diagnostics techniques.

I would also like to thank the help of Professor Fabio Cozzi, and other kind colleges working in the department of energy, Politecnico di Milano.

Finally, I thank my family, whose support is always appreciated.

CONTENT

LIST OF FIGURES

LIST OF TABLES

CHAPTER 1

INTRODUCTION

1.1 Motivations

Transverse injection into crossflow has been studied over many years, due to its great relevance to many engineering applications, particularly in energy and propulsion systems, as a consequence of the near field enhancement of the entrainment of crossflow and superior molecular mixing, when compared with the free jet issuing into quiescent surroundings or co-flow jet [1]. Examples of application can be found in aeronautics, including V/STOL aerodynamics, turbine blade cooling, fuel injection, hot gases cooling in industrial burners or gas turbine combustors, and many other engineering systems. Recent applications in automotive industry include port fuel injection (PFI) for internal combustion engines fueled with non-conventional gaseous fuels, such as methane, hydrogen, CH_4/H_2 mixtures or synthetic fuels. PFI of gaseous fuels has advantages in air-fuel mixing compared with in-cylinder direct injection, since it has been proved that in-cylinder direct injection may be affected by incomplete mixing due to the short available time in the speed range 1000-5000 rpm [2]. In addition, in most applications to date natural gas is injected in the intake manifold [3].

Despite the large amount of studies covering the various aspects of transverse injection, few experimental investigations have reported quantitative velocity measurements or were concerned with applications in as narrow duct at high level of turbulence, i.e. fuel-air mixing in the intake port of PFI gaseous fueled internal combustion engines. In addition, internal combustion engine fueled with gaseous fuel need to be further

improved urgently to achieve same performance as those engines fueled by gasoline or diesel at various conditions. Thus it is essential to carry out investigations of transverse injection in narrow duct, to understand its behavior under different conditions, and to provide fundamental knowledge to optimize PFI internal combustion engines fueled by gaseous fuel, particular the air-fuel mixing process inside intake manifold.

1.2 Previous Studies

The widespread applications of transverse jet have led over the past 50+ years to experimental, theoretical, and numerical examinations of this fundamental flow field, with and without combustion reaction, and with single or multi-phase flow. Earliest studies focused on jet main trajectory and structural features [4], the source and evolution of vortical structures [1, 5-9], crossflow entrainment and jet-crossflow turbulent mixing [1, 6, 10, 11], the concentration field [12]. For steady jet, it is well known that the jet's structure and trajectory depend on the jet-to-crossflow momentum flux ratio, crossflow boundary layer thickness, while jet temperature and Reynolds number have limited impact, at least in the near field and at high momentum flux ratios [4]. As a consequence, the jet trajectory of a turbulent jet issuing transversely into a uniform, steady crossflow can be described by a single function, when the space coordinates are normalized by the momentum flux ratio [1].

Numerous experimental studies have been carried out by using various flow visualization methods or hot-wire techniques and revealed that several complex phenomena are associated even with the simple case of steady injection into a uniform crossflow [4, 5, 7, 13]. Different vortical structures have been observed by a number of investigations and four types of coherent structure have been discerned and analyzed. In particular, a counter rotating vortex pair (CVP) occurs as a result of the interaction between the jet and the crossflow, as well as the roll-up of vorticity at the jet shear layer [1, 7, 8]. The CVP originates in the near field and becomes the dominant flow feature after the jet has turned in the crossflow direction [6, 8, 12]. Also the presence of the CVP, which does not exist in the free jet, favors entrainment and mixing of the crossflow by secondary effects [1, 14].

In the majority of reported experimental studies, the CVP has been observed through hot-wire measurements [6, 15], which are nonetheless questionable in a three

dimensional high turbulent flow, or by flow visualizations in a water channel, generally for high momentum flux ratios. More recent experiments investigated the near field characteristics of transverse jets at moderate velocity ratios in a water tunnel by particle image velocimetry (PIV) [14, 16], the scalar mixing and two-dimensional velocity field with combined planar laser induced fluorescence (PLIF) and PIV [17], as well as the CVP by stereoscopic PIV in a wind tunnel [18]. However, the mechanism of formation of the CVP remains poorly understood.

Most of the reported experiments have been performed in large wind tunnels, when the effect of wall confinement on the jet's trajectory is insignificant and only the boundary layer on the wall from which the jet issues affects the vortical structures in the wake of the jet. Jets in confined turbulent crossflow have received considerably less attention and only few experiments have been performed in a narrow duct [19, 20], and generally in water flows. Moreover, most investigations considered jets and crossflows having low turbulence and thin boundary layers, while most practical applications deal with turbulent inlet conditions.

In another side, gaseous fuels such as methane and hydrogen have attracted attentions from engineers and scientist for years, and they are presumed as ideal alternative fuel for traditional petrol fuel [21, 22]. Although various approaches has been applied to improve the performance of gaseous fueled internal combustion engines based on numerous studies with both experimental and numerical methods on this specified engine, few research has concerned the fuel-air mixing before the mixture enters into the cylinder in the intake port of a PFI gaseous fueled engine.

1.3 Objectives and Investigation Methods

The objective of the present study is to provide quantitative data on the mean flow and turbulence of gas jets issued into a confined cross-stream, simulating typical conditions of gaseous fuel injection in the intake manifold of internal combustion engines. The analysis is motivated by the lack of both the experimental and numerical data in such flow conditions. Specifically, we report on gas injection into a steady crossflow confined into a narrow transparent duct which provides the possibility for the application of optical diagnostic techniques, such as schlieren imaging and laser Doppler velocimetry (LDV).

Schlieren imaging has been applied to observe the macro structure of jet and its interaction with the walls, while mean and fluctuation velocity have been measured by LDV, at several cross-sections downstream of the injection port. HWA has been conducted additionally to understand the mixing level at the far downstream. Finally, a RANS (Reynolds averaged Navier-Strokes) model has been built to understand the mixing process directly via the fuel concentration distribution in the flow field. With those investigation methods, the following targets are supposed to be reached:

- To understand the flow pattern of transverse jet in a confined duct;
- To understand the fuel air mixing process in the simulated intake port for PFI internal combustion engine fueled by gaseous fuel;
- To explain the physical phenomenon that control the fuel air mixing process in the simulated intake port for PFI internal combustion engine fueled by gaseous fuel.

The results presented in this study are expected to provide valuable reference information to the optimization of air-fuel mixing strategy for PFI gaseous internal combustion engine.

1.4 About This Thesis

As mentioned in previous section, the work presented here was targeted to understand the behavior of transverse jet in a confined narrow duct, under different conditions, and to provide fundamental knowledge to optimize PFI internal combustion engines fueled by gaseous fuel, particular the air-fuel mixing process inside intake manifold. In this sense, the current work explains how those techniques (both experimental and numerical) have been applied, improved and coupled in order to determine and explain the complex flow phenomena inside the narrow duct where the gas jet is transversely injected. The structure of this thesis is followed:

First, a review of literature is given in the following chapter 2, trying to explain the general phenomena, previous achievements in this field as well as limitations.

After that, all the experimental facilities used are described in chapter 3, including the principle of each experimental technique.

Chapter 4 presents the experiment results obtained from schlieren imaging experiment and the LDV experiment results is given in chapter 5, followed by the experiment results of HWA measurements, given in chapter 6. Based on these three experimental measurements, a detailed description of the flow field inside a model intake port of an engine fueled with gaseous fuel is provided.

Then in chapter 7, a numerical study has been attempted. The numerical model is firstly validated by the experimental results, and then tries to predict those flow characteristics which are difficult measured with experimental methods, such as the gas concentration.

Finally, the main conclusions of the work are outlined and future works are proposed.

CHAPTER 2

LITERATURE REVIEW

2.1 Overview of Non-reactive Jet Structure

The flow field associated with the transverse jet, or jet injected normally into crossflow, is one that has been extensively investigated, via experimental, theoretical, as well as computational approaches, for its widespread applications, particularly in energy and propulsion systems, which has been mentioned in the first section. A sketch indicating the dominant flow and vortical structures associated with the jet in crossflow is shown in Fig. 2.1-1.

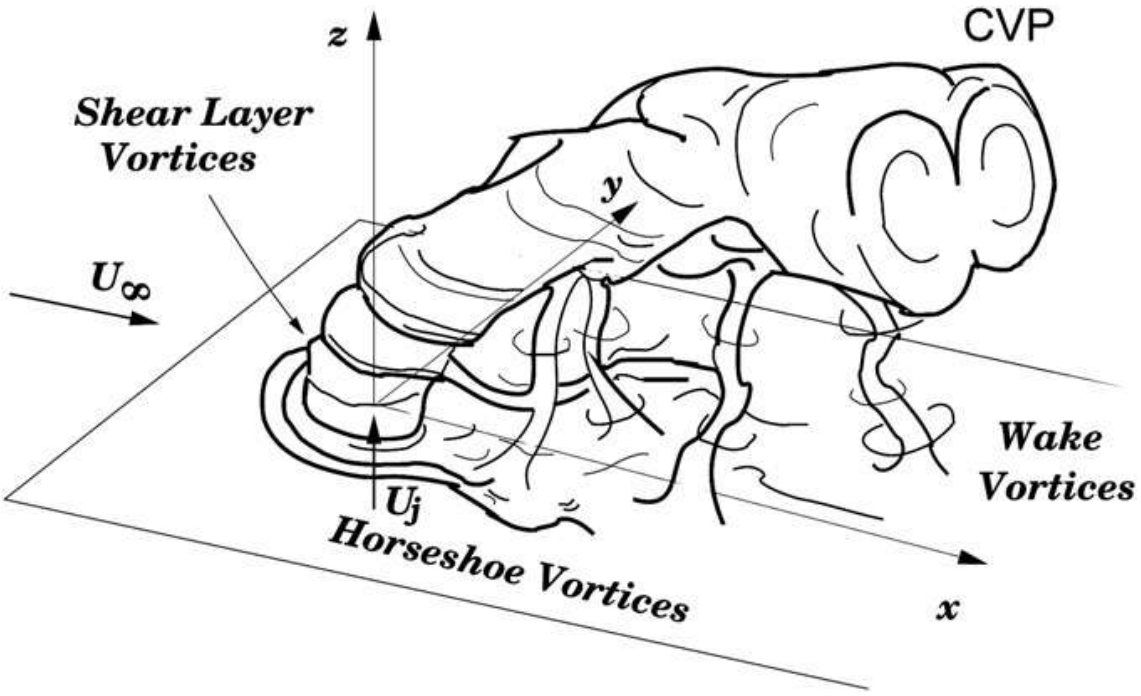

Figure 2.1-1 Schematic of the transverse jet, introduced flush with respect to the injection wall, and relevant vortical structures and axes. Crossflow U_∞ is the positive x-direction. (adapted from [7])

As showed in Fig. 2.1-1, the transverse jet typically consists of a jet of mean velocity U_j issuing into a crossflow of velocity U_∞ (U_{cf} in the rest of this thesis), with different injection angle, usually normal to the mean flow. The jet can exit either flush from an orifice embedded within a wall, as shown in Fig. 2.1-1, or from an elevated pipe or nozzle. Apparently, the transverse jet is a more complicated flow field than the free jet in quiescent surroundings due to its interaction with the crossflow and, for the case of the flush jet in crossflow, interaction of the jet with the wall boundary layer. For steady jet, it is well known that the jet's structure and trajectory depend on the jet-to-crossflow momentum flux ratio, crossflow boundary layer thickness, while jet temperature and Reynolds number have limited impact, at least in the near field and at high momentum ratios [4]. The jet-to-crossflow momentum flux ratio R is defined as:

$$R = \sqrt{\rho_j {U_j}^2 / \rho_{cf} {U_{cf}}^2} \qquad \text{(Eq. 2-1)}$$

Where the subscript j and cf refer jet and crossflow respectively. Other parameters used to characterize this flow field are:

Jet to crossflow velocity ratio:

$$R_v = U_j/U_{cf} \qquad \text{(Eq. 2-2)}$$

The jet Reynolds number:

$$Re_j = U_j D/\upsilon_j \qquad \text{(Eq. 2-3)}$$

And the crossflow Reynolds number:

$$Re_{cf} = U_{cf} D/\upsilon_{cf} \qquad \text{(Eq. 2-4)}$$

Where D is the jet nozzle diameter, or, for a non-circular cross section, the hydraulic diameter. In the limit of isodensity jets in crossflow, $R=R_v$.

As a consequence, the jet trajectory of a turbulent jet issuing transversely into a uniform, steady crossflow can be described by a single function, when the space coordinates are normalized by the momentum flux ratio [1]. Particularly, trajectories of the local jet velocity maxima, the local temperature maxima or minima, the local concentration maxima, etc, have been characterized in terms of R or R_v based on scaling arguments [12, 23, 24]. An extensive discussion on historically implemented transverse jet trajectory correlations may be found in the review article by Margason [23]. For example, characteristic incompressible transverse jet velocity centerline trajectories are often scaled using the formula:

$$z/RD = A(x/RD)^m \qquad \text{(Eq. 2-5)}$$

Where x and z are the downstream and transverse spatial coordinates of the jet, defined in Figure 2.1-1, and A and m are constants. The experimentally determined value of m is typically of the order 0.28, with A of the order of 2.0 for a jet emanating from a pipe extending into the crossflow in the range $5 \leq R \leq 35$ [25]. For a jet injected from a converging nozzle flush with respect to the crossflow, in the range $5 \leq R \leq 25$, Smith and Mungal in [12] indicate values of A=1.5 and m=0.27 for a closer fit to trajectory data. Similarity arguments made by Hasselbrink and Mungal [24], based on the ideas of Broadwell and Breidenthal [26], suggest that near field trajectories for the transverse jet should have m=1/2 scaling, while the far field should be represented by m=1/3. Differences between nearfield and far field trajectory scaling, based on loci of velocity maxima, are also observed in experiments by Su and Mungal [17] for the transverse jet created by a pipe flow protruding from the injection wall.

Fig. 2.1-1 also shows that the fundamental dynamics of transverse jet are dominated by a complex, inter-related set of vortex systems. The most prominent vortex structures is the counter-rotating vortex pair (CVP), which is supposed to be the result of the interaction between the jet and the crossflow, as well as the roll-up of vorticity at the jet shear layer [1, 7, 8]. This CVP originates in the near field and becomes the dominant flow feature after the jet has turned in the crossflow direction [6, 8, and 12]. As introduced in previous chapter, the presence of the CVP, which does not exist in the free jet, is found to favor the entrainment and mixing of the crossflow by secondary effects [1, 14].

For the transverse jet injected flush from a wall, there are additionally horseshoe vortices[27, 28], which form in the plane of the injection wall and surround the upstream portion of the jet, and upright wake vortices [7], which are thought to be initiated within the wall boundary layer and to evolve periodically. These two vortices, combined with CVP and shear layer vortices, have been studied extensively and all proved to play important roles in the development of flow field and cross flow entrainment. Some of these studies will be elaborated in next sections.

A detail literature review on the reported study of jet into crossflow will be presented below. The main features of jet into crossflow will be explained in detail by the results and relative analysis of various experiment studies, followed by numerical studies, which provide useful explanations to those complex phenomena found in experimental studies. Finally, different control strategies proposed for various application of jet into crossflow will be introduced and discussed briefly, including their implementation on internal combustion engines.

2.2 Experimental Study

The earliest experiment record of the jet into a crossflow problem may be that of Dobson [29]. The purpose of that report, however, was not to specifically study the transverse jet. Instead, smoke trails from a factory chimney in a crosswind were used to estimate the turbulence “eddy conductivity” in the atmosphere. Bosenquet and Pearson [30] studied the transverse jet with regard to the spread of emissions from chimneys. After nearly one century has been passed since Dobson’s observation, numerous experimental studies have been carried out by using various flow visualization methods [4, 7, 8, 12-14, 19, 20,

31-36], flow velocity field [4, 7, 8, 14, 16-18, 20, 32, 35-45], or concentration field [12, 14, 17, 19, 20], measurements methods. These experiments have been conducted either in wind tunnels [4, 7, 8, 12, 17, 18, 31, 32, 34-41, 43-45], or water tunnels [8, 13, 14, 16, 19, 20, 33, 42], and all of them revealed that several complex phenomena are associated even with the simple case of steady injection into a uniform crossflow. Here only the literatures after 1980s are presented, nonetheless, review of early experimental studies can be found in [8, 46].

2.2.1 Flow Visualization

Despite the focus on the macro structures or jet trajectory from early research, those vortex structures existing in the flow field introduced by transverse injection of a jet into cross flow are concerned in nearly all of the reported studies, which has been introduced briefly in previous section. Among these studies, flow visualization is extremely useful in confirming the existence of large structures in the flow and in revealing some more details of their behavior [4]. Different methods have been attempted, including capture the Mie scattering image from seeding into the jet with smoke [7, 8, 31, 32, 35, 36], oil droplets [8], or reactive particles [34], for the study in the wind tunnels, and releasing dye at various strategic locations in the water tunnels [8, 13, 33].

One pioneering study on structural features resulting from the interaction of jet issuing transversely into a cross flow based on flow visualization in wind tunnel was done by Fric and Roshko [7]. A. Large jet-to-crossflow velocity range, from 2 to 10, was investigated at crossflow Reynolds number from 3800 to 11400. Photographs or shear layer vortex and horseshow vortex system were presented and analyzed briefly. In particular, the origin and formation of the vortices in the wake were described by them, which are most pronounced when R is around 4, and found to be not shed from the jet but are formed from vorticity which originates in the boundary layer of the crossflow wall. They conclude that the formation process begins just downstream and to either side of the jet, with separation of the crossflow-wall boundary layer in the adverse pressure gradient which is imposed on it by the external flow, because the latter does not separate from the jet but closely around it. The ‘separation event’ on the crossflow wall occurs alternately on each side of the jet and results in eruptions (more or less periodically) of boundary-layer fluid and

vorticity. This tornado-like vortex which is formed has its base in the boundary layer while its other end is entrained by the jet.

Similar results have been found in the study of Kelso and Lim [8], which presented images from flow visualization in both water channel and wind tunnel, combined with experimental data from flying-hot-wire measurements. Many vortex systems are found in those images, to be contained in the flow field again, all of which are somehow connected. They interpreted the major roll-up process of the jet shear layer based on the image of dye released at different location of jet nozzle or upstream of crossflow. The large-scale vortex ring-like roll-up, similar to that of a free jet, was described as well. And their results also show the mean reorientation of the shear layer vorticity which leads to (or contributes to) the formation of the CVP. This interpretation agrees well with mechanism proposed by Andreopoulos [4], who visualized the flow by introducing a fog of paraffin oil droplets into the jet. Evidences of horseshoe vortex and wake vortex were also presented and explained. They concluded that wake vortex come from the vorticity generated at the flat wall, which confirms the results of Fric and Roshko [7], and this vorticity somehow links up with the wall vortices and the CVP. Moreover, they believe that horsehoe vortex system seems to play only a minor role in the overall structure, proved by the mechanism provided by Doligalski et al. [47]. In the end, they have attempted to summarize the relationship between the various phenomena in the Fig. 2.2-1, which shows a tentative sketch in (*R*, *Re*)-space.

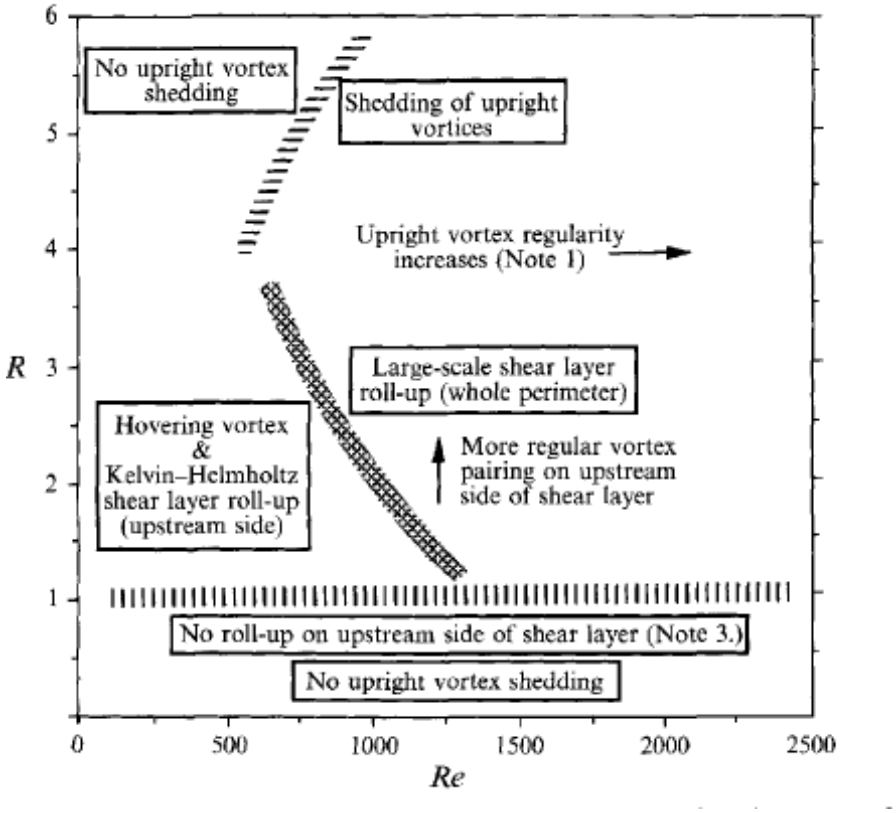

Figure 2.2-1 Graphical summary of jet in cross-flow phenomena, showing the range of phenomena and the R, Re-ranges for which they occur. The precise shapes of the zone boundaries are unknown. Note 1: most regular upright vortex shedding at R ≈4; Note 2: vortex breakdown at R>3. (adapted from [8])

Flow visualization of jet in cross flow has been carried out in water channel as well by Morton and Ibbetson [33], Lim and New [13]. Morton and Ibbeston studied the entrainment of crossflow into the jet and provide some explanation of mixing mechanism, and proved again that wake vortices are generated from crossflow boundary layer. Lim and New's research focus on the large scale vortex structures. Based on their observation, Lim and New proposed a model which explains the contribution of shear layer vortex loop to CVP. Their results show that as soon as the cylindrical vortex sheet of the jet emerged from the nozzle, it immediately folded up on its edges to form a CVP, which is consistent with the experimental observation of Kelso [8]. Combined their observation with previous study, they attempted to interpret the finally developed vortex structures in the flow field, which are shown in Fig. 2.2-2.

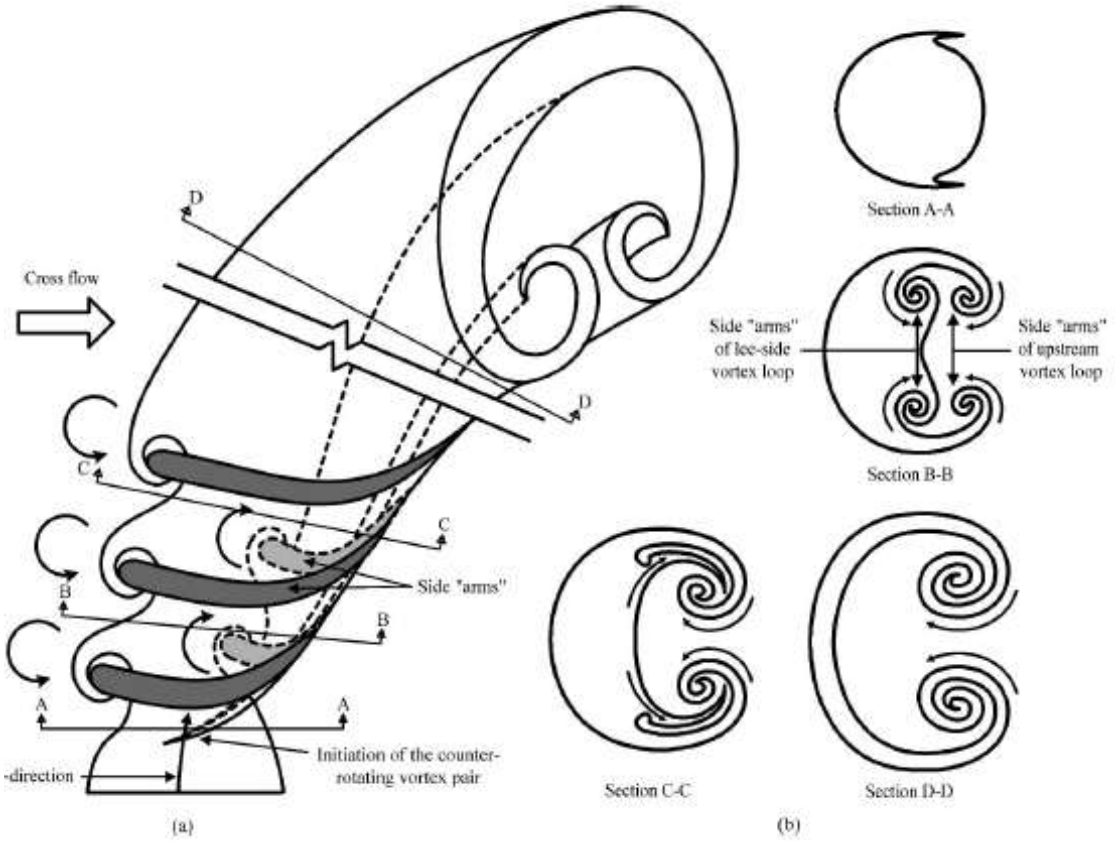

Figure 2.2-2 Lim and New's interpretation of the finally developed vortex structures of jet in crossflow (a) the sketch shows how the 'arms' of both the upstream and the lee-side vortex loops are merged with the counter-rotating vortex pair. (b) Cross sectional views of (a) taken at various streamwise distance.

2.2.2 Hot Wire Anemometry

Hot wire anemometry (HWA) is another common method to study the jet into cross flow [4, 7, 8, 31, 35, 36, 38, 41, 43, 44], especially the mean velocity and turbulence field, despite its uncertainty in a three dimensional high turbulent flow. Early studies use this technique to reveal complex vortical structures in the flow field through the analysis of velocity field [4, 7, 8, 36]. The data obtained from HWA have been used to explain the phenomena observed by flow visualization in those studies, which have been mentioned above. One of such studies is done by Coelho and Hunt [36], who focused on the dynamic of nearfield of strong jets in crossflow and shows that turbulent entrainment and the transport of the transverse component of vorticity largely control the dynamics of the jet and its boundary shear layer in the near field of jets in crossflows. In this study, velocity data of HWA shows that the diffusion of vorticity into the wake is weak and therefore the

jet does not act on the external flow like a solid bluff body, which is similar to what Fric found [7].

Recent research use HWA to investigate the instability inside the flow field [7, 43, 44], particularly the instability in the shear layer vortices, which have been observed by flow visualization and are generally thought to result from a Kelvin-Helmholtz instability near the jet exit [7, 8], although Balnchard et al [48] argue that the near-field instabilities for the jet in crossflow are not of the Kelven-Helmholtz type, owing to the shear between the jet and cross-stream, but rather are of an elliptical nature, strongly influenced by the near-field formation and longitudinal evolution of the CVP and its effect on transverse eddy structures. Despite this argument, it's generally agreed that the evolution of these shear layer vortices has a strong relation on the formation of CVP, as mentioned before. In addition, an understanding of transverse jet shear-layer instabilities can have a profound impact on jet control. The control of jet will be introduced in Section 2. 4.

A detail study on jet shear layer instability by HWA in wind tunnel is done by Megerian, Davitian, et al [44]. First of all, the experiments suggest that even at relatively large values of R, the transverse-jet shear-layers instabilities may be remarkably different from those associated with the free jet. Then difference in character of shear-layer instabilities between flush- and elevated-injection conditions in the range of R (1.25~3.25) are found. At this range of R, the elevated jet's shear-layer instabilities were dramatically weakened in comparison to those for the flush jet. All of these differences in the transverse-jet shear-layer response for different jet and crossflow conditions suggest that a variety of different jet forcing strategies could be applied for the control of such jets in practical systems, depending on the specific jet and crossflow conditions and specific flow regime.

Getsinger and Hendrickson investigated shear layer instabilities in low-density transverse jets with HWA recently [43]. In their study, spectral measurements corresponding to fluctuations in vertical velocity were obtained using a hot wire, along the jet shear layer, revealing the dependence of the shear layer stability on independent manipulation of jet-to-crossflow density ratio as well as jet-to-crossflow momentum flux ratio. The results show a process of energy transfer from the fundamental mode to its sub harmonic, appeared to be enhanced at lower density ratios, as well as an apparent lack of Strouhal number scaling of the global mode as the jet density was lowered. All of them indicate a different type of global mode occurring in low density transverse jets than in

higher-density ones, similar to the mode competition between shear layer- and 'jets column' –type modes in variable density axisymmetric jets under external flow [49]

Moreover, Bayraktar S. & Yilmas T. proposed various methods to process the velocity measurements data obtained by HWA experiment, such as Fourier, wavelet and proper orthogonal decomposition (POD) techniques [38]. While Fourier transform is widely used in the signal processing field and provides time-independent averaged spectral coefficient, wavelet transform could produce a potentially more revealing picture of the time-frequency localization of signals and contains more information on time and frequency, so can be treated as mathematical microscopy [50]. Thus it is suitable for studying unsteady turbulent flows with complex flow characteristics. Proper orthogonal decomposition (POD) is another advanced signal processing technique, which organizes data into orthogonal modes whose reduction depends on their contribution to the energy of the flow. Power spectrum obtained by Fourier analysis shows that flow at the center of nozzle has better laminar property than in subsequent stations. In addition, the energy of the flow decreases when jet exit velocity increases. Wavelet analysis reveals the dominant frequencies of the flow to be 45 Hz for R =0.5 and 85-105 Hz for R=1.0. POD gives the results of energy distribution of the flow, showing that while R increases energy of the flow, it becomes distributed into more modes, indicating the turbulence becomes more dominant in the flow.

2.2.3 Laser Optical Diagnostics

Until recently, with the development of advanced laser optical diagnostics techniques, such as laser Doppler anemometry (LDA) [20, 32, and 39], particle image velocimetry (PIV) [14, 16, 17, 18, 20, 37, 40, 42, and 45], planer laser induced fluorescence (PLIF) [12, 14, 17, 19, and 20], these techniques have been used in the investigations of jet in crossflow as well. Both LDV and PIV could provide the information of velocity field, while PLIF could show the concentration field.

One of the earliest LDA study on jet into crossflow was done by Ozcan and Larsen in a low speed wind tunnel [39]. Mean velocity vector map and sectional streamlines in the center plane and various sections are presented in this study, which also reveal the critical points defining the CVP and the horsehoe vortex in a jet in crossflow. Based on the velocity map, the authors speculate that the crossflow fluid enters into the plane of

symmetry at a singular point, which is around 2 jet diameters downstream of jet axis, and then it is dispersed in all directions. This hypothesis is supported by flow-visualization studies [13]. Topologies in the center plane and cross sections (normal to the crossflow) are similar for low and high velocity ratios. However, topologies of sectional streamlines near the jet exit (plane normal to jet axis) are dissimilar for two velocity ratios studied, indicating different strengths and stages of CVP formation.

PIV is another powerful technique to obtain the velocity field of jet into crossflow. An example of application of PIV on the study of jet into crossflow is Perterson and Plesniak's work [37], which focus on the evolution of a short injection-hole jet issuing into a crossflow at low velocity ratios. PIV is used there to determine structural features of the jet/crossflow interaction throughout its development from within the jet supply channel (which feeds the holes), through the injection hole, and into the crossflow. The effect of supply channel feed orientations, i.e. counter to, or in the same direction as the crossflow is emphasized in their study, which are found to affect profoundly such jet characteristics as trajectory and lateral spreading. The results show that fluid within the high speed supply channel exhibits swirling motions similar to the flow induced by a CVP, the sense of which depends upon the orientation of the supply channel flow with respect to the crossflow, and in turn impacts the in-hole velocity fields. In the co-flow supply channel geometry (channel flow is in the same direction as the free stream), a CVP exists with the hole with the same sense of rotation as the primary configuration of CVP in the main stream, which could enhance the development of CVP and thus increase the trajectory and decrease the spanwise spreading. The counter flow supply channel configuration shows opposite results.

Meyer and Ozcan used both LDA and PIV to study the flow field in a water channel [20]. They found that LDA and PIV in general give results in good agreement. However, in a region with intense mixing just downstream of the jet trajectory some deviations are found. They explained that these deviations are mainly caused by the measuring volume of PIV being too large to capture smaller scales in regions of high turbulence and mixing. PLIF and LIF have been also conducted, thus velocity and concentration could be simultaneous measured to provide Reynolds fluxes, which is important for the understanding of mixing processes. Comparison of the results from same jet injected into two crossflows with different Reynolds number shows that penetration of the jet into the duct is much higher for the laminar case than the turbulent one, which is due to the higher

diffusion of the jet momentum and larger kinetic energy of the incoming flow for the turbulent case.

As the study above, PIV and PLIF are usually implemented together in the study of jet into cross flow, in order to obtain both velocity and concentration information from the flow field, which could be illuminated by the same laser sheet. Another example of such study is presented by Su and Mungal [17]. This work focuses on the developing region of flow as well. The flow trajectory, which has been mentioned in Section 2.1, has been quantified based on both scalar concentration field and velocity field. Both of them demonstrate that the flow penetrates further into the crossflow with the nozzle exit placed flush with the facility wall, than that with the nozzle protruding into the crossflow. This tendency can be intuitively explained by noting that in the case of flush nozzle, the jet initially flows through low-momentum fluid in the crossflow boundary layer. In addition, analysis of turbulence quantities in the scalar and velocity fields is permitted by the high resolution of the measurements. The results show that the intensity of the mixing, as quantified by the scalar variance and the magnitude of the turbulent scalar fluxes, is initially higher on the jet windward side, but eventually becomes higher on the wake side. Another conclusion from the comparisons between their work and another work done by Smith and Mungal [12] is that the jet exit velocity profile is more significant in defining the evolution of the crossflow-jet mixing field than the jet nozzle position or the velocity ratio.

The work done by Smith and Mungal presents results from extensive imaging of the planar concentration field of the jet in crossflow [12]. They use three length scalings, D, RD, and R^2D to interpret these results. In the end, they conclude that it should be noted that the near field is the region of CVP development, and the far field is the region where the CVP is fully developed. Thus the CVP itself does not enhance mixing compared to the free jet, as the CVP is in the far-field region. Instead it is the structural formation of the CVP that corresponds to the enhanced mixing region, the near field.

Another combined application of LIF and PIV on the study of jet into crossflow is accomplished by Haven and Kurosaka [14], which concerns the effect of different hole shapes on the evolution of jet into crossflow with relative low jet-to-crossflow velocity/momentum flux ratios, for the application of film cooling, where the attachment of the jet to the wall is crucial. The LIF images at different cross-sections reveal that for

each jet configuration the stream wise vortices consist of more than a single counter-rotating pair. They appear to be stacked on top of one another as double-deck structures and are labeled as ‘lower’ and ‘upper’ vortices, as shown in Fig. 2.2-3. The different sense of rotation of upper-deck vortices, caused by different shape of holes, either cancel or reinforce the effect of the lower kidney vortices, thus influence both the jet penetration and lateral movement. In addition, flow visualization and PIV reveal distinct contributions to the kidney vortices from the leading and trailing edge boundary layers. In fact, all vorticity around the circumference of the jet influences, in one way or another, the downstream kidney-vortex structures. They conclude that the flow field at a point is inseparably dependent on that at the other points.

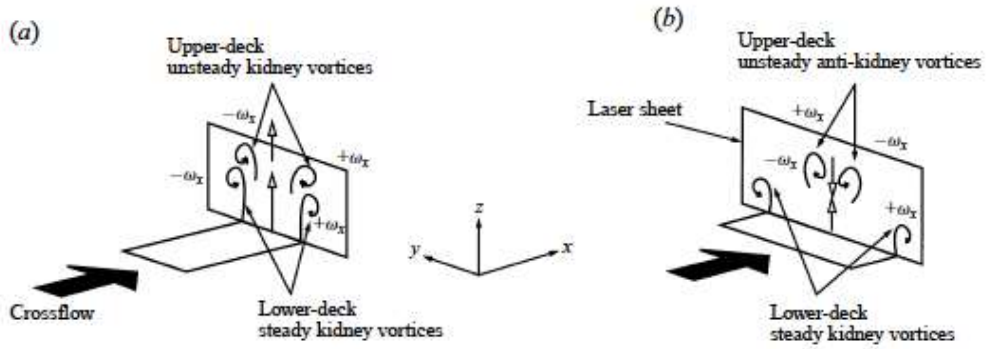

Figure 2.2-3 Double-decked structure showing (a) unsteady kidney pair in the upper deck for low-aspect-ratio rectangle and (b) unsteady ‘anti-kidney’ pair for high-aspect-ratio rectangle (adapted from [14])

2.3 Numerical Study

Numerical simulations can provide a useful source of new data for turbulent flows, as simulations allow examination of quantities, which are difficult to measure accurately in experiments. Firstly, the only feasible means of numerically simulating this flow has been through solving the Reynolds-averaged Navier-Stokes equations. Sykes et al. solved them using a version of the Mellor Yamada 2.5 turbulence model [51]. They used a very limited number of points and did not resolve the flow near the bottom wall, which limits the value of their results. Claus and Vanka [52] used a simple k-ε turbulence model with many more points and still had trouble reproducing mean experimental results. They concluded from their study that Reynolds-averaged Navier-Stokes models developed for use with simple boundary layer flows were not accurate enough for the complexities of

the jet in crossflow. Kim and Benson [53] attempted to improve on the turbulence model by introducing turbulent time scales which vary in the flow. They also employed a numerical method which allowed them to simulate the flow beneath the flat plate, greatly improving the inflow boundary condition for the jet. Their results reproduced mean flow statistics reasonably well, but severely underpredicted turbulent kinetic energy. Demuren [54] modeled the full Reynolds stress transport equations in his simulations, but still failed to accurately reproduce mean velocities and overpredicted turbulent kinetic energy.

Until recently, the tremendous development of computer technology, regarding both hardware and algorithm, has allowed researchers to contemplate space-time accurate simulations of the flow. Yuan and Street [55] reported on large-eddy simulations that they have performed of the jet into crossflow, in which they have achieved quantitative agreement with experimental measurements. The main focus of their study is to examine the development of large-scale features in the flow and to understand how these features affect turbulent statistics. Several new structures in the near field of the jet have been identified by this study. First of all, the spanwise rollers on the upstream (shear layer vortex) and downstream edges of the jet are created by a Kelvin-Helmholtz instability, and these rollers carry intense velocity fluctuations and account for most of the turbulence kinetic energy (TKE) production in the near field. The CVP has been found to form by those quasi-stable hanging vortices, originated from skewed mixing layers between jet edges and crossflow, encountering a strong compressive stress from crossflow. This has been proved by the experiment study of [13]. Evidence of wake vortices has been also found in this study.

Inclined injection of a jet into crossflow with velocity ratio 0.5 has been simulated by Wegner and Huai [56], using LES as well. The ability of LES to precisely capture the flow and mixing features in jets in cross-flows has been demonstrated when compared to experimental data of Andreopoulos [57] and Andreopoulos and Rodi [58]. Mixing processes taking place while jet has been injected into crossflow with different angles (90, ±30) have been discussed. Jet injected towards the crossflow has been proved to be most favorable for mixing between jet and crossflow, which could be related with the increased amount of unsteadiness caused by this reverse injection.

While LES could capture most of the flow features, direct numerical simulation (DNS) provides a full numerical solution of the Navier-Stokes equation without any turbulence

model, which means that the whole range of special and temporal scales of the turbulence have been resolved, despite its super high computational cost, even at low Reynolds numbers. Munppidi and Mahesh [59] have implemented this technique to study the trajectories of jets in crossflow, which are scaled by *RD*. The results show the dependence of jet trajectory on both of crossflow boundary layer thickness and the jet velocity profile. In addition, a length scale h is proposed in this study that parameterizes the relative inertia of the jet and the crossflow, which take into account both the jet velocity profile and the crossflow boundary layer thickness. Including this h into the trajectory scaling yields:

$$z/RD = A'(x/RD)^B(h/RD)^C \qquad \text{(Eq. 2-6)}$$

Where A', B and C are constants. They stated that this scaled trajectories show a significantly better collapse with simulation data.

More recently, the same group has conducted another DNS study on jet in crossflow, which is more focused on velocity and turbulent intensity distribution in the flow field [60]. Same experimental conditions in the study of Su and Mungal [17] have been chosen, and the results show good agreement with each other. Despite the confirmation of those macro features of jet in crossflow, such as CVP, trajectory, an examination of turbulent kinetic energy budget for this flow has been reported as well, showing that the flow is not in turbulent equilibrium. Jet and crossflow fluid interaction in the near field causes peak production of turbulent kinetic energy on the leading edge of the jet. While in the far field, entrainment of crossflow fluid and the CVP cause peak production below the center streamline. Thus it turns out that the turbulence kinetic energy produced at the jet edges is transported toward the center of the jet.

Since vortex methods are particularly useful in simulating unbounded, incompressible, unsteady flows, where the fluid containing vorticity occupies only a small fraction of the total fluid volume [61], these methods have been used to simulate some aspects of the evolution of jets in crossflow. For example, Cortelezzi and Karagozian have used vortex methods to simulate and analyze the generation and evolution of the vorticity field [9]. Their results of evolution of transverse jets in nearfield vortex filament simulations confirm the mechanism proposed by Kelso et al., [8] and others describing the formation of the CVP, which has been mentioned in the discussion of experiment study on jets in crossflow. In addition, the effect of boundary layer thickness on global trajectory has

been found here as well as the study of Munppidi and Mahesh [59], which indicates the jet penetrates further into the crossflow with increasing boundary layer thickness. A visualization of a bundle of the deflected upstream boundary layer flow about the jet and upward into the lee side of the jet could be derived from the ensemble-average velocity field, suggesting origins of the experimentally observed wake vortices within the boundary layer, again consistent with experiments [7, 12]. Finally, the results show that the entrainment of crossflow is clearly enhanced as the jet is deformed and as vortex rollup results in the formation of the CVP.

Marzouk and Ghoniem [62] also developed a three-dimensional vortex element method to simulate the flow field of an incompressible transverse jet at high Reynolds number, providing a clear description of the formation of large-scale vertical structures relevant to mixing.

2.4 Jet Control and its Application in Internal Combustion Engine

Different strategies should be considered for each different application of jet into crossflow, due to its wide range of conditions. For instance, while it is applied as film cooling in gas turbines, the attachment of the jet to the wall is crucial, thus the lift caused by the CVP should be compressed. Haven and Kurosaka [14] have studied the effect of hole-shapes on the jet penetration, and they found that the hole geometry has a powerful influence on the very near field character. The proximity of these counter-rotating vortices relative to one another affects both the lift-off of the jet as well as the entrainment of crossflow fluid toward the plate surface. The results for six basic hole-geometries show that the jet from the high-aspect-ratio holes, with increased separation distance between the sidewall vortices, stay attached the surface even for higher blowing ratios. Thus they conclude that by manipulating the hole-geometry alone, without increasing the hole cross-sectional area, one can reduce jet lift-off.

Jet injection angle should be another important concern, although this has received considerably less attention and only few studies have been performed. Wegner and Huai [56] used numerical method to study influence angle on turbulent mixing. Their results show that injection normal to or counter with flow has almost same growth rate (the slope

of the mixedness parameter curve) of mixedness, while streamwise injection shows a significantly smaller rate of mixing than the two other cases. They pointed out that it seems favorable to inject the jet at an angle inclined against the oncoming main flow, from an engineering point of view, which could help build shorter, lighter and cheaper devices.

One significant interest of both researchers and engineers is the active control of vorticity generation and hence jet penetration and mixing processes, through temporal excitation of the transverse jet fluid. Such excitation has been of significant interest for well over a decade. Experiments on pulsed or acoustically excited transverse jets [8, 11, 31, 35, 63-66], suggest that for certain excitation conditions, increased jet penetration into the crossflow and/or increased mixing maybe achieved. Yet specific conditions yielding increased penetration vary rather widely among the different sets of experiments that have been conducted in both liquids [11, 65] and gases [31, 35, 63, 64, 66].

Some of these recent studies have focused on sinusoidal excitation [8, 31, 63] and find improvement in transverse jet mixing when forcing at specific values of the Strouhal number (based on mean jet velocity and jet orifice diameter, $St_f = f_f D/U_j$). For example, in the gas-phase experiments in [31], the forcing frequency f_f for maximized jet spread and mixing is equal to or greater than that associated with the unforced transverse jet's shear-layer instability, when the mean jet-to-crossflow velocity ratio R is equal to 6. For these studies, significant jet response is achieved when sinusoidal jet forcing with a peak-to-peak velocity excitation amplitude of about 30% of the mean jet exit velocity is employed.

However, in other cases, e.g., in the gas-phase experiments by M'Closkey et al. [35], there is little response of the jet to sinusoidal forcing, even to very high amplitude excitation with the peak-to-peak amplitude exceeding about 75% of the mean jet velocity, irrespective of the applied frequency. These experiments are conducted at a lower value of R, 2.58, which suggest a globally unstable jet shear layer. This and other studies [64, 65, 11] utilize square-wave excitation for the transverse jet, with the ability to modify both excitation frequency f_f and the duty cycle α of the wave form, the latter of which is defined as the ratio of the temporal pulse width τ to the period T of square-wave forcing, where $T=1/f_f$. Studies of fully modulated transverse jets by Johari et al. [65], for example,

suggest that optimal jet penetration and spread may occur for specific values of the Strouhal number and relatively low values of duty cycle, on the order of α=20%.

Recently, jet into crossflow is applied in automotive industry as well, such as port fuel injection (PFI) for internal combustion engines fueled with non-conventional gaseous fuels, such as methane, hydrogen, CH_4/H_2 mixtures or synthetic fuels, all of which offers considerable potential as an alternative fuel to fossil fuels, as mentioned at the beginning of this thesis [67]. Hydrogen is a potential alternative to gasoline in the future, which is considered a near perfect energy storage medium, as it can be created from either fossil or non-fossil sources. However, hydrogen is currently a rare commodity compared to hydrocarbon fuels partly due to a lack of the distribution infrastructure. Current use of hydrogen is probably limited to the role of a fuel additive [68]. Natural gas vehicles are a potential alternative to gasoline vehicles in short term, because of the widely available fuel and less pollution. In order to further reduce their pollutants, hydrogen enriched natural gas has been burned in gas vehicles, which combines the advantages of both hydrogen and methane. [69]

No matter which gaseous fuel is implemented on internal combustion engines, fuel-air mixing should be carefully concerned, and direct injection has long been viewed as one of the most attractive advanced options, which is based on the high volumetric efficiency and the potential to avoid pre-ignition [70]. The challenge with direct injection operation is that in-cylinder injection requires fuel-air mixing in a very short time. For early injection (i.e., coincident with intake valve close) maximum available mixing times range from approximately 20-4 ms across the speed range 1000-5000 rpm, respectively, while Homan's study [71] demonstrates that complete mixing of hydrogen and air in an engine takes approximately 10 ms. Particularly, homogeneously charged compression-ignition (HCCI) type engines have been the subject of much research recently, which are capable of providing at high load more efficient and increase power output than conventional diesel engines while reducing exhaust emissions [72]. This concept acquires more on fuel-air mixing, where port injection could still bring benefits. In fact, in most applications to date natural gas is injected in the intake manifold [3].

To summarize, despite the large amounts of work that have been done on the study of jet into crossflow, further studies on transverse jets are needed because of the complexity of the phenomenon, and the wide range of conditions found in practical applications. For

instance, most of the reported experiments have been performed in large wind tunnels, when the effect of wall confinement on the jet's trajectory is insignificant and only the boundary layer on the wall from which the jet issues affects the vertical structures in the wake of the jet. Jets in confined turbulent crossflow have received considerably less attention. Moreover, most investigations considered jets and crossflows having low turbulence and thin boundary layers, while most practical applications deal with turbulent inlet conditions with thick boundary layers

In addition, data resulted from injection of gaseous fuel into intake port or manifold for a port fuel injection (PFI) internal combustion engines and the air-fuel mixing process is quite limited, which is a typical flowfield caused by jet into confined crossflow. Thus this study is proposed in order to understand gas injection into a steady crossflow confined into a transparent duct which provides the possibility for the various experimental measurements. Detail of the experimental set up will be followed in next chapter.

CHAPTER 3

EXPERIMENTAL TECHNIQUES AND METHODOLOGY

As stated before, the experimental activities are conducted with one transparent duct, aiming to simulate the intake port of internal combustion engine. This duct and the flow rig, together with all experimental techniques, are described in the following.

3.1 Transparent Duct and Flow Rig Description

The transparent straight duct used in this study is made by Poly (methyl methacrylate), with a square cross-section 40 mm × 40 mm and 500 mm in length, aimed at simulating the intake port of a normal naturally aspirated light duty natural gas engine, while allowing full optical access (Fig. 3.1-1, Fig. 3.1-2). The air stream, supplied by the laboratory's compressed air line, was introduced from one side of the duct through a cylindrical pipe (inner diameter = 19 mm) and exhausted from the open opposite side. A perforated grid with void ratio (area of the holes to the total area) equal to 60.5% was inserted at the entrance of the duct, well upstream the jet injection cross-section to keep the turbulence of crossflow approximately homogeneous and isotropic. The volume flow rate of inlet air in the duct was regulated and monitored with a rotameter, under controlled temperature and pressure.

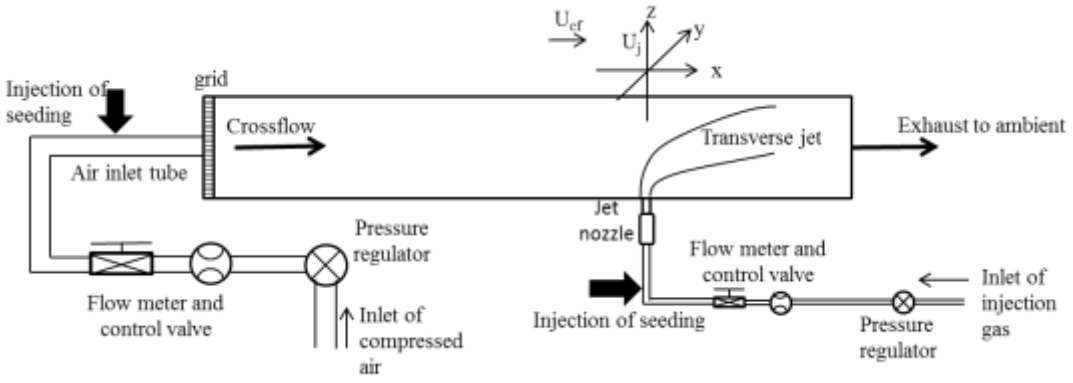

Figure 3.1-1Schematic diagram of the duct with transverse gas injection, and the coordinate system

(a) 3D model of test bench for jet into crossflow: jet injected into crossflow confined in a transparent square duct from a nozzle on the side of a transparent duct

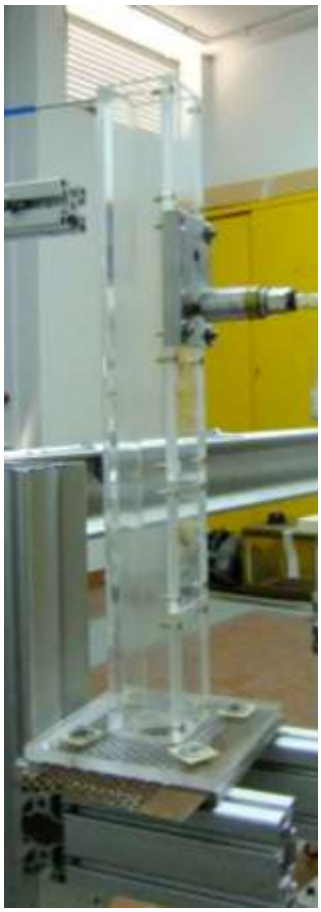

(b) Photo of transparent duct with injection nozzle on the side

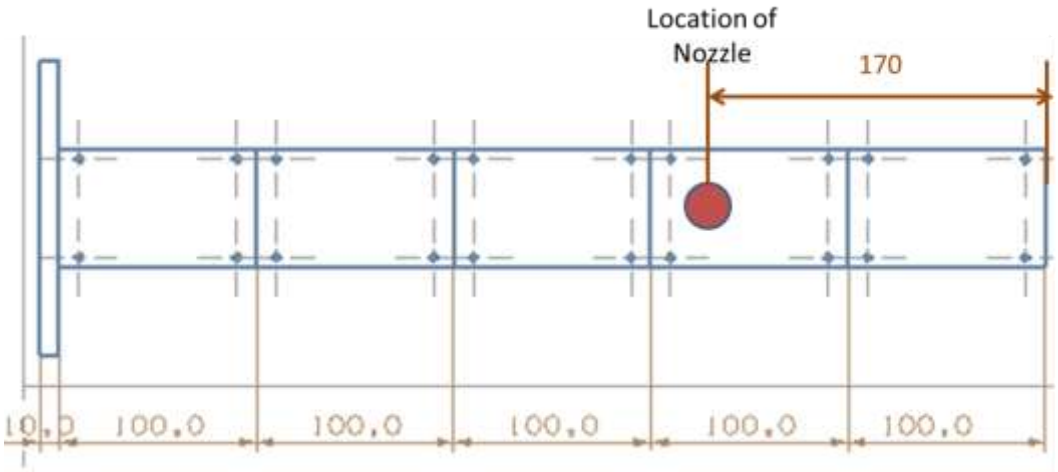

(c) Dimension of transparent duct (unit: mm)

Figure 3.1-2 Transparent duct

As indicated in Fig. 3.1-1, the incompressible gas jet entered the crossflow through a round nozzle, whose outlet was mounted flush with one of the duct wall (called injection wall, hereafter). When the jet is normally injected with respect to crossflow, the jet pipe

axis resulted parallel to the Z direction of the coordinate system shown in Fig. 3.1-1 as well, which will be used throughout this paper, with the origin located at the center of the jet exit, and X axis being the direction of the crossflow. The jet axis was located 330 mm downstream of the inlet section and 170 mm upstream of the exit. For all the experiments, the temperatures of both the jet and crossflow were kept equal as ambient temperatures.

Two nozzles with different size have been implemented in this study, which is shown in Fig. 3.1-3. The smaller one has an inner diameter of 3.2 mm, while the larger one has an inner diameter of 6.4 mm. The lengths of both nozzles are around 24 mm. During experiment, these two nozzles are set onto the duct through a plate adapter. The inner geometry of these two nozzles is shown in Fig. 3.1.3 (b), where a small contraction region could be seen near the middle of these nozzles.

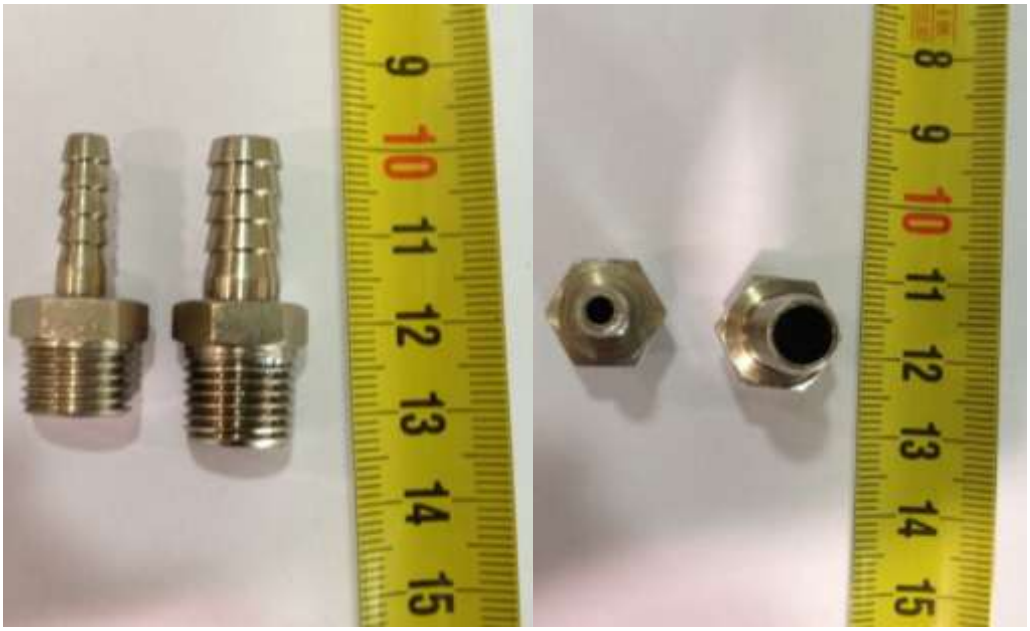

(a) Photo of Injection nozzle

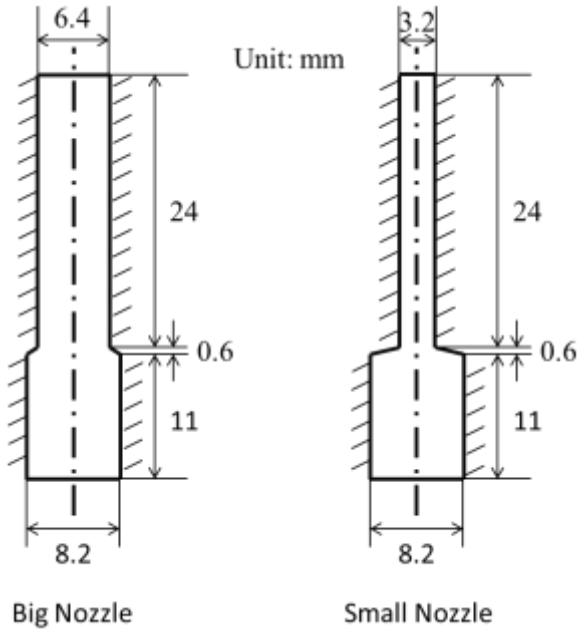

(b) Inner geometry of injection nozzle

Figure 3.1-3 Injection nozzle

Different injection orientations have been concerned in this study. The detail of different injection orientation and its effect on the flow field will be given in chapter 4.

3.2 Schlieren Imaging

The present investigation combines flow visualization with quantitative velocity measurements. Schlieren imaging were conducted firstly to study the topology of the jet, to acquire important insight into the flow field and to select the experimental conditions for subsequent measurements.

3.2.1 Principle of Schlieren Imaging

The term schlieren, which originates from German, means optical inhomogeneities in transparent material not visible to human eye [73]. They are relatively small refractive differences within the overall background [74, 75] and by definition they bend light in any direction other than the ‘normal’ direction (which light is supposed to transmit). Schlieren occur in solids, liquids, and gases. They may result from temperature changes, high-speed flows, or the mixing of dissimilar materials. In glass and plastic, they may be

due to inclusions of variable density or to thickness differences in otherwise-homogeneous material. Some schlieren are of complicated structure, others are simple. Some reflect light very strongly, others barely at all.

Schlieren flow visualization, or so called schlieren imaging, for brief, is based on the deflection of light by a refractive index gradient, which is directly related to flow density gradient. Consider a light is transmitted in z direction, it can be demonstrated that optical inhomogeneities refract or bend light rays in proportion to their gradients of refractive index in an x,y-plane. The resulting ray curvature is given by:

$$\frac{\partial^2 x}{\partial z^2} = \frac{1}{n}\frac{\partial n}{\partial x},\ \frac{\partial^2 y}{\partial z^2} = \frac{1}{n}\frac{\partial n}{\partial y} \qquad \text{(Eq. 3-1)}$$

Where n is the refraction index of the corresponding material. Integrating once, the components of the angular ray deflection in the x- (ε_x) and y- (ε_y) directions are:

$$\mathcal{E}_x = \frac{1}{n}\int \frac{\partial n}{\partial x}\partial z,\ \mathcal{E}_y = \frac{1}{n}\int \frac{\partial n}{\partial y}\partial z \qquad \text{(Eq. 3-2)}$$

To understand the basics of schlieren imaging, it helps to begin as simply as possible with two lenses, geometric optics and a point light source, which is shown in Fig. 3.2-1.

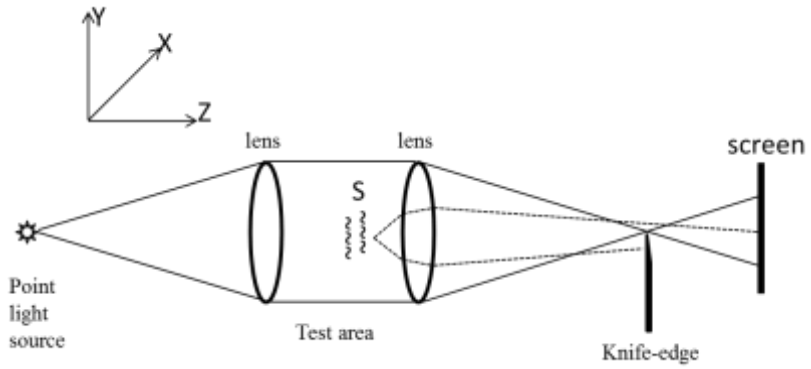

Figure 3.2-1 Diagram of a simple schlieren system with a point light source

As show in Fig. 3.2-1, if a schlieren object S is added to the test area, it bends light rays away from their original paths. Despite this, however, the second lens focuses the ray from each point in S to a corresponding point in the screen image. Two such rays are shown in this figure: one bent upward, the other downward. Both refracted rays miss the focus of the optical system. The upward-deflected ray brightens a point on the screen, but the downward-deflected ray hits the knife edge. Its corresponding image point is dark

against a bright background. For this particular point of the schlieren object, the phase difference causing a vertical gradient $\partial n/\partial y$ in the test area is converted to an amplitude difference, and thus the invisible phase difference is made visible.

This point-source schlieren system is good for illustration, but not very practical, since its operation is "on-or-off," with infinite sensitivity over zero measuring range. In order to take real schlieren pictures, an extended light source is generally required, which is shown in Fig. 3.2-2.

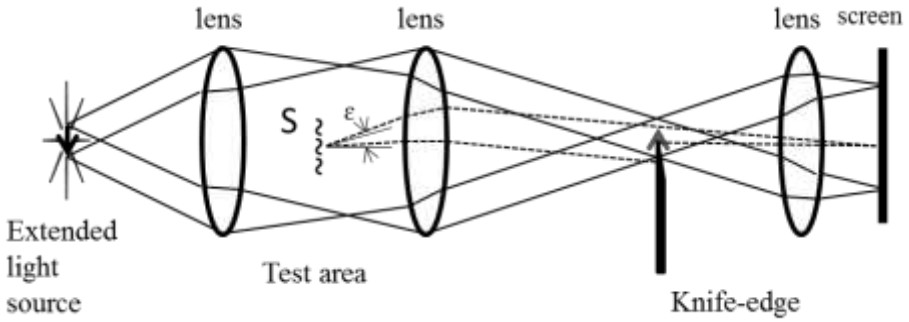

Figure 3.2-2 Diagram of a simple schlieren system with an extended light source

As diagrammed in Fig. 3.2-2, an additional focusing lens is added after the knife edge. An incoherent beam of white light originates from the extended source, here shown as a downward-pointing arrow. Collimated by the first lens, the light beam traverses the test area and is refocused by the second lens to form an inverted image of the source at the knife-edge. Now a ray bundle from all light-source points suffers the refraction angle ε. This bundle-shown as dashed lines, originally proceeded to form an elemental source image in the knife-edge plane in the absence of refraction, now displaces from the undisturbed composite source image by virtue of its refraction. This concept is illustrated in Fig. 3.2-3[76].

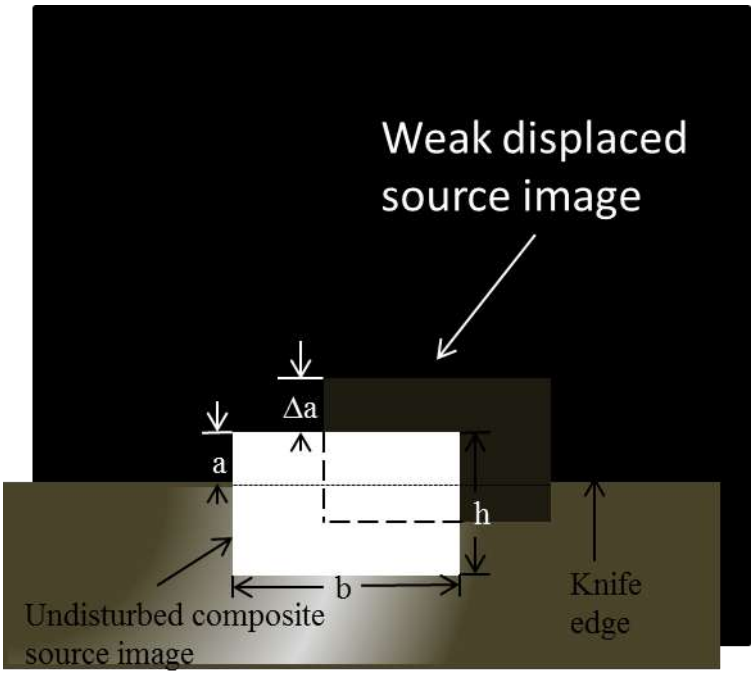

Figure 3.2-3 Diagram of the knife-edge plane.

As indicated in Fig. 3.2-3, a rectangular composite source image is shown about half cut-off, with a remaining unobscured height, a, by the knife-edge. Due to refraction at a point in the test area, a weak elemental source image is shifted to the upper right. Its unobscured height, a+Δa, passes extra light to a corresponding point in the schlieren image

Despite this displacement in the knife-edge plane, the ray bundle originating at a test-area point is returned by the second and third lens to the same relative position in the conjugate image plane on the screen, which happens, according to the properties of lens, regardless of the angle ε at which the rays left the test plane. Thus it is possible to separate the extraordinary light rays-refracted by schlieren in the test area-from the ordinary rays that provide the general background luminance. Once separated, the refracted light is marked by a different amount of cutoff at the knife-edge, and then recombined in the schlieren image to yield illuminance variations with respect to the background [77]. The schlieren image is built up of many such points of varying illuminance, corresponding to the shape and strength of the refractive schlieren object.

In Fig. 3.2-3, the amount of knife-edge cutoff of the undisturbed composite source image sets the background level of illuminance in the image on the viewing screen. As a

consequence, within the measuring range of the instrument, the image illuminance I is, by geometric optics, linearly proportional to the amount of knife-edge cutoff.

Shadowgraph are close related with schlieren image, which is also to visualize the flow based on the variation of refractive index through the light path. But there are several distinctions [78]. Frist, the shadowgraph is not a focused optical image; it is a mere shadow. The schlieren image, however, is what it purports to be: an optical image formed by a lens, and thus bearing a conjugate optical relationship to the schlieren object. Second, schlieren methods require a knife-edge or some other cutoff of the refractive light, where no such cutoff is needed or allowed in shadowgraph. Finally, the illuminance in a schlieren image responds to the first spatial derivative of the refractive index in the schlieren, e.g. $\partial n/\partial x$. The shadowgraph, however, responds to the second spatial derivative or Laplacian, e.g. $\partial^2 n/\partial x^2$. Equivalently, the schlieren image displays the deflection angle ε while shadowgraph displays the ray displacement resulting from the deflection.

By far the most popular arrangement is the Z-type Herschlian system using two oppositely-tilted, on-axis telescopic parabolas (see Fig. 3.2-4). The combination of a diverging illuminator beam, an opposite converging analyzer beam, and a parallel beam between the two mirrors suggests the letter Z, whence the name. The arrangement could reduce the dimension of setup.

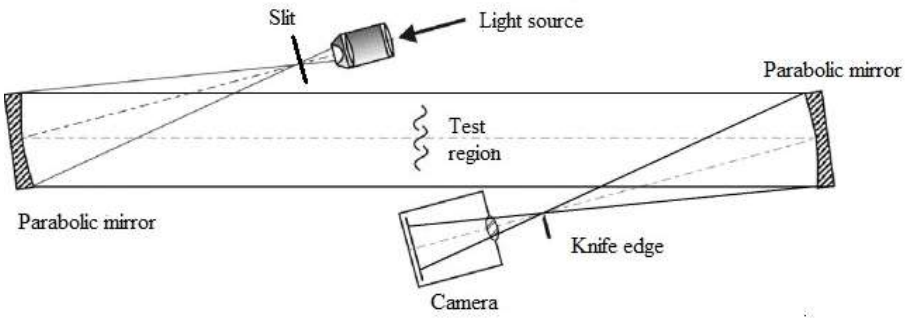

Figure 3.2-4 Z-type schlieren arrangement

The advantage of mirrors in place of lenses is primarily found in a larger field-of-view for a given cost. Nonetheless, there are still problems arising from the use of a system of mirrors are due to optical aberrations, which are known as coma and astigmatism: [77, 79, 80]

Coma: by definition, coma occurs when the direction of light reflected from a mirror depends on the position of the point of reflection. This is a consequence of tilting the schlieren field mirrors off their optical axes. In result, beginning with a point light source, a comatic optical system spreads the point focus into a line. Different annular zones of the mirror-face focus at different points along this line with different spot sizes. The point focus becomes smeared into a region of flare with a bright core at one end: a 'comet', whence the name.

This aberration grows in proportion to the offset angle, and to the inverse square of the mirror *f*/numbers. It could be thus minimized by keeping offset angle small and using long-focal-length mirrors. There are other reasons to do this as well, but fortunately, since coma is generated at both schlieren field mirror, it is possible to cancel its overall effect by tilting the mirrors at equal angles and in opposite directions from the central optical axis, forming a 'Z'. One must use identical mirrors, of course, and all optical elements must be centered in a common plane.

Astigmatism: unlike coma, astigmatism cannot be eliminated from the z-type schlieren or any off-axis mirror system. The word literally means non-point-like, or failure to focus a point to a point. It arises from differences in path length along the optical centerline and the mirror periphery.

To avoid those aberrations as much as possible, recommended practice is to minimize both astigmatism and coma by restricting the offset angles to their minimum practical values. Further, mirrors with *f*/numbers of 6 or greater are strongly recommended.

The main advantages of the schlieren techniques are their sensitivity and their simplicity [81]. It is convenient to use the Z-type mirror system here, to illustrate the geometrical optics of schlieren sensitivity, and consider that the output is a 2-D image in x and y. A horizontal source slit orientation and a horizontal knife edge are assumed for convenience. Beginning with the luminance B emitted by the light source, one can easily find the illuminance I_0 incident upon the first mirror by way of the inverse square law:

$$I_0 = \frac{B \cdot b \cdot h}{F_1^2} \qquad \text{(Eq. 3-3)}$$

where b and h are the breadth and height of the source slit, respectively and F_1 is the focal length of the first mirror. Neglecting any losses, this illuminance level also falls on the test area and the second mirror in parallel light. The schlieren image illuminance is the same as well, in the absence of any knife-edge cutoff, but for a magnification factor m that accounts for image size relative to that of the test area,

$$I_0' = \frac{B \cdot b \cdot h}{m^2 F_1^2} \qquad \text{(Eq. 3-4)}$$

Now let the knife-edge block all but a part of the light source image at the second mirror focus, that part having height a. Replacing h in above equation with (F_1/F_2) a to describe the actual unobstructed height of the light source image,

$$I = \frac{B \cdot b \cdot a}{m^2 F_1 F_2} \qquad \text{(Eq. 3-5)}$$

Every schlieren image has such a background illuminance or amplitude level: I, often appearing as a middle-gray shade. The illuminance of a point in the image is judged by comparison of this level: above it, below it, or equal to it.

Now consider the case of a schlieren object in the test area that refracts a certain light ray through angle ε having y-component ε_y. This will cause a weak elemental source image to shift upward in the knife-edge plane by a distance $\Delta a = \varepsilon_y F_2$ (recall Fig. 3.2-3). Then one obtains:

$$\Delta I = \frac{B \cdot b \cdot \varepsilon_y}{m^2 F_1} \qquad \text{(Eq. 3-6)}$$

which describes the incremental gain of illuminance at the corresponding image point due to the refraction ε_y in the test area.

Contrast in the schlieren image refers to the ratio of differential illuminance ΔI at an image point to the general background level I,

$$C \equiv \frac{\Delta I}{I} = \frac{F_2 \varepsilon_y}{a} \qquad \text{(Eq. 3-7)}$$

This image contrast is the output of the schlieren instrument. The input is a pattern of irregular ray deflections ε, resulting from refractive-index gradients in the test area, in an otherwise regular beam. Since the sensitivity of any instrument is basically an

influence coefficient, i.e. d(output)/d(input), we can therefore write the schlieren sensitivity – sometimes called contrast sensitivity – as the rate of change of image contrast with respect to refraction angle:

$$S = \frac{dC}{d\varepsilon} = \frac{F_2}{a} \qquad \text{(Eq. 3-8)}$$

This simple geometric-optic result is accurate and sufficient for most purpose. It provides a measure of schlieren sensitivity independent of any observing or recording means. It also shows that sensitivity is proportional to the focal length of the second parabolic mirror in a Z-type system, another reason for longer rather than shorter focal length. Further, it reveals that the unobstructed height of the source image, a, determines sensitivity, not the overall height h.

3.2.2 Schlieren Imaging Set up

A Z-type Schlieren imaging set-up was used to provide a light beam, normal to both jet and crossflow (Y direction in the coordinate system of Fig. 3.1-1). The schlieren images of the jets were illuminated by a stroboscopic xenon flash lamp and captured by a CCD camera (PCO SensiCam, 1280×1024 pixels) with a lens (Nikon 60mm), using an exposure time of 20 μs, which is supposed to be short enough to capture the instantaneous phenomena of flow field. The resolution of all schlieren images was set to be 10 pixels for 1 mm. The parameters for other components in the schlieren imaging setup are given below:

- Light source: type 850 Bint xenon strobe white light lamp, which is characterized by: flash frequency from 0 to 60 Hz; energy per flash of 325 mJ (Low position), 580 mJ (position middle), 850 mJ (high position); duration of flash 4 to 10 μs (short enough to froze the flow field), delayed of flash 6 to 9 μs (which is negligible in this study); maximum instantaneous power about 120 kW; synchronized with an external TTL signal. Black Screen in steel with slot-sized central 1x6 mm spot exit of the strobe.
- Signal Generator: BNC 505 Pulse generator
- Mirrors: two Edmund spherical mirrors with a diameter of 150 mm, focal length of 1500 mm, schlieren-specific applications.

3.3 Laser Doppler Velocimetry

Laser Doppler velocimetry (LDV) was applied to provide space and time resolved measurements of the two-dimensional velocity field in several cross-wise (Y, Z) as well as stream-wise (X, Z) sections of the duct, by using two configurations of the optical set-up. The principle and detail setup in this study are given below.

3.3.1 Principle of LDV

Generally, LDV uses monochromatic laser light as a light source. The interference of two beams crossing in the measurement volume or the interference of two scattering waves on the detector creates a fringe patter. The velocity information for moving scattering centers is contained in the scattered field due to the Doppler effect [82].

The basic principle of the LDV is illustrated in Fig. 3.3-1. The Doppler effect is invoked twice, once when the incident laser light of the transmitter system, characterized by the wavelength λ_b and frequency f_b (subscript b for beam), impinges on the moving target, and once when light with a frequency f_p is scattered from the moving target particle and received by a stationary detector with the frequency f_r (subscript r for receiver). Then the following relationship could be obtained [83]

$$f_r = f_p \frac{1}{1-\frac{\boldsymbol{e_{pr}}\cdot\boldsymbol{v_p}}{c}} = f_b \frac{1-\frac{\boldsymbol{e_b}\cdot\boldsymbol{v_p}}{c}}{1-\frac{\boldsymbol{e_{pr}}\cdot\boldsymbol{v_p}}{c}} \approx f_b + f_b \frac{\boldsymbol{v_p}\cdot(\boldsymbol{e_{pr}}-\boldsymbol{e_b})}{c} = f_b + \frac{\boldsymbol{v_p}\cdot(\boldsymbol{e_{pr}}-\boldsymbol{e_b})}{\lambda_b}$$

$$(|v_p| \ll c, c = f_b\lambda_b) \quad \text{(Eq. 3-9)}$$

where c is the speed of light in the medium surrounding the particle.

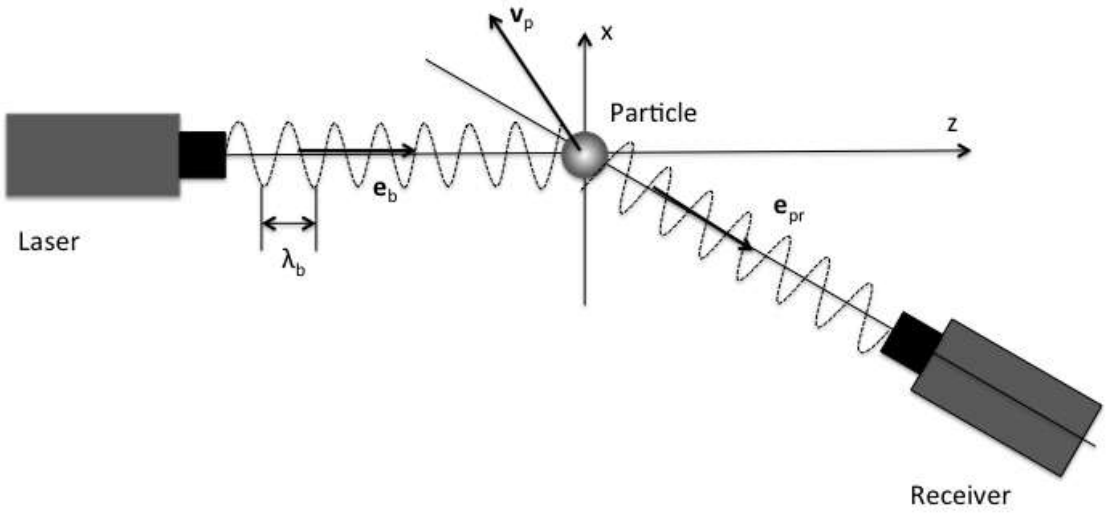

Figure 3.3-1 Defining geometry for applying the Doppler effect in the LDV

The second term after ≈ of Eq. 3-9 contains the Doppler shift of the incident wave frequency. The difference of the normal vectors appears when the direction of propagation of the incident and scattered wave differs. The Doppler shift is directly proportional to this difference and to the velocity of the particle. Conventional optical arrangements work with two scattered waves, each exhibiting a different Doppler shift, since for typical flow systems the Doppler shift is of the order 1~100MHz, which compared to the frequency of laser light of approximately 10^{14} Hz is very small and thus virtually impossible to resolve directly.

Fig. 3.3-2 shows the so-called dual-beam configuration, on which a real measurement volume is formed at the intersection of the two incident waves and the scattered waves are detected with a single detector [84, 85]. In this configuration:

$$f_1 = f_b + \frac{\boldsymbol{v}_p \cdot (\boldsymbol{e}_{pr} - \boldsymbol{e}_1)}{\lambda_b},\ f_2 = f_b + \frac{\boldsymbol{v}_p \cdot (\boldsymbol{e}_{pr} - \boldsymbol{e}_2)}{\lambda_b} \quad \text{(Eq. 3-10)}$$

$$f_D = f_2 - f_1 = \frac{\boldsymbol{v}_p \cdot (\boldsymbol{e}_1 - \boldsymbol{e}_2)}{\lambda_b} \quad \text{(Eq. 3-11)}$$

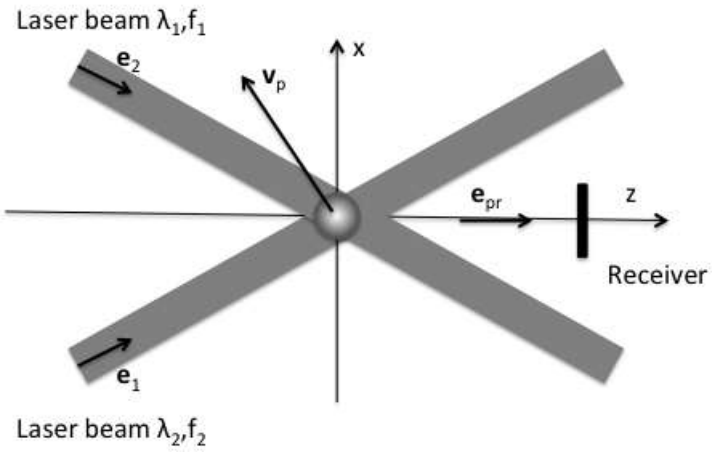

Figure 3.3-2 Optical configuration for dual-incident-beam systems

Noteworthy is the fact that the difference frequency is independent of the receiver position for the dual-beam configurations in Fig. 3.3-2. If the intersection angle of two beams is denoted by Θ, then the difference frequency on the detector is given by

$$f_D = \frac{2sin^{\Theta}/_2}{\lambda_b}\left|\boldsymbol{v}_p\right|cos\alpha = \frac{2sin^{\Theta}/_2}{\lambda_b} v_{p\perp} \quad \text{(Eq. 3-12)}$$

as clarified also in Fig. 3.3-3:

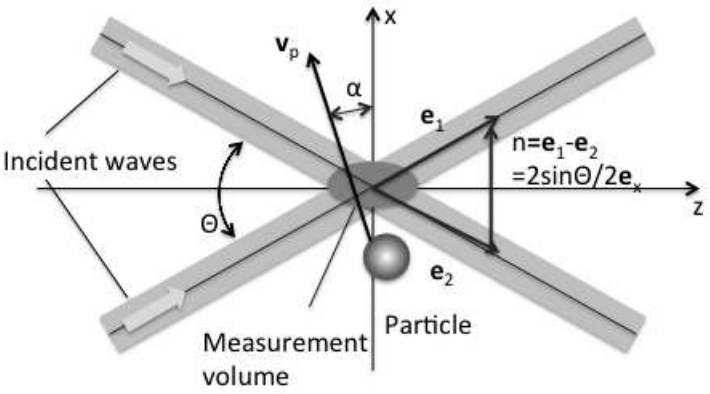

Figure 3.3-3 Vector relations relevant to determining the Doppler frequency

The flow direction α is measured with respect to the perpendicular of the beam bisector. Thus the frequency difference is linearly proportional to the velocity component in the x direction, denoted by $v_{p\perp}$ or v_{px}.

This result could be deduced from the interference theory. The two incident laser beams form an intersection volume, which could be interpreted as an interference field with fringes. The fringes spacing is given by:

$$\Delta x = \frac{\lambda_b}{2sin^{\Theta}/_2} \qquad \text{(Eq. 3-13)}$$

If a small particle $d_p << \Delta x$ passes through the interference pattern, it could effectively sample the local intensity, which is constant over its diameter. A particle of diameter d_p perceives a mean power of from laser, which is product of its center plane area and light intensity, and scatters this power in all space. The scattered wave is modulated in its amplitude and has the carrier frequency. Therefore and electrical signal i(t) is obtained from the photodetector, whose amplitude is modulated with the difference frequency f_D. The frequency f_D is called the Doppler frequency, which is defined as Eq.3-12.

The velocity component perpendicular to interference fringes is then inversely proportional to the period of the fringe crossing T_D:

$$v_{p\perp} = \frac{\Delta x}{T_D} \qquad \text{(Eq. 3-14)}$$

note that this 'interference' or fringe model of the LDV is strictly only valid for very small particles fulfilling the condition $d_p << \lambda_b$, since only then can the amplitude and phase, or the intensity of the field be considered constant over the particle diameter. For particles larger than the wavelength of light this model fails. Both the amplitude and the phase of the incident waves vary across the diameter of the particle. Effectively the particle images certain parts of the incident waves onto the photodetector, thus only certain areas of the particle surface are involved in defining signal properties. Nonetheless, the signal from the detector is still modulated by the Doppler frequency, and Eq. 3-12 remains valid.

The optical arrangement discussed above yields the velocity component normal to the interference fringes; however, its sense is no longer contained in the received signal. Directional information is recovered when incident laser beams of different wavelengths are used. A wavelength shift of one or both of the laser beams can be achieved using acousto-optic modulators, for example Bragg cells [86]. If an acousto-optic modulator is mounted in the path of beam 1, the frequency of the beam can be shifted by an amount f_{sh}, yielding

$$f_1 = f_b + f_{sh} \quad \text{or} \quad f_1 = f_b - f_{sh} \qquad \text{(Eq. 3-15)}$$

Since the frequency f is the derivative of the phase with time

$$f = \frac{1}{2\pi}\frac{d\varphi}{dt} \qquad \text{(Eq. 3-16)}$$

For a stationary wave the frequency shift can be expressed as a linear change of phase with time

$$\varphi_1 = 2\pi f_{sh} t \qquad \text{(Eq. 3-17)}$$

in the fringe model this corresponds to a movement of the fringes in the –x or +x direction with a constant velocity. After the optical mixing of the two scattered waves on the detector surface, the modulation of the configuration in Fig. 3.3-3 becomes

$$f_r = f_{sh} + \frac{\boldsymbol{v_p}\cdot(\boldsymbol{e_1}-\boldsymbol{e_2})}{\lambda_b} = f_{sh} \pm \frac{2sin^{\Theta}/_2}{\lambda_b}\left|\boldsymbol{v_{p\perp}}\right| = f_{sh} \pm f_D \quad \text{(Eq. 3-18)}$$

The signal frequency exhibits an offset equal to the shift frequency. A stationary particle will result in a signal with a modulation of f_{sh}. A particle moving with the fringes yields a lower frequency and movement against the fringes, a higher frequency.

A conventional LDV optical arrangement is summarized in Fig. 3.3-4. The laser beam is split into two beams of equal intensity and polarization using a beam splitter and brought to intersection with a lens. A collimator is used for adjusting the beam properties in the measurement volume and the Bragg cell provides a frequency shift used for the directional sensitivity. The Doppler frequency is determined using a single processor and the data analysis for computing flow properties is performed in a computer.

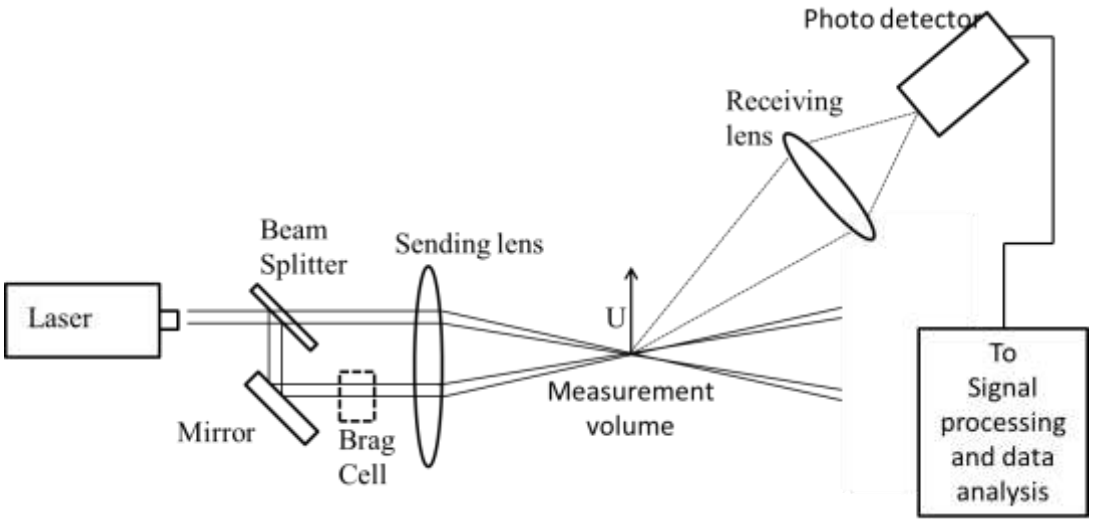

Figure 3.3-4 Sketch of dual-beam laser Doppler anemometer

It has to be mentioned that the LDV samples the flow velocity at discrete times corresponding to the passage of a particle through the intersection volume. The velocity sampled at these times can be considered as primary measurement quantity. The derivation of flow parameters or secondary measurement quantities, such as mean flow velocity, turbulent level or turbulence spectra, requires further data processing.

3.3.2 LDV Setup

A Dantec 2D Fiber-Flow optical system was used with a Spectra-Physics Stabilite 2017 argon-ion laser, and the Doppler signals were analyzed by two Dantec BSA processors. The LDV system was operated in the backscatter mode, and includes a Bragg cell to resolve directional ambiguity. The backscatter mode configuration is shown in Fig. 3.3-5, which integrates the transmitter and receiver in one probe.

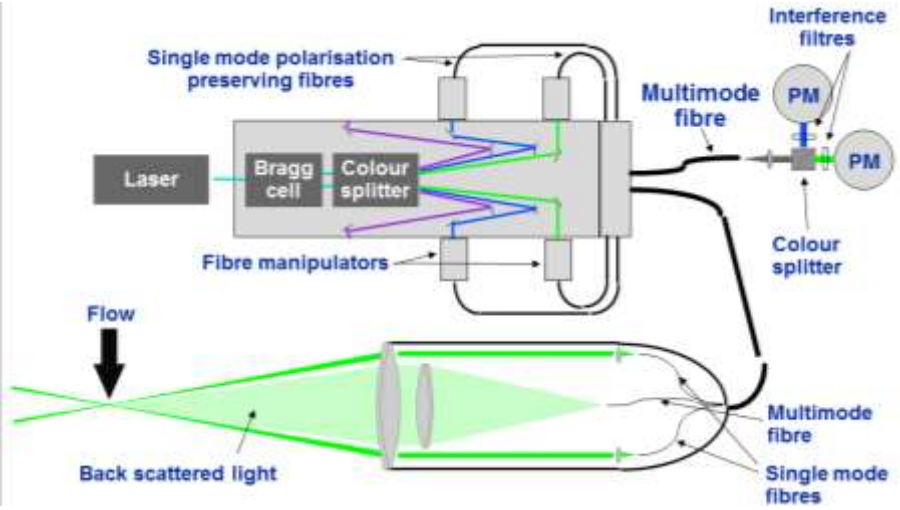

Figure 3.3-5 Sketch backscatter mode configuration of LDV

For cross-wise sections measurements, the laser beams entered from the exit section of the duct and were inclined to allow moving the probe volume in several cross planes (Y, Z) from a region close to the injection wall to the inner zone of the crossflow, which is illustrated in Fig. 3.3-6. Stream-wise measurements were obtained with the laser beams entering through the lateral wall of the duct, in order to measure the two velocity components in X and Z directions. In the first configuration a focal length of the transmitting optics of 600 mm has to be used, while in the second one the focal length was reduced to 300 mm with the addition of a beam expander, to reduce the probe volume dimensions. The grid spacing for all of the LDV measurements in this study is 1 mm.

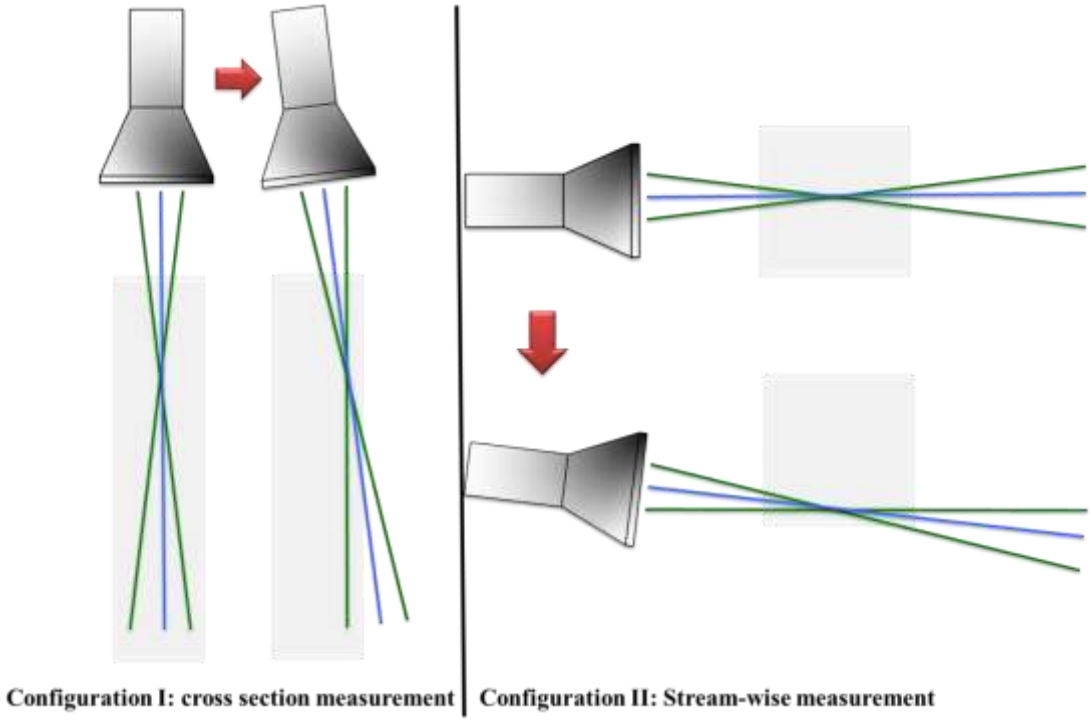

Figure 3.3-6 Illustration of different configuration for cross section measurement and streamwise measurement respectively in LDV experiment

Separate pneumatic atomizers were used to seed alternatively the crossflow or the jet with droplets smaller than 2 μm in diameter. This acquisition procedure has been implemented in order to distinguish between jet and crossflow velocity field. The maximum measurable frequency of the flow fluctuations, limited by the inertia of the tracer oil droplets, is estimated to be around 2 kHz [82]. LDV sampling rate ranged from 100 to 1000 Hz, depending on the measurement location and seeding procedure. The maximum statistical error at 95% confidence interval is estimate to be less than 5% with a number of statistically independent samples of at least 2000.

3.4 Hot Wire Anemometry

Hot wire anemometry (HWA) is the one of the most common method used to measure instantaneous fluid velocity [87, 88]. In this study, HWA was applied to determine the turbulence level at the outlet of duct, from which results the mixing level between jet and crossflow at far field could be predicted. This section gives a brief introduction of the principle of HWA, followed by the specific setup of HWA measurements in this work.

3.4.1 Principle of HWA

The technique depends on the convective heat loss to the surrounding fluid from an electrically heated sensing element or probe [89, 90]. If only the fluid velocity varies, then the heat loss can be interpreted as a measure of that variable. It enjoys its popularity because the technique involves the use of very small probes that offer very high spatial resolution and excellent frequency response characteristics. The basic principles of the technique are relatively straightforward and the probes are difficult to damage if reasonable care is taken.

HWA have been used for many years in the study of laminar, transitional and turbulent boundary layer flows and much of our current understanding of the physics of boundary layer transition has come solely from hot-wire measurements.

The sensor for HWA is, as the name implies, made from short lengths of resistance wire and is circular in section, since it could offer the greatest flexibility of use in restricted, often highly unsteady environments. One typical hot wire sensor is shown in Fig. 3.4-1

Figure 3.4-1 Typical hot wire sensor

To optimize the frequency response of an anemometer, the probe should have a thermal inertia as small as possible and this is consistent with the requirement of a small size. The

wire is supported on prongs that are embedded in non-conducting (often ceramic) material.

Again, the technique depends on the convective heat loss to the surrounding fluid from an electrically heated sensing element or probe. The physics of fluid flow and convective heat transfer are inextricably linked by relationships of the general form:

$$\text{Nu} = f\ (\ \text{Re, Pr, Kn, ...geometrical factors}\ ) \quad \text{(Eq. 3-19)}$$

where the Nusselt (Nu), Reynolds (Re), Prandtl (Pr) and Knudsen (Kn) Numbers are all non-dimensional quantities. In the context of a cylindrical thermal anemometer, the above equation may be expanded to give:

$$\frac{\dot{q} l_w}{{d_w}^2 (T_w - T_a) k} = f\left(\frac{\rho U d_w}{\mu}, \frac{\mu C_p}{k}, \frac{l_w}{l}, \cdots geometry\right) \quad \text{(Eq. 3-20)}$$

where ρ is the fluid density, U is its velocity and μ its viscosity, d_w is a typical dimension such as the hot-wire diameter, $\dot{q}$ is the heat loss, l_w is the wire length, k is the thermal conductivity, l is the mean-free path of the fluid, and T and T_a the temperatures of the wire and fluid respectively. The geometrical factors referred to include not only the length-diameter ratio of the cylinder l_w/d_w, but also quantities such as the support geometry for the cylinder and the orientation of the sensor with respect to the flow. It could be seen that the heat loss depends on many parameters.

In 1914, King L.V derived a solution for the heat transfer from an infinite cylinder in an incompressible low Reynolds number flow, referred as King's law:

$$\text{Nu} = A' + B'\ \text{Re}^{0.5} \quad \text{(Eq. 3-21)}$$

where A' and B' are constants, so that:

$$\frac{\dot{q} l_w}{{d_w}^2 (T_w - T_a) k} = A' + B' \left(\frac{\rho U d}{\mu}\right)^{0.5} \quad \text{(Eq. 3-22)}$$

The rate of heat loss to the fluid is equal to the electrical power delivered to the sensor V^2/R where V is the voltage drop across the sensor and R is its electrical resistance. If the fluid properties and wire resistance remain constant, this expression reduces to:

$$V^2 = A'' + B'' U^{0.5} \quad \text{(Eq. 3-23)}$$

where A" and B" are constants. When the conductive heat losses to the sensor supports or the substrate do not change with fluid velocity, the constant A may be replaced by the quantity V_0^2, where V_0 is the voltage across the sensor under zero flow conditions.

In practice, the voltage registered at the anemometer output is not that across the sensor but the e.m.f. E that is applied to the top of the Wheatstone bridge, the two arms of the bridge acting as potential dividers so that the relationship becomes in effect:

$$E^2 - A^2 = BU^{0.5} \qquad \text{(Eq. 3-24)}$$

The constant A may be replaced by the zero-flow voltage E_0 when high accuracy is not required. In practice, the value of the exponent changes with sensor and velocity as do the values of A and B, and therefore it's necessary to calibrate each sensor individually and to check this calibration frequently. An exponent of 0.45 is nearer to that found in practice.

Since no universal calibration is available, the sensors must be calibrated. To do this, a low turbulence flow of known velocity must be used. Ideally, the probe should be placed into it in the same attitude that it will be used. In use, errors arise due to changes in ambient temperature and other fluid properties and due to the deposition of impurities in the flow on the sensor. Standard procedures are available to correct for the effects of changes in temperature. For instance, one simple and widely available method is constant temperature anemometry (CTA) [89], which using a feedback circuit to maintain the wire at a constant temperature, shown in Fig. 3.4-2. The hot wire, shown between C and D, forms part of Wheatstone bridge, such that the wire resistance is kept constant over the bandwidth of the feedback loop.

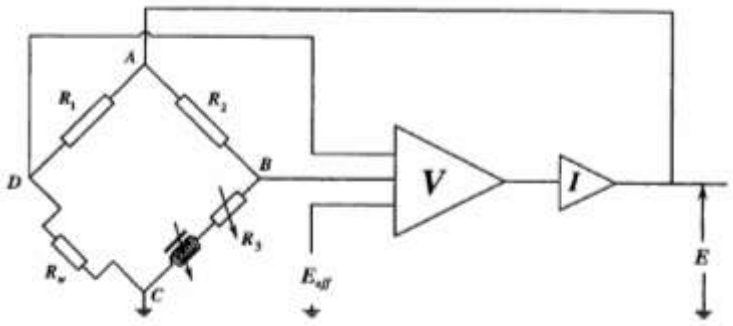

Figure 3.4-2 Schematic of a constant temperature HWA

Figure 3.4-3 shows a typical measurement situation where U is the mean fluid velocity that is normal to the wire and u', v' and w' are velocity fluctuations in three perpendicular directions. The axis of the sensor is aligned with the w direction so that the sensor will have a very poor response to the w component, providing that the length-diameter ratio of the sensor is large (i.e. l_w/d_w>200). Therefore, the sensor sees the effective cooling vector U' which, providing v' is not too large, has the same magnitude as (U+u'). Thus at low turbulence intensities the wire is measuring the magnitude of the velocity in the direction of the mean flow. Consequently, the stream-wise turbulence intensity $\sqrt{\overline{u'}/\overline{U}}$ can be derived by calculating the root-mean-square of the velocity-time history. In isotropic turbulence, this measurement and that of the mean velocity are in error by about 2% when the turbulence intensity is about 20 percent.

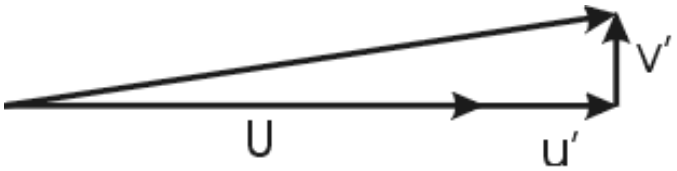

Figure 3.4-3 Mean (U) and Instantaneous (u') flow velocities

To obtain the components of turbulence that are normal to the mean flow vector, a variety of two and three sensor techniques are used to determine the magnitude and direction of the instantaneous flow vector. From this, the time-mean and turbulent flow properties may be found.

3.4.2 HWA Setup

In this study, a hot wire was set at the outlet of duct, where the measurements are performed. Fig. 3.4-4 shows a photo of HWA setup. As indicated in Fig. 3.4-4, the hot wire is parallel with jet axis (if the jet is normally injected into crossflow), thus the streamwise velocity information is mainly concerned here.

A hot wire made by DANTEC was used to in this study, with a resistance 3.57 Ω at 20 ℃. The voltage signal was transformed to digital signal through an A/D converter, and then analyzed by a home-made program.

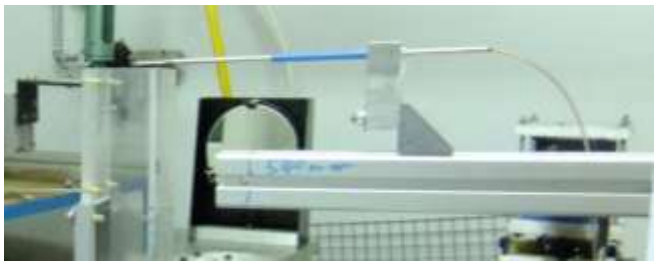

Figure 3.4-4 Setup of HWA measurement

3.5 Test Matrix

A wide range of conditions have been concerned in this study, referring jet-to-momentum flux ratio, injection orientation, and injection gas, which are also dependent on the various techniques applied. Detail of test conditions is summarized here: (Air has been selected for the crossflow throughout this work, and it will not be mentioned anymore)

3.5.1 Schlieren Imaging

The target of this schlieren imaging is to determine the topology of flowfield and select test conditions for the followed measurements. Gases with different density of air have been selected to be injected, to improve the sensitivity of schlieren images. Large ranges of jet velocity, crossflow velocity as well as jet-to-crossflow momentum flux ratio are considered, which are shown in Table 3.5-1.

Table 3.5-1 Experimental conditions used for the schlieren imaging tests

Jet to crossflow momentum flux ratio	2~7
Crossflow free stream velocity	1.7 m/s, 3.4 m/s
Injection gas	CO_2, Mixture (50%He + 50% N_2)
Injection orientation	45°, 60°,90°,120°,135°

It has to be noticed that a mixture of Helium and Nitrogen (with a volume fraction ratio 1:1) has been used in this study. This is aimed to simulate the density of methane

(ρ_m=0.671 kg/m^3 at normal condition), and to study the influence of the gas. For this case, jet Reynolds number is lower caused by the higher viscosity of mixture (ν_m=2.9x10^{-5} m^2/s) [90].

3.5.2 LDV Measurement

Compared with the large test matrix of schlieren imaging experiment, only several representative conditions were selected in the LDV measurements, which are summarized in Table 3.5-2.

Table 3.5-2 Experimental conditions used for the LDV

Jet to crossflow momentum flux ratio	2~7
Crossflow free stream velocity	1.7 m/s
Injection gas	Air, Mixture (50%He + 50% N_2)
Injection orientation	45°,90°,135°

Same as previous section, the detail of experimental conditions will be given in Chapter 5, which presents the results of LDV measurements and their relative analysis.

3.5.3 HWA Measurement

The HWA measurements have been mainly conducted at the outlet of the duct, trying to study the turbulence characteristics under different conditions. The selected test conditions are similar with those of LDV measurements. Thus they are not shown here; instead they will be given in chapter 6.

3.5.4 Flow Characterization

Considered that the square duct used in the present study is relatively small and its boundary layer may have a significant effect on jet evolution and penetration, it is necessary to characterize the crossflow generated during tests by LDV preliminary

measurements, in terms of flow uniformity, turbulence level and boundary layer thickness. Fig. 3.5-1 presents the time mean and RMS velocity profiles measured by LDV in the crossflow without the jet, and shows that the thickness of the boundary layer (defined as the 95% of U_{cf}) is 7.2 mm, thus the undisturbed area into the duct central region amounts to ~41% of the total cross-section. This observation underlines the importance of the boundary layer on the mixing process between jet and crossflow in such small geometry, not to mention its influence on the vorticity in the wake of the jet. The turbulence intensity is almost constant (≈10%) in the inner region of the flow, with a sharp increase at around 2 mm from the wall. The relative error on the measured mean velocity is estimated to be less than 1% in the free stream region and increases to about 3 % near the wall.

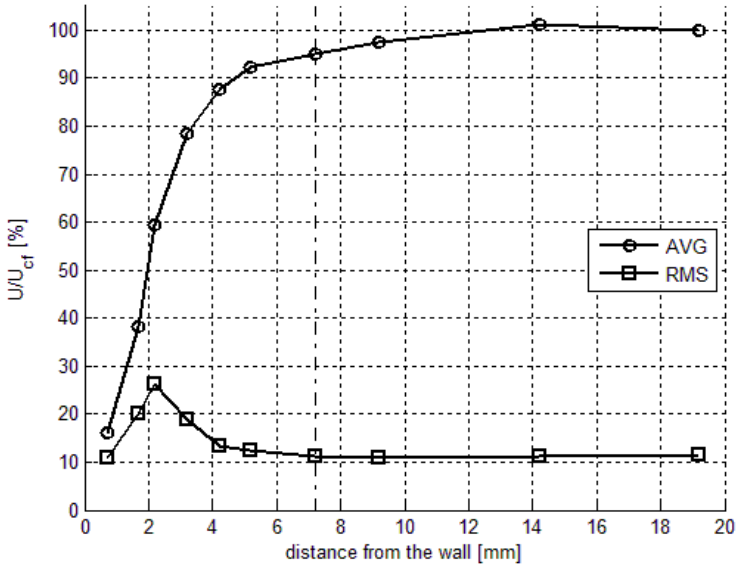

Figure 3.5-1 Mean (circles) and RMS (squares) velocity profiles of the crossflow measured by LDV at the nozzle exit cross-section. The dashed line shows the limit of the boundary layer where $U/U_{cf} = 0.95$

The velocity profile of the jet has been also characterized for the three investigated velocities. In that case, LDV measurements were performed by seeding the jet and the mean and RMS velocity profiles are shown in Fig. 3.5-2, as measured in the absence of the crossflow and at a distance from the jet exit, Z/D = 0.5. The jet exhibits a fully developed turbulent top hat velocity profile, which is more pronounced at higher jet outlet velocities. Highest turbulence intensity is measured at the edge of jet, which is around 20%, while in the core of the jet it amounts to less than 10%.

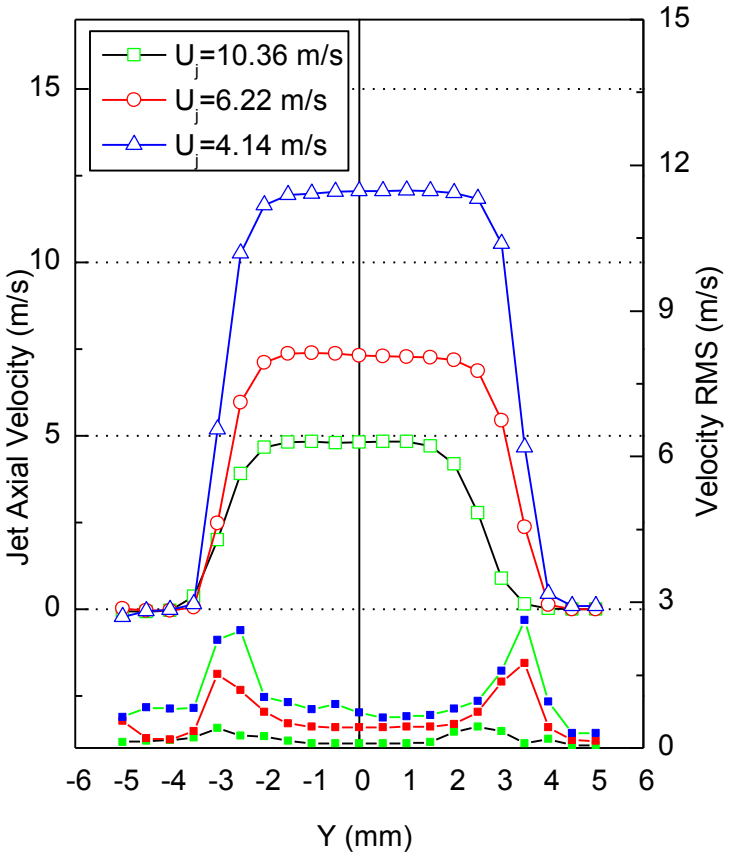

Figure 3.5-2 Mean and RMS velocity profiles at the nozzle exit (z/D = 0.5), measured by LDV

Here and in the rest of this thesis, U_j is the nominal jet velocity, which is calculated from the average volume flow rate, determined by a mass flow meter. This mass flow meter is shown in Fig. 3.1-1 as well.

It has to be noticed that for a naturally aspirated light duty engines with cylinder capacity of 0.5 liters, the intake air stream is around 2 m/s and the injected fuel flow is around 15 m/s when working at 1000 rpm, full load. Thus here both the velocities of the crossflow and of the jet are smaller. However, the jet-to-crossflow momentum flux ratio is comparable and thus this experiment can represent a generic scenario for the injection of gaseous fuel into an intake port.

To summarize this chapter, Table 3.5.3 gives a comparison of test rig and techniques applied in this work and some of other studies.

Table 3.5-3 Test rig and techniques in the literature works

Author	Test Rig	Range of R	Techniques	Active Control
Coelho L.V & Hunt J.C.	wind tunnel (1m ×1m)	10	Smoke flow visualization, HWA	no
Fric T.F. & Roshko A.	wind tunnel (0.5m × 0.5m)	2~10	Smoke flow visualization, HWA	no
Kelso R.M. & Lim T.T.	water channel, wind tunnel (1.2m ×0.9m)	2~6	dye visualization, HWA	included
Haven B.A. & Kurosaka M.	water channel (0.7m × 0.7m)	0.8, 1.6, 2	PIV, PLIF	no
Gogineni S. & Goss L.	air channel (6.35cm × 6.35cm)	1	Mie scattering, PIV	yes
Smith S.H & Mungal M.G.	wind tunnel0.54m × 0.54m)	5~25	PLIF	no
Rivero A. & Ferre J.A.	wind tunnel (0.6m × 0.6m)	3.8	HWA	yes
Hasselberink E.F., Mungal M.G.	wind tunnel(0.5m × 0.5m)	10,21	PIV	no
Camussi R. & Guj G.	water tunnel(0.1m × 0.1m)	1.5~4.5	PIV, PLIF, Dye visualization	no
Lim T.T & New T.H.	water tunnel(0.4m × 0.4m)	4.6	dye visualization	no
Gordan M. & Soria J.	water tunnel(0.25m × 0.25m)	4.6,7	PIV	yes
Meyer K.E. & Ozcan Oktay	water channel(0.04m × 0.04m)	3.3	PIV, LDA, PLIF, LIF	no
M'Closkey R.T., et al	wind tunnel (0.12m × 0.12m)	2.58	HWA, smoke visualization	yes

Narayanan S., et al	wind tunnel (0.1175m × 0.1175m)	6	HWA, Mie scattering	yes
Ozcan O. & Larsen P.S.	wind tunnel (0.3m × 0.6m)	1.3, 3.3	LDA	no
Peterson S.D & Plesniak M.W.	wind tunnel (0.3m × 0.3m)	0.5,1	PIV	no
Su L.K. & Mungal M.G.	wind tunnel (0.5m × 0.5m)	5.7	PIV, PLIF	no
Gopalan S. & Abraham B.M.	water tunnel(0.145m × 0.145m)	0.5 ~ 2.5	PIV	no

CHAPTER 4

SCHLIEREN IMAGING

Schlieren imaging provides a non-intrusive, time resolved method for flow visualization. Although schlieren images are mainly qualitative, they can offer preliminary understanding of the physical behavior and provide interesting information on turbulent and non-stationary flow structures, as introduced in previous chapter. In this study, schlieren images of jet transverse injection into crossflow have been firstly captured to study the topology of the flow field and select experiment conditions for the consequent measurements. The main flow features of jet into confined crossflow under wide range of various conditions will be described based on the results of schlieren images.

4.1 Macro Flow Structures

Fig. 4.1-1 to 4.1-3 show side view schlieren images providing the typical instantaneous jet structure in the stream-wise (X, Z) direction, for three value of the jet-to-crossflow momentum flux ratio R=2.44, 3.66, 6.10 respectively. Here CO_2 has been injected due to its relative large difference of density with air, which can improve the sensitivity of schlieren images. The crossflow is maintained as 1.7 m/s for all of these three images. Each image here has been individually corrected by subtracting a mean background image. A chain of vortices has been found along the upward of the jet, which is so called shear layer vortices and becomes distorted with streamwise distance. These vortices have been interpreted to be the result of instability similar to the Kelvin-Helmholtz instability of the annular shear layer that separates from the edge of the jet orifice [20]. Similar ring

like vortices formed from the jet shear layer were observed at values of $R \geq 3$ and attributed to jet-like structures [8, 9, 19]. It was also found that the formation of these vortices is related to the jet Reynolds number (Re_j). In addition, it has been suggested that folding of the vortex rings leads to the initiation of the CVP [8, 9, 13].

From Fig. 4.1-1 to 4.1-3, it is clear to see that the evolution of the vortical structures and jet penetration depends strongly on the value of *R*. When jet-to-crossflow momentum flux ratio is as low as 2.44, the jet is entirely deflected by the crossflow and does not reach the opposite wall before it moves far downstream (Fig. 4.1-1).

As *R* is increased to 3.66, moderate confinement to the jet's development can be observed by the schlieren image (Fig. 4.1-2), after the deflection of the jet, around 1.5 diameters downstream of nozzle center. This confinement on the nearfield development of the jet is found when *R* is larger than 3, with the experimental setup of this study. When *R* is lower than 3, the jet's penetration is too small and can reach the opposite wall only far downstream. In addition, this interaction between jet and wall seems to favor the jet dispersion and mixing with crossflow, based on the results of schlieren images.

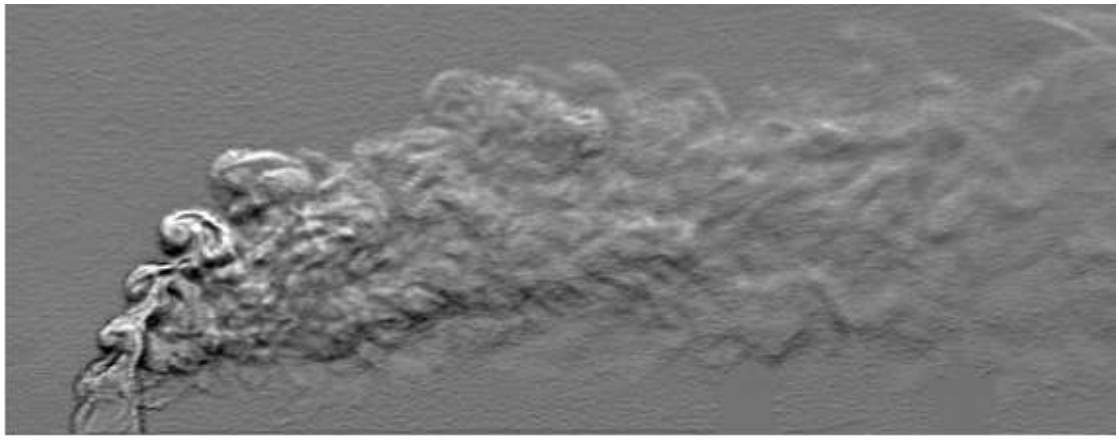

Figure 4.1-1 Instantaneous schlieren image of jet in crossflow, R=2.44, U_j=3.26m/s, U_{cf}=1.7 m/s; CO_2 injected

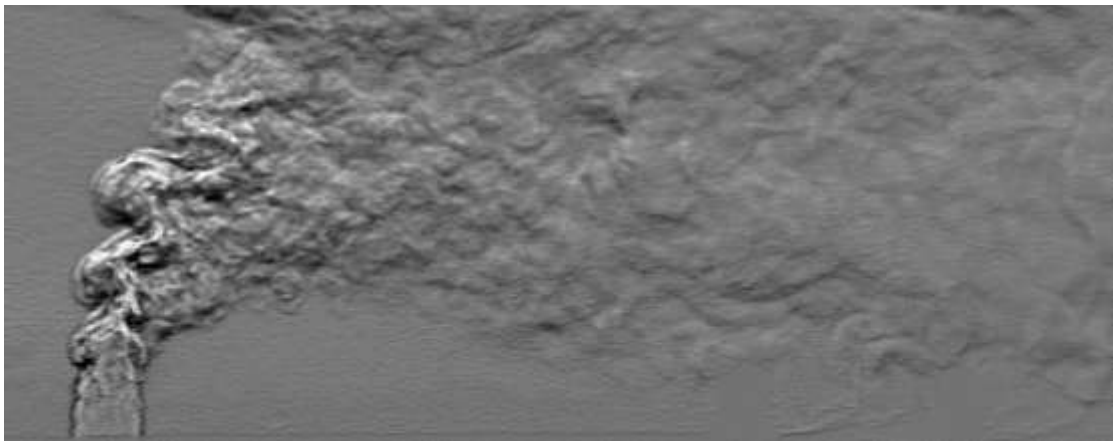

Figure 4.1-2 Instantaneous schlieren image of jet in crossflow, R=3.66, U_j=5.04m/s, U_{cf}=1.7 m/s; CO_2 injected

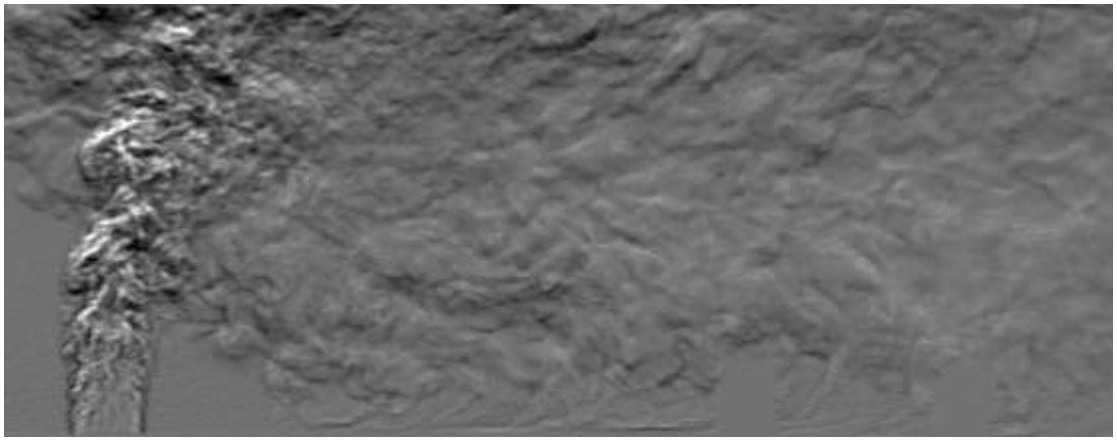

Figure 4.1-3 Instantaneous schlieren image of jet in crossflow, R=6.10, U_j=8.41m/s, U_{cf}=1.7 m/s; CO_2 injected

With a further increase of *R* up to 6.10, the confinement to the jet development from the wall becomes more effective, as clearly shown in Fig. 4.1-3. At this condition, the jet impinges on the opposite wall, even before complete deflection by the crossflow. In addition, interaction between the jet and the crossflow can be observed even near the injection plane from 2 diameters downstream of the nozzle center, indicating a rapid 3 dimensional spread of jet after impingement on the opposite wall.

Another interesting phenomenon is the development of shear layer vortex. It seems that these shear layer vortex are more clearly shown in Fig.4.1-1 and Fig. 4.1-2, when *R* is lower than 4. This infers the relation between rolling up of these shear layer vortex and deflection of jet by crossflow, since the shear layer vortex are well announced at the deflection upstream side of jet. Clearly, the deflection of jet caused a pressure gradient

above this region, which can provide strength for the enlargement of those shear layer vortex.

The effect of jet-to-crossflow momentum flux ratio *R* on the flow field has been clearly illustrated by Fig. 4.1-1 to Fig. 4.1-3. In order to verify the dominant influence of *R*, schlieren images of jets with same *R* but various velocities have been captured as well. Fig. 4.1-4 shows the schlieren images of jet that has an *R* equal to 2.44, but higher jet outlet velocity as well as higher crossflow velocity. This is to compare with Fig. 4.1-1, and the flow fields in both two cases are similar with each other, despite that Fig. 4.1-4 shows smaller undisturbed area, caused by larger amount of jet gas injected. For the same reason, Fig. 4.1-4 shows contact between jet and opposite wall in a manner. In addition, due to the increasing of both velocities of jet and crossflow, their Reynolds numbers also increase. As a result, the shear layer vortices seem less announced, and break up more rapidly than the case with lower velocities of jet and crossflow.

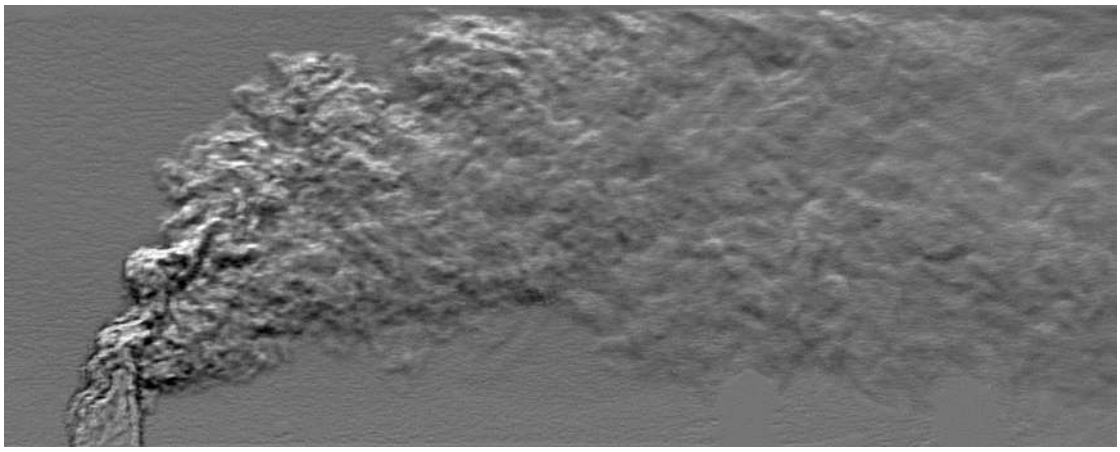

Figure 4.1-4 Instantaneous schlieren image of jet in crossflow, R=2.44, Uj=6.52m/s, U_{cf}=3.4 m/s; CO_2 injected

Fig. 4.1-5 shows the schlieren image of jet injected with mixture under same *R* with that of Fig. 4.1-2. The flow fields between these two cases are similar as expected, although different brightness in the image caused by different density of gas injected. Whether the separation between the two gases (helium and nitrogen) exists has not been identified in this experiment and needs to be study further.

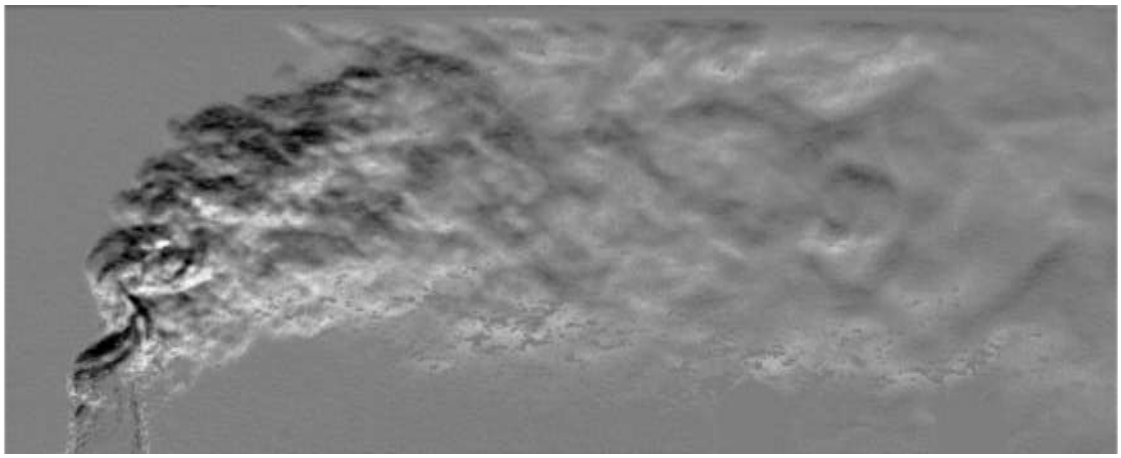

Figure 4.1-5 Instantaneous schlieren image of jet in crossflow, R=3.66, U_j=8.35m/s, U_{cf}=1.7 m/s; Mixture injected

For a short conclusion, the results of schlieren images confirm that *R* is the dominant parameters to define the flow field, while Reynolds number could influence the flow in a limit range.

4.2 Different Injection Orientation

Jets injected both in the streamwise and counter-streamwise orientations have been concerned in this study. Fig. 4.2-1 and Fig. 4.2-2 shows the schlieren image of streamwise injection of jet under high jet-to-crossflow momentum flux ratio, with an injection angle 45 °and 60 °with crossflow respectively. The injection angle is defined as the angle between jet axis and crossflow, which is shown in Fig. 4.2-3. With this definition, the jets normally injected into the crossflow, described in last section, have an injection angle of 90 °. In this study, only jets inclined in the (X, Z) plane have been considered. When the injection angle is less than 90 °, it is also called streamwise injection. Similarly, when the injection angle is larger than 90 °, it is called counter streamwise injection. Both the streamwise injection and counter streamwise injection are indicated in Fig. 4.2-3 (c).

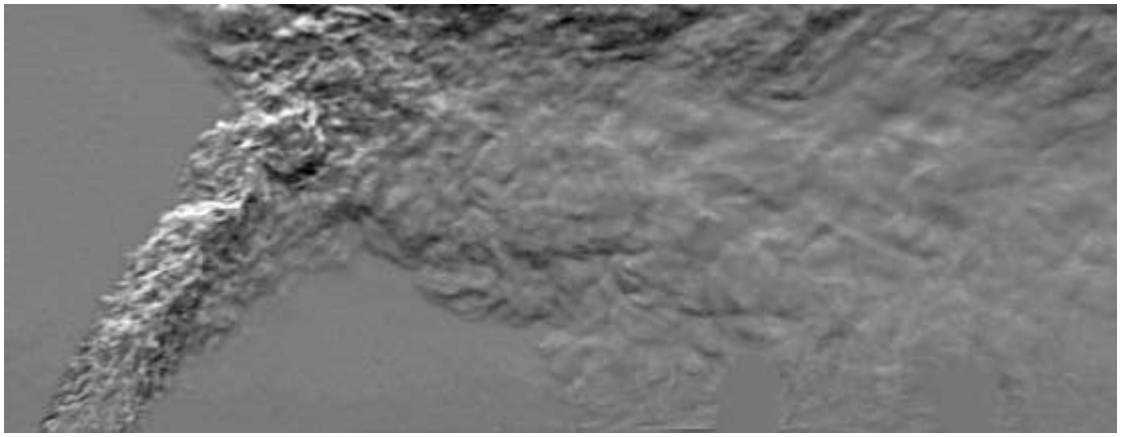

Figure 4.2-1 Instantaneous schlieren image of jet in crossflow, R=6.10, U_j=8.41m/s, U_{cf}=1.7 m/s; CO_2 injected; injection angle: 60 °with crossflow

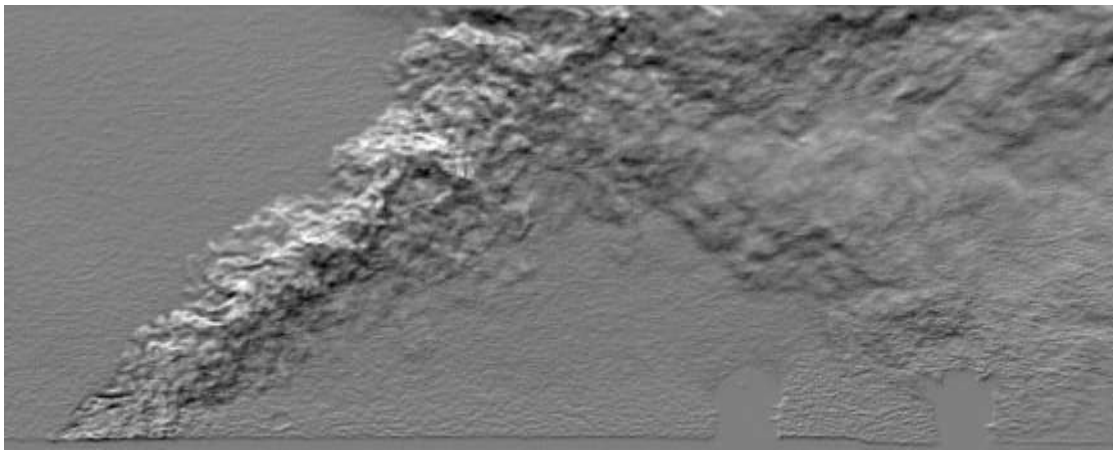

Figure 4.2-2 Instantaneous schlieren image of jet in crossflow, R=6.10, U_j=8.41m/s, U_{cf}=1.7 m/s; CO_2 injected; injection angle: 45 °with crossflow

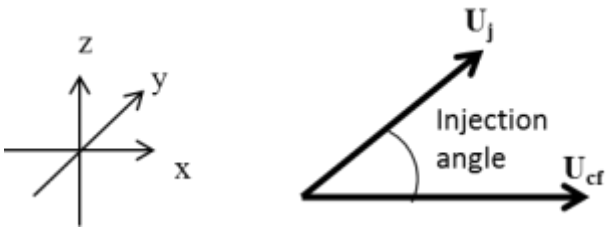

(a)

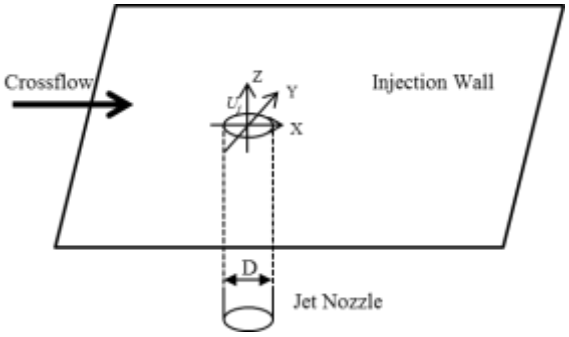

(b)

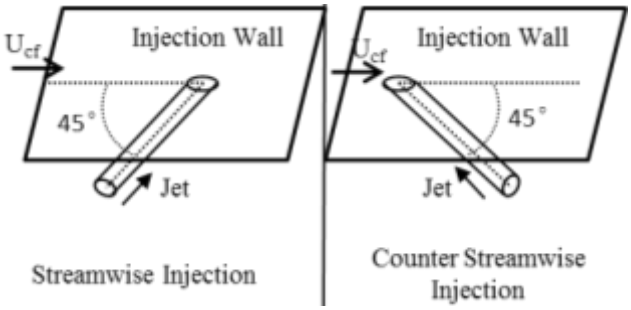

(c)

Figure 4.2-3 Injection configuration (a) Definition of injection angle, note that jets were only inclined in (X, Z) plane in this study; (b) Schematic diagram of the jet nozzle mounted flush with the injection wall (c) The injection with different injection orientation

In the case of streamwise injection, shear layer vortices are no more observed here. In the case of normal injection, a pressure gradient exists along the jet upward edge, which is supposed to provide strength for the vorticity in the shear layer to roll up, as shown in Fig. 4.1-1 to Fig. 4.1-2. This pressure gradient might vanish in the case of streamwise injection as the jet penetrate directly to the opposite wall, which seems like a cylinder inclined between two sides of the duct. Due to this reason, the strength of those shear layer vortices could be decreased as the decreasing of pressure gradient, and thus cannot be observed here.

In addition, as the injection angle is decreased, which means the jet is more inclined to crossflow, more undisturbed area could be observed in the schlieren images, particular in the ‘wake’ region. These undisturbed areas infers litter interaction between jet and crossflow, thus it can indicate a poor mixing between jet and crossflow in the near field if the jet is inclined to the crossflow. In the far field, thanks to the confinement of the opposite wall, the jet started to be broken and move back to the injection plane. It seems that the macro mixing between jet and crossflow starts only from this point.

When the jet is injected against the crossflow, the flow field is changed greatly, as shown in Fig. 4.2-4 to 4.2-6, which has an injection angle of 135 °. Generally speaking, the flow field behaves like a struggle between the jet and the crossflow. The jet firstly penetrates into the crossflow, forcing the crossflow to circumvent it. Then the axial velocity would be decreased quickly due to the blockage from the crossflow. Finally, the jet is turned greatly to move to downstream. Particularly, compared with those cases with normal injection and streamwise injection, the undisturbed ‘wake’ region does not exist in the case of counter-streamwise injection anymore, within all range of R concerned. This suggesting part of jet entrained in this area and mixed with crossflow in some degree.

While the R is low, shown in Fig. 4.2.4, the jet is completely turned to move to downstream, after a short penetration into crossflow, which is comparable with that of jet with same R but normal injected. From the schlieren image, it seems that the crossflow breaks up the main structure of jet, and blow it off after bending it. Rapid mixing between the jet and the crossflow could be inferred as well, which is caused by the strong interaction between them. Same as the case of normal injection of jet with same R, there is not much contact between the jet and the opposite wall until downstream.

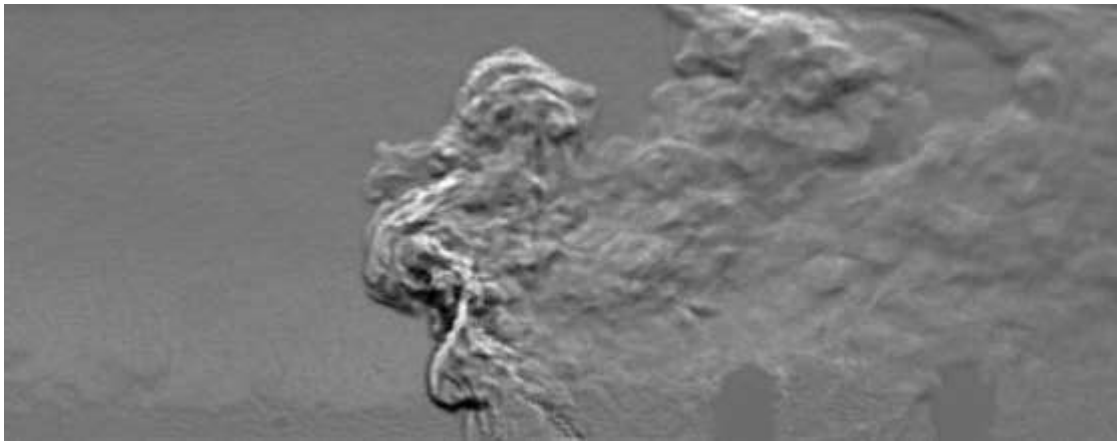

Figure 4.2-4 Instantaneous schlieren image of jet in crossflow, R=2.44, U_j=3.26m/s, U_{cf}=1.7 m/s; CO_2 injected; injection angle: 135 °with crossflow

When *R* is 3.66, shown in Fig. 4.2-5, the jet stops penetration before impact on the wall. However, some interaction between jet and crossflow can be observed in the area above the end of the jet penetration, indicating the influence of duct wall.

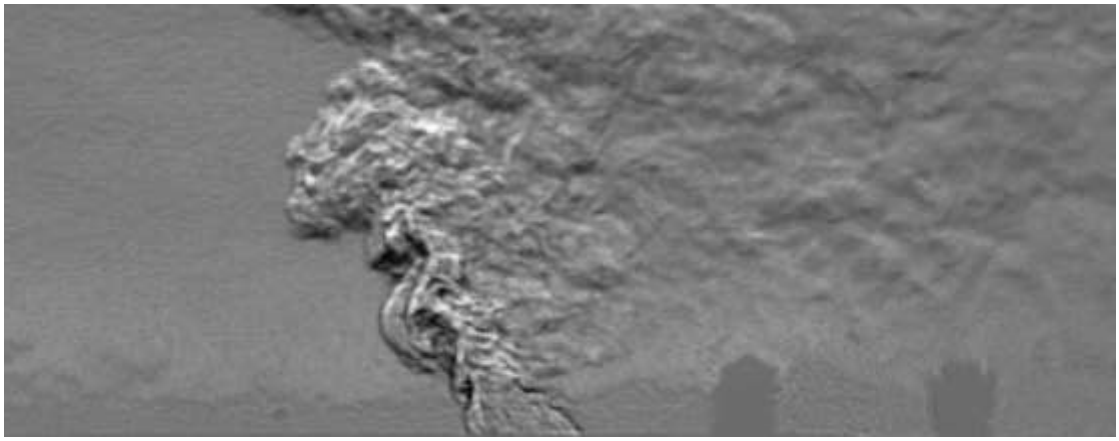

Figure 4.2-5 Instantaneous schlieren image of jet in crossflow, R=3.66, U_j=5.04m/s, U_{cf}=1.7 m/s; CO_2 injected; injection angle: 135 °with crossflow

In this schlieren image of counter streamwise injected jet with high jet-to-crossflow momentum flux ratio, the jet seems like a cylinder, similar to the streamwise injection but differently inclined. The shear layer vortices are not clearly shown as well. The crossflow moves around the jet, bringing part of the jet gas from its upstream boundary, and flowing downstream. The interaction region among the jet, the crossflow and the opposite wall seems similar to that at normal injection.

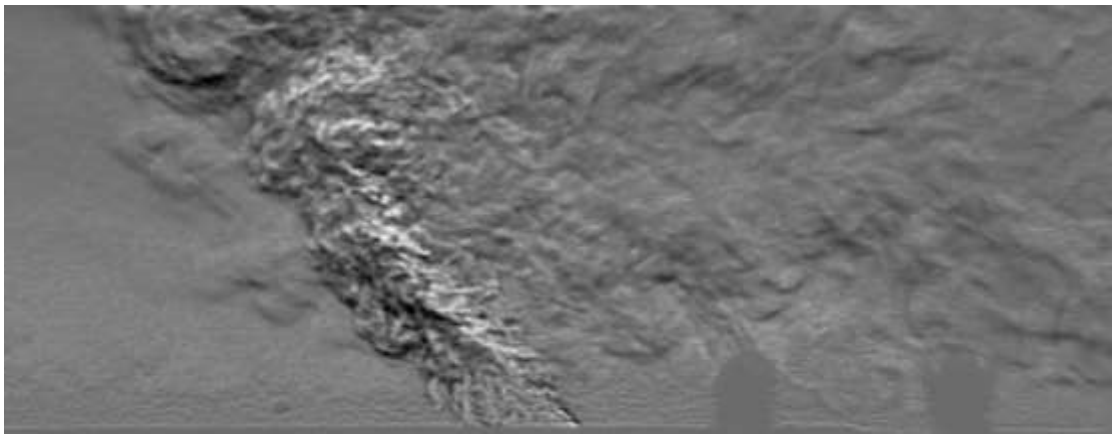

Figure 4.2-6 Instantaneous schlieren image of jet in crossflow, R=6.10, U_j=8.41m/s, U_{cf}=1.7 m/s; CO_2 injected; injection angle: 135 °with crossflow

In a short summary, the injection orientation is observed to play a critical role in the development of flow field, and thus changes the jet - crossflow mixing process greatly. Specifically, the counter-streamwise injection is found to enhance the mixing between jet and crossflow, which the streamwise injection is found to influence the mixing negatively.

CHAPTER 5

LDV MEASUREMENTS

The macro flow structures have been discussed in last chapter based on the results of schlieren images, which illustrate well the complexity of the flow field. In order to understand the development of flow field, LDV measurements have been conducted at center plane and several cross sections. The phenomena observed by schlieren images could be explained well with the results from LDV measurements. Detail of test conditions should be given Table 5-1.

Table 5-1 Experimental conditions used for the LDV

Case	R	U_{cf}(m/s)	U_j (m/s)	Re_{cf}	Re_j	Injection Orientation
Jet1N	3.7	1.7	6.22	4500	2630	Normal
Jet2N	6.1	1.7	10.36	4500	4400	Normal
Jet2S	6.1	1.7	10.36	4500	4400	Streamwise
Jet2CS	6.1	1.7	10.36	4500	4400	Counter-Streamwise
Jet2M	6.1	1.7	13.94	4500	3070	Normal

The jet has been studied firstly with Normal injection in the LDV measurements, indicated by the capital letter 'N' in the case name in the table above, with two jet-to-crossflow momentum flux ratios. Then the jet nozzle was inclined at 45 °and 135 °, with respect to the crossflow, as indicated in previous chapter. The two inclinations are referred to as Streamwise injection and Counter-Streamwise injection, indicated by the capital letter 'S' and 'CS' in the case name respectively. All the cases considered in this paper for LDV measurements refer to injection of air, as mentioned previously, except the last case, named 'Jet2M', which refers to the injection of a Mixture of helium and nitrogen (with a volume fraction ratio 1:1). This is aimed to simulate the density of methane and to study the influence of the gas composition, as mentioned in Chapter 3. Again, when the gas mixture was applied, the jet outlet velocity was adjusted to obtain the same jet-to-crossflow momentum flux ratio, according to Eq.2-1. Consequently, the jet Reynolds number changes as well.

5.1 Preliminary Test

Since different LDV configurations have been implemented during the measurements at different locations, it is necessary to understand the influence from various configurations on the velocity measurement results. In addition, the seeding flow is supposed to have effect in some manner as well. Thus several preliminary tests have been performed to identify those influences

5.1.1 Effects of Seeding Flow

Oil droplets have been utilized to trace the flow, seeded from crossflow and jet simultaneously, as introduced in Chapter 3. Considered the jet flow is relative small, only seeding the jet could not reach enough data rate. If only the crossflow is seeded, the sample rate in the jet potential core is quite low, and the acquisition error is relative large. Thus seeding both flows is required, even though seeding the jet might cause slight change on the flow rate, and consequently the jet-to-crossflow momentum ratio is changed slightly as well, because the relative small flow rate of jet is more sensitive to the ambient influences.

Fig. 5.1-1 shows the comparison between the results of LDV measurement by different seeding method: seeding only the crossflow (left) or seeding both jet and crossflow (right). Here the velocity and turbulence kinetic energy (TKE) maps at two cross-sections, X/D=0 and X/D=5, are shown, aiming to present the effect of seeding configuration on both near and far filed of the flow. The velocity is indicated by vecotors, while TKE is expressed as color contours, and is calculated from RMS of two available velocity components:

$$TKE = \frac{1}{2}\sqrt{U_x'^2 + U_z'^2} \qquad \text{(Eq. 5-1)}$$

Both mean velocity and TKE are scaled by the free stream velocity of the crossflow U_{cf} before plotting, as in the rest of the paper.

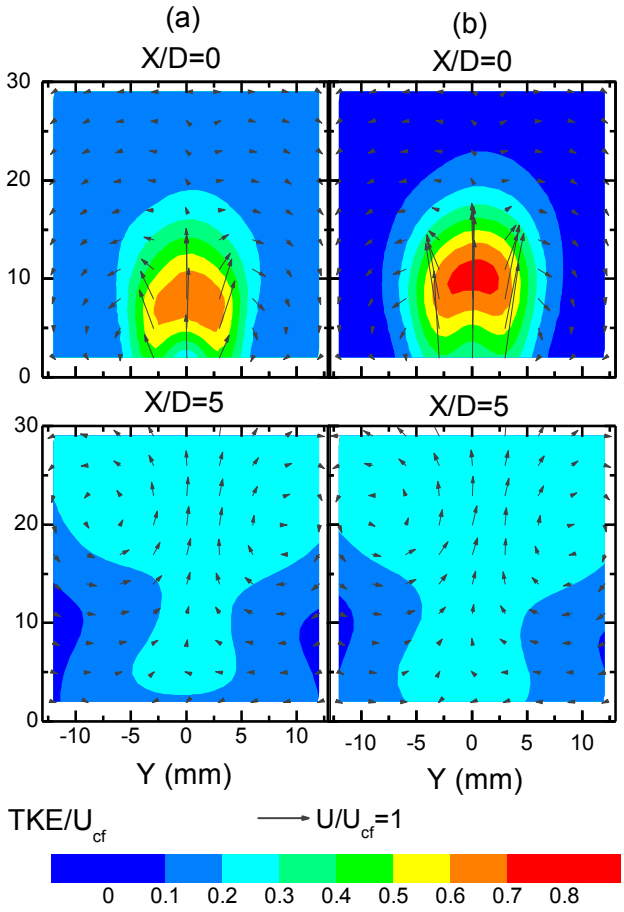

Figure 5.1-1 Comparison between the results of LDV measurement by different seeding: (a) seeding only the crossflow (b) seeding both the crossflow and jet, case Jet1N.

The main difference caused by different seeding configuration is observed at near field. When only the crossflow is seeded, the magnitude of velocity in the jet potential core region is slightly lower than that when both flows are seeded. In addition, the direction of velocity vectors in that region is tilted to two sides. These two phenomena indicate a lower jet flux, when only crossflow is seeded. However, jet flux was maintained constant during the measurements.

This effect should not be related to particle dynamics which is controlled by the Stokes number defined as the ratio of the aerodynamic response time of the particle, t_p, and the appropriate fluid time scale, t_f. Assuming Stokes flow, t_p is defined as:

$$t_p = \rho_p d_p^2/18 \qquad \text{(Eq. 5-2)}$$

where ρ_p and d_p are the particle density and diameter respectively, and μ is the fluid viscosity. In the jet near field, the appropriate fluid time scale may be assumed [91]:

$$t_f \approx 2L_v/U_j \qquad \text{(Eq. 5-3)}$$

based on a length scale L_v equal to the vortex core diameter and a vortex propagation velocity assumed to be half the jet exit velocity. When $t_p << t_f$, a particle would respond completely to the flow and in all the three investigated cases the above condition is fully satisfied. However, the measures also revealed a very low sampling rate indicating a poor entrainment of crossflow into the jet potential core. This effect, together with the length of the LDV probe volume (≈ 8 mm, oriented normally to the jet axis) for that particular optical configuration, could explain a mean velocity biased toward lower values probably originated by few particles crossing the edge of the jet.

At farfield, the influence of seeding configuration is observed to be negligible, and the measurement results under two seeding configurations are generally the same, which are shown in Fig. 5.1-1 as well.

Again, since seeding only the crossflow results limited sample rate in the near field, seeding both the crossflow and jet is applied. And all of the LDV data reported in the rest of this thesis were acquired from measurements when both the crossflow and jet were seeded.

5.1.2 Effects of Optics configuration

As introduced in Chapter 3, two optics configurations were selected, in order to measure the flow field at streamwise center plane and several cross sections. The transverse velocity component (U_z) at jet axis has been measured with both optics configuration, thus it is necessary to compare these results. This can also verify the accuracy of LDV measurement.

Figure 5.1-2 shows the comparison of results between the results of transverse velocity measurement of Jet1N along the jet axis, with two optical configurations. The configuration I is specified to cross section measurements, while configuration II is specified to streamwise measurements. Again, the detail of these two configurations could be found in Chapter 3 (recall Fig.3.3-6).

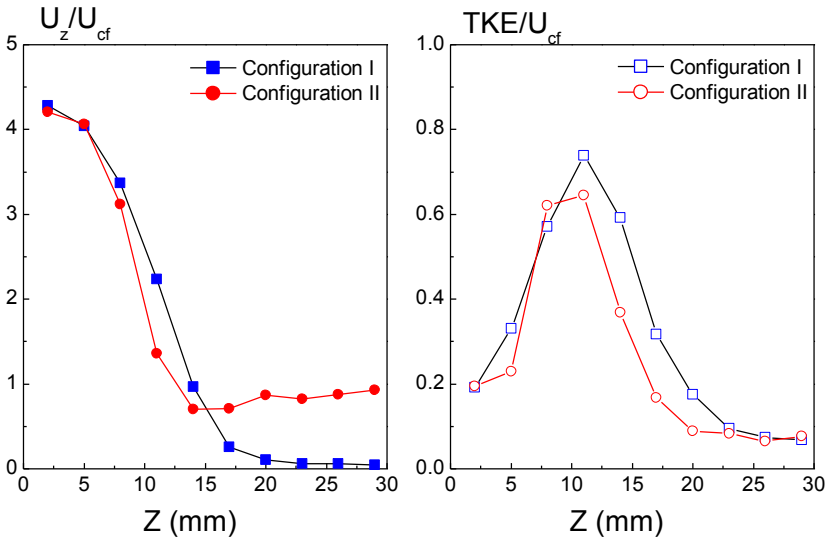

Figure 5.1-2 Comparison between the results of transverse velocity measurement, with two optical configurations, case Jet1N, X=0, Y=0

The transverse velocity profiles along the jet axis acquired by two configurations are approximately the same before the jet's deflection, as well as the TKE profile. Here the TKE profile is also RMS profile of transverse velocity. The difference in the fourth point in the mean transverse velocity profile might be caused by uncertainty of alignment. Nonetheless, larger transverse velocity and smaller TKE are observed when configuration II is applied. This is because that the probe volume of configuration II is as long as 8 mm. Thus droplets at downstream, which is inside the jet and thus have relative

large transverse velocity component, are also identified by the detector. Consequently, the mean velocity at this region detected with this configuration is increased. The difference of TKE profile acquired with two configurations is generally small. The scattering light from oil droplets must pass the transparent duct before detected, and the impurity inside wall will scatter this light in a small manner, which might increase the results of RMS, and thus the results of TKE.

5.2 Mean Velocity and TKE Field at Center Plane

5.2.1 Jet with Normal Injection

The mean velocity map and turbulence kinetic energy (TKE) distribution in the center plane of case Jet1N is shown in Fig. 5.2-1. The shear layer vortices found in the instantaneous schlieren image are not visible in the mean velocity map, indicating the instability of these shear layer vortices. However, a stable singular point is observed at the lee side of the jet, where X=9 mm and Z=4 mm, which separates the flow field in the wake region into reverse and forward flow areas, and that looks like a locally 2-dimensional emitting flows. In fact, the crossflow, after passing around the jet potential core, reenters into the center plane at this singular point, where it is dispersed then in all directions. The reversing flow portion indicates a pressure gradient at the leeside, and is entrained into the jet. Similar vortex is found in the study of [20, 39]. They also speculated the contribution to the formation of CVP from this singular point.

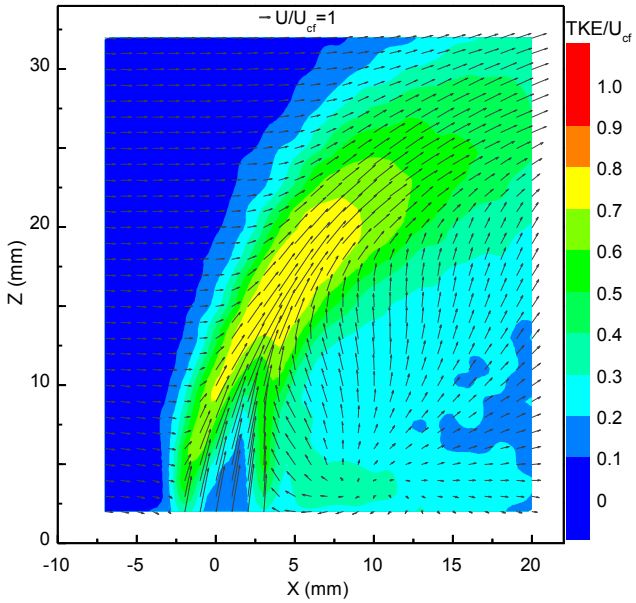

(a)

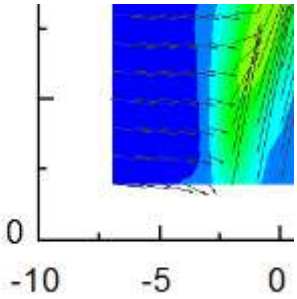

(b)

Figure 5.2-1 (a) Mean velocity vectors and TKE field at center plane, case Jet1N (b) Magnified view of the region at upstream corner of jet

In addition, the presence of a vortex can be deduced, at the upstream of the jet exit, which is shown in the magnified view in Fig. 5.2-1 (b). This suggests the existence of the horseshoe vortex, which is found to be steady with no periodic vortex shedding by Kelso [8]. This horseshoe vortex system is induced by the adverse pressure gradient in the pipe on the upstream side, extends to downstream, either incorporated into the vortex system of the wake, or lifted away from the wall behind the jet and merge with the CVP. Nonetheless, Fric and Roshko [7] suggest that the horseshoe vortex system seems to play only a minor role in the overall structure.

The TKE contour shows that maximum turbulence occurs along the shear layer and where the deflected crossflow mixes with the jet, indicating that maximum entrainment of

crossflow into jet happens there. This could be also inferred from schlieren image of same jet into crossflow shown in last chapter. In the same region in the schlieren image (Fig. 4.1-2), the shear layer vortices start to break up and the flow become more heterogeneous.

Fig. 5.2-2 shows the mean velocity and TKE field at center plane for Jet2N. Here, additional LDV measurements have been performed near the opposite wall by turning the probe to this side, as mentioned in the experimental setup section, to obtain data close to the wall. In addition to those two structures found in the case of Jet1N, another vortex can be observed upstream of the impact zone (X3, Z38), in Fig. 5.2-2, which indicates the stagnation of the crossflow induced by the jet. In the shear layer of the jet, the flow is deflected toward the opposite wall, where it impacts, and inducing a lateral spreading (±Y) of the crossflow.

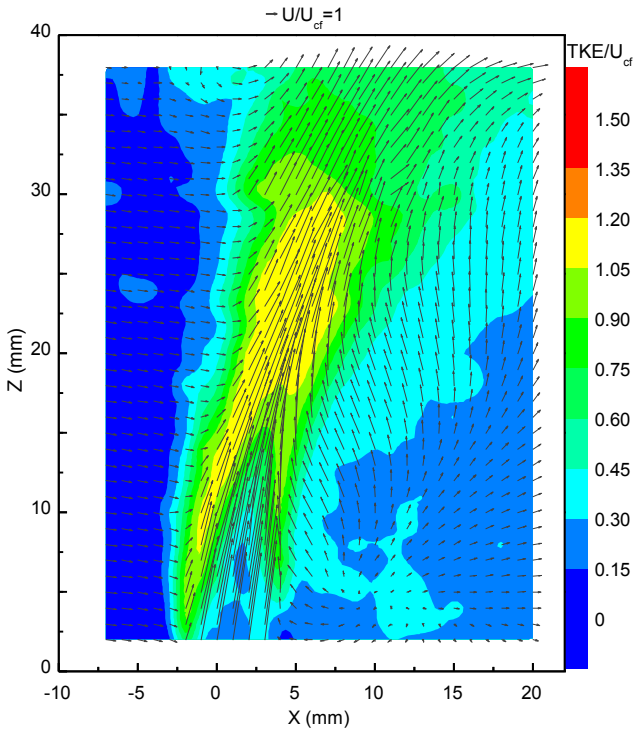

Figure 5.2-2 Mean velocity vectors and TKE field at center plane, case Jet2N

The maximum TKE is found again at the deflection region of the jet, although the magnitude of turbulence kinetic energy is much higher than that of the previous case. However, the turbulence level in the wake region is comparable between these two cases, Jet1N and Jet2N, suggesting a low influence of the jet-to-crossflow momentum flux ratio, at least in the studied range of *R*. However, it has to be stated that the flow in this wake region is different and distinct from the classical shedding of vorticity from solid

cylinders, according the smoke flow visualization [7], although the jet potential core looks like a cylindrical obstacle.

5.2.2 Streamwise Injection and Counter-Streamwise Injection

Jets injected both in the streamwise and counter-streamwise orientations have been concerned in this study. Fig. 5.2-3 shows its mean velocity and TKE field at center plane for the case of streamwise injection (Jet2S).

Generally, the velocity and TKE map of Jet2S shows a poor mixing between the jet and the crossflow in the near field under this condition. Same phenomenon has been found in the schlieren image (Fig. 4.2-2) as well. Previous studies [92] have proved that the shear layer vortices have strong relation with the formation, strengthening and evolution of CVP, which is believed to enhance the mixing between jet and crossflow. It can be conjectured that the poor mixing in the near field in this case is related with vanishing of shear layer vortices, which is found in the schlieren image.

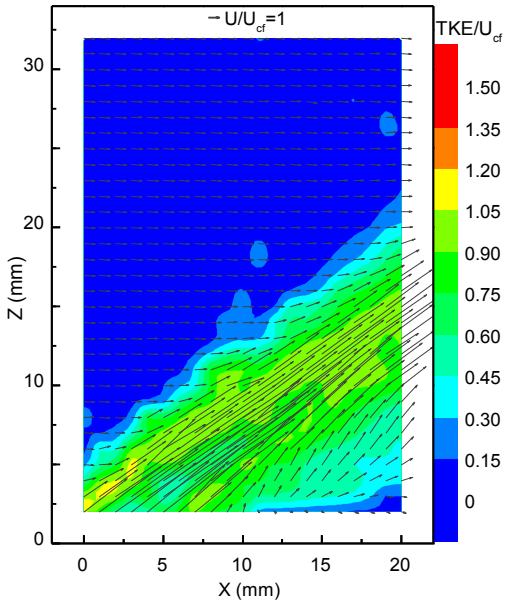

Figure 5.2-3 Mean velocity vectors and TKE field at center plane, case Jet2S

When the jet is injected against the crossflow, the flow field is changed greatly, which has been proved by the schlieren image (Fig. 4.2-4 to 4.2-6). The velocity and TKE map of Jet2CS, which has high jet-to-crossflow momentum flux ratio, is shown in Fig. 5.2-4.

In the upper left area of Fig. 5.2-4, all of the flow is moving directly towards the opposite wall. Considering that downstream of the injection cross-section (X>0), the jet is turning to move in streamwise direction, the flow structure indicates a strong interaction between the jet and the crossflow happening here. In addition, the reverse flow at the 'wake' region exists only close to the injection wall, indicating reduced pressure gradient there.

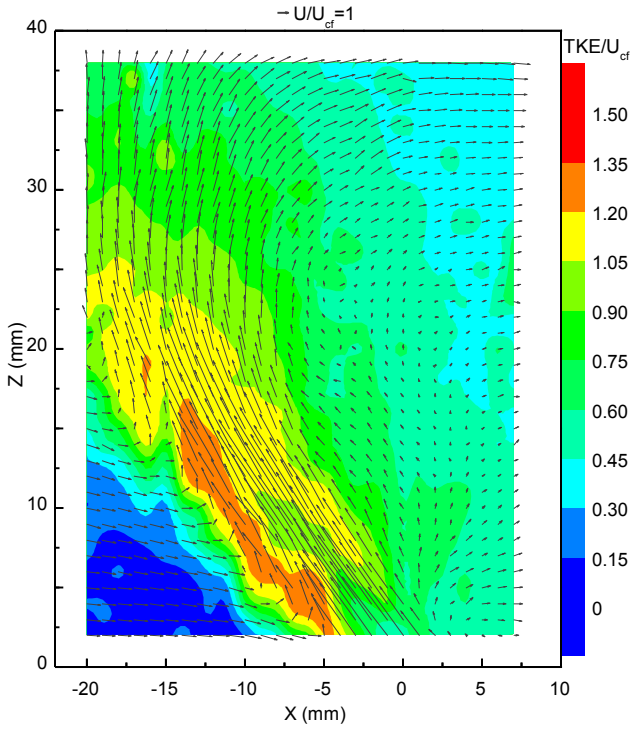

Figure 5.2-4 Mean velocity vectors and TKE field at center plane, case Jet2CS

The TKE level inside the jet is general higher than that of Jet2N and Jet2S. And the maximum of TKE in this tested area occurs at the upward side of jet, close to the injection wall, which is different from the previous two cases again. In addition, velocity and TKE map shows that the jet and crossflow are better mixed at 1D downstream of the jet center, compared with Jet2N and Jet2S, which results in a more uniform flow field. This is consistent with the result of schlieren image (Fig. 4.2-6)

5.3 Mean Velocity and TKE Field at Cross-sections

5.3.1 Jet with Normal Injection

Due to the complexity of the flow field caused by the jet injected into the crossflow, LDV has been done at several cross-sections as well, to study the streamwise flow development. Fig. 5.3-1 shows the mean velocity map and TKE distributions at several cross sections (X/D=0, 1, 2, 5), for the case Jet1N. The well mentioned structure of CVP has been observed in the velocity map, at all the range of *R* tested in this study, up to far field, while the jet is injected normal to the crossflow. This CVP structure is found to appear at the jet exit plane, X/D=0, on each side of the jet axis, although the location and strength of the vortices depend on *R*. This CVP causes the separation of the jet flow into two distinct streamwise 'tubes' with vorticity of opposite sign, and entraps surrounded crossflow into jet. Similar velocity field structures were obtained via various experimental techniques [6, 8, 12, 14, 39], which have been introduced in the chapter of literature review as well.

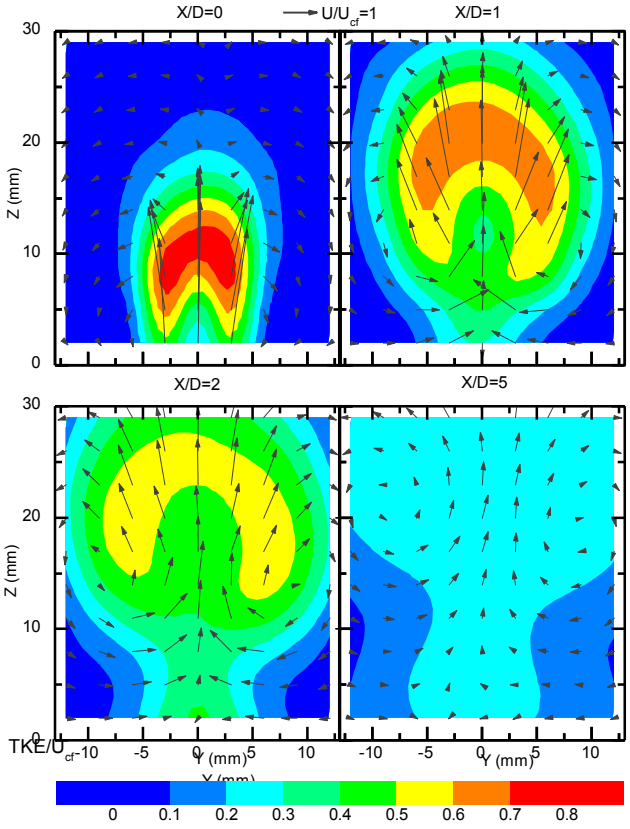

Figure 5.3-1 Mean velocity vectors and TKE field at different cross sections, Jet1N

The near field initiation of this vortex pair is suggested by other experiments and is supposed to arise from the impulse of the jet and the exchange of momentum between the jet and the crossflow, which also favors entrainment. This is augmented by the action of the vortices, which cause large scale mixing within the jet. The vortices acquire axial momentum from the jet and are stronger at higher R. They originate in the near field and are convected far downstream by the crossflow, where they become the dominant feature of the flow, even in this highly confined environment.

The formation process of CVP in the near field of the jet is quite complex and has been studied in depth (detail could be found in Chapter 2). In the present case, the vortex cores appear firstly in the near field of the jet, close to the injection wall, and then spread toward the sidewalls of the duct, but their increasing in diameter and lateral spreading seems to be limited by the confinement effect of the walls.

Although the turbulence kinetic energy is defined from the only two available velocity fluctuation components (see Eq. 5-1), the TKE results at the same location from streamwise measurements and cross-section measurements are general consistent with each other. This means the definition of TKE from only two velocity fluctuation components is accurate enough.

Distribution of turbulent kinetic energy is significantly large at the jet exit plane (shown in Fig. 5.3-1) and extends further in the transverse direction as flowing downstream due to the diffusion as well as the convection, as observed by [92]. They showed that vortical structures at jet exit generate larger turbulent kinetic energy that those of the incoming jet and crossflow. In fact, the maximum turbulence intensity occurs in the near field of the jet, where deformation of jet cylindrical vortex sheet and formation of CVP happen together, which increases complexity and instability of the flowfield greatly. The distribution of turbulence intensity with increasing distance downstream from jet exit reflects the progressive enlargement of the vortical structure and it is expected to improve mixing. More intense turbulence is observed with increasing *R*, in nearly all the cross-sections, in conjunction with a larger penetration of the jet and stronger vortices.

It is recognized that large turbulence kinetic energy could bring benefit for the mixing between crossflow and jet. Thus it can be assumed that strongest entrainment of crossflow into the jet happened in the nearfield of transverse jet, which has been

confirmed in several studies [7]. Further attention should be paid on the asymmetry of jet flow at each cross-section. This issue has been already addressed [12] and it has been suggested that it might be caused by non-perfect alignment of nozzle and crossflow.

Fig. 5.3-2 shows the cross section flowfield development of Jet2N, from X/D=0 to X/D=5. Same as the results at center plane, both the magnitude of velocity and TKE are found larger, when *R* is higher, at least in the nearfield region of the jet. The CVP has been observed for this case as well, in the side corners and moves toward the opposite wall, with increasing diameter. At the cross section where X/D=5, the CVP is well established and become the dominant flow structure there.

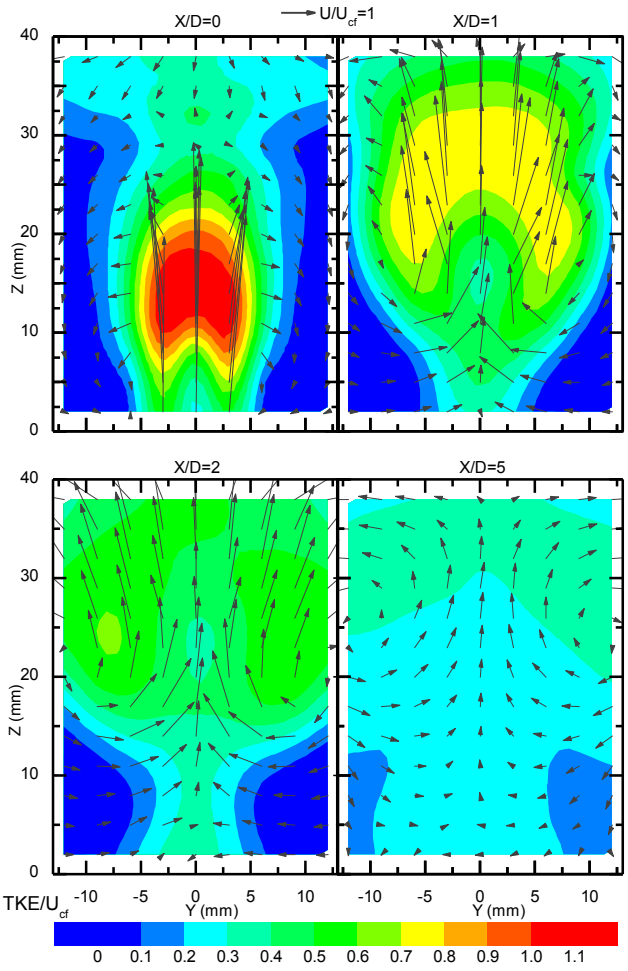

Figure 5.3-2 Mean velocity vectors and TKE field at different cross sections, Jet2N

In addition, at the cross section X/D=0, near the opposite wall, where additional measurements have been performed by turning the probe towards the opposite wall, a backward flow is found there, which can confirm the conjectured spanwise rotating flow due to the interaction among crossflow, jet and duct. Downstream, at the cross section

X/D=1, the flow, particularly in the region around (Y=0 mm, Z=30 mm), is still dominated by the jet penetration. Confinement from the duct to the jet development is evident near the opposite wall, where the jet velocity is rapidly reduced, and the flow is squeezed and forced to move laterally. Then as the CVP continues to enlarge, it impinges on the opposite wall, and slows down its transverse movement, as indicated by the mean velocity field at cross sections X/D=2 and X/D=5. Finally, this CVP becomes the dominant flow structure, as mentioned before.

The maximum turbulence kinetic energy occurs in the near field, around the region where the jet is being deflected by the crossflow, consistently with results of same tests in the center plane. As the CVP becomes the dominant flow structure, the turbulence kinetic energy decreases rapidly, and the flow tends to become more uniform, suggesting positive effect to the jet-crossflow mixing brought by the CVP. From the cross section X/D=5, the transverse positions of cores of the CVP do not change apparently, caused by the confinement from the duct obviously.

5.3.2 Jet with Streamwise Injection and Counter-streamwise Injection

Fig. 5.3-3 presents the mean velocity and TKE for the case of streamwise injection (Jet2S), at cross sections X/D=1 and X/D=5. It can be observed that at the cross section X/D=1, mixing between jet and crossflow is quite low, compared with the case of normal injection. The crossflow is nearly unaffected by the jet, except in the region around the jet exit. Particularly, the TKE in most of the cross section is comparable with that of crossflow without jet injection, which is below 10%. Crossflow is entrained into the wake region, because of the pressure gradient there. The existence of CVP is not clear, although there are two rotating flows at the lateral side of the jet. This confirms the previous analysis that the decreasing strength of shear layer vortices influences the formation of CVP, and thus results in poor mixing at this cross section.

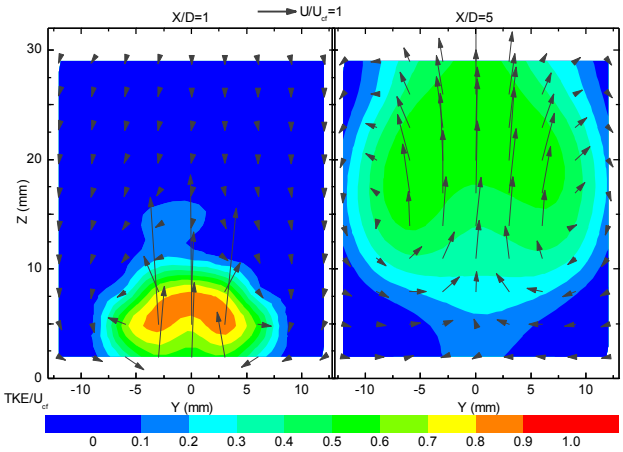

Figure 5.3-3 Mean velocity vectors and TKE field at different cross sections, Jet2S

Downstream at X/D=5, it could be still observed some area with low TKE, indicating lower interaction between jet and crossflow there. The CVP is more evident at this cross section, acting to involve crossflow into the jet. However, the general TKE in the test region at this cross section is higher than the corresponding case with normal injection, and seems less uniform, suggesting poor mixing under this condition.

The cross-section flowfield development of counter streamwise injection of jet (Jet2CS) is shown in Fig. 5.3-4. Again, the flow is greatly different from those of normal injection or streamwise injection. The jet is firstly found to interact with crossflow upstream, at the cross section X/D = -4. The crossflow suppresses the counter stream penetration of the jet, and forces it to scatter around. Then the penetration of the jet becomes dominant at cross section X/D= -2, due to its high momentum flux compared to the crossflow. The jet seems to behave as a cylinder obstacle there, blocking the streamwise movement of the crossflow. Consequently, the crossflow could only circumvent the jet, passing it through the lateral sides. However, the maximum TKE is found in this cross section, indicating a strong interaction between jet and crossflow here, which is consistent with the result in the center plane (Fig. 5.2-4). We can infer that there might be significant entrainment of crossflow into the jet, due to the strong interaction between the jet and the crossflow.

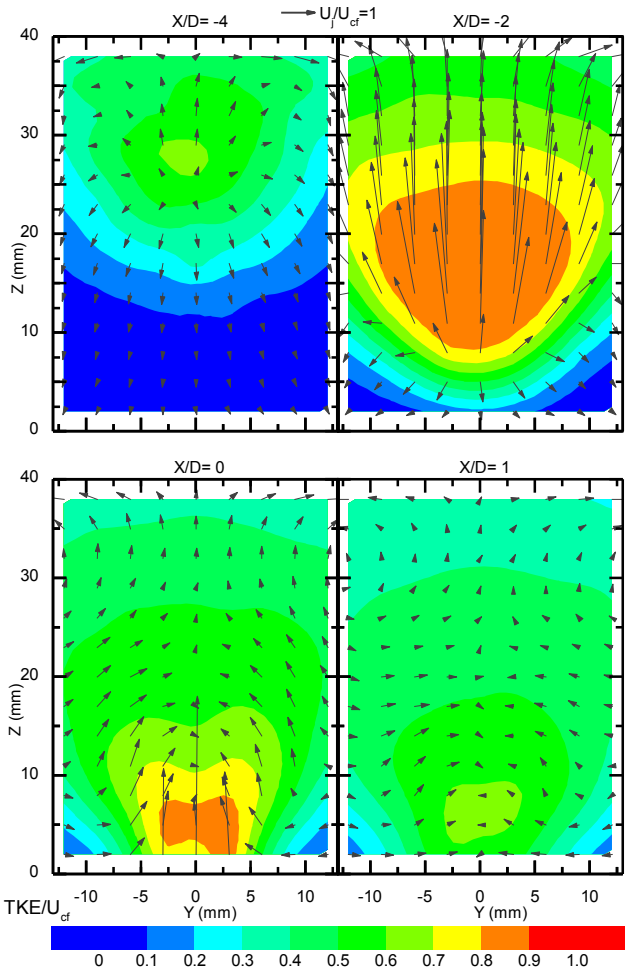

Figure 5.3-4 Mean velocity vectors and TKE field at different cross sections, Jet2CS

At the injection cross section, X/D=0, the bypassed crossflow is firstly brought up by the jet, tending to occupy the 'empty' region close to the jet leeside. The crossflow parts from the two sides of jet meet rejoins beyond the jet, then continue moving upward and finally form a CVP, similar to what observed when the jet is normally injected. Large TKE could be also found here, where the crossflow interacts with the jet, consistently with the results in the TKE map at center plane. Then the flow tends to become uniform quickly. The magnitude of both the spanwise and transverse velocity (U_y and U_z) decreases greatly at the cross section X/D=1 compared with upstream. In addition, at this cross section the distribution of TKE under this condition is much more uniform than other cases in this study. From the cross section flow development, it could be deduced that reverse injection could enhance the mixing between the jet and the crossflow.

5.3.3 Mean Velocity and TKE Field at Far Field

Fig. 5.3-5 shows the mean velocity and TKE distribution at far field, cross section X/D=10, for all the four cases concerned so far in this chapter. Notice the change of color scale. For the cases with normal injection (Jet1N and Jet2N), the CVP is quite clear observed, which is shown at the top two sub-maps. This confirms the previous statement that the CVP could persist until far field. Notice that the transverse distance between the CVP and injection plane is longer for the case of Jet1N, where jet-to-crossflow momentum flux ratio is smaller. This infers the confinement effect from the opposite wall, which might also cause longer spanwise distance between the two vortex pair.

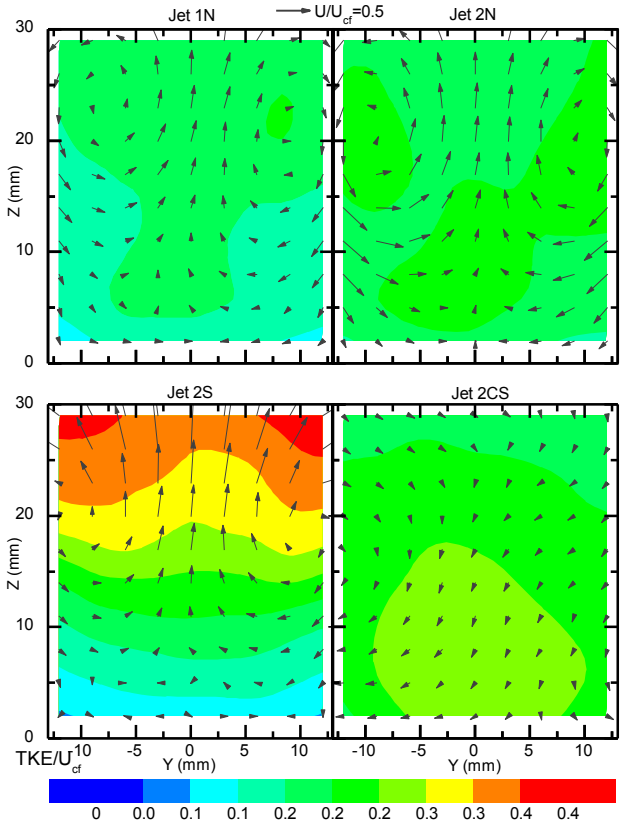

Figure 5.3-5 Mean Velocity and TKE distribution at cross section X/D=10, for different cases: Jet1N (topleft), Jet2N (topright), Jet2S(bottomleft), Jet2CS (bottomright)

The TKE level of both Jet1N and Jet2N is reduced greatly at this cross section, although it is still not homogeneous. Relative large TKE is observed at the core of CVP, as well as region between center of duct and injection plane, where crossflow is brought up by the crossflow and entrained into it. The TKE level of Jet2N is generally higher than that of Jet1N, which might be caused by the confinement of opposite wall or by the larger jet

Reynolds number. Again, it is generally believed large TKE might enhance the mixing. Thus it can conclude that the confinement of duct wall can bring a positive effect on the mixing between jet and crossflow.

The great influence of injection orientation on the velocity field can be also observed clearly at this far field, which is shown at two sub-maps at the bottom of Fig.5.3-5. When jet is injected streamwise, indication of a CVP can be found at this cross section, although not fully observed due to the limited test area. Consider the CVP is not clearly observed at upstream (see Fig. 5.3-3), it is hard to conclude whether this CVP is formed by the interaction between jet and crossflow, or caused by the confinement of duct wall. Despite the existence of CVP at this cross section, the TKE is still less uniform than the case where jet is normally injected, indicating a poor mixing between jet and crossflow even at this downstream.

When the jet is injected against the cross flow, the magnitude of cross section components of velocity is decreased greatly at this cross section, and CVP could not be observed at least in the test area. This infers the jet and crossflow are well mixed at this downstream field, at least in the test area. However, the TKE level is slightly higher than that of Jet2N. In addition, the TKE map of Jet2CS shows a negative gradient from injection plane to duct wall.

In order to compare the influence of injection angle on the mixing between the jet and the crossflow in the far field, the TKE distribution at cross section X/D=10 has been analyzed by statistical methods. Fig. 5.3-5 shows the average and standard deviation of TKE values measured in the entire cross section. Both the average turbulence kinetic energy and its standard deviation present the same trend: the case with normal injection has the smallest average turbulence kinetic energy as well as its standard deviation, while the case with streamwise injection shows the largest value of those two parameters. It can be argued that the jet with streamwise injection is the least affected by the crossflow and confinement of the duct. The relative small difference between normal injection and reverse injection needs to be further studied.

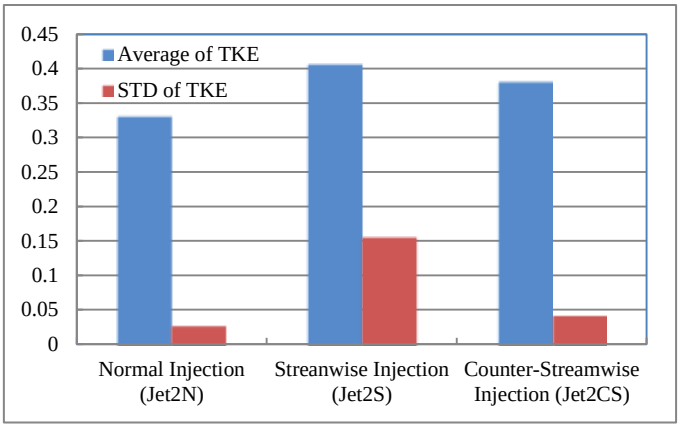

Figure 5.3-6 Comparison of TKE at cross section X/D=10

5.4 Effect of Injected Gas Composition

The effect of different gases injected normally into crossflow is shown in Fig. 5.4-1, where the mean and RMS velocity components are compared. For the case Jet2M, where the mixture gas was injected instead of air, jet exit mean velocity was corrected to obtain the same jet-to-crossflow momentum flux ratio of the Jet2N case, which is indicated in Table 5.1.

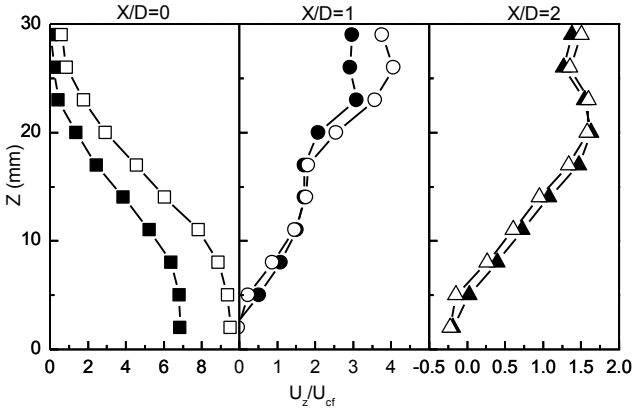

solid symbol: air jet (Jet2N), empty symbol: mixture jet (Jet2M); Y=0

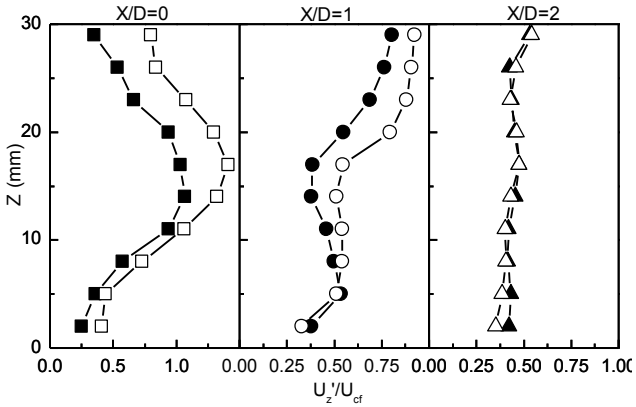

solid symbol: air jet (Jet2N), empty symbol: mixture jet (Jet2M); Y=0

Figure 5.4-1 Comparison of mean transverse velocity U_z (above) and RMS U_z' (below) between air jet and mixture jet (Jet2N and Jet2M)

Fig. 5.4-1 shows that for both profiles of transverse mean velocity and their RMS, these two jets with two different gases exhibit the same trend. There is a considerable difference only in the near field, at X/D=0, which is induced by the different jet exit velocity. This confirms again that the dominant parameter is *R*, regardless of which gas is injected.

CHAPTER 6

HWA MEASUREMENTS

Spectral analysis of velocity fluctuations is a powerful tool to study turbulent flows. Turbulent energy spectra are the decomposition of the measured function into waves of different periods or wavelengths; thus the value of the spectrum at a given frequency (or wavenumber) represents the mean energy in that wave. Spectra can be used to study how waves, or eddies, of different sizes exchange energy with each other and how they dissipate energy. In the following, the evaluation of turbulent energy spectra is performed, based on the results of HWA measurement, to study flow field instabilities and effects of injection orientation of jet. The measurements have been performed at the outlet of duct, which is 170 mm downstream of jet outlet center in the case of normal injection and streamwise injection, and 130 mm downstream for the case of counter streamwise injection.

During the HWA measurement, only the results of one jet-to-crossflow momentum flux ratio will be presented, which is 3.05. And the crossflow velocity is kept as 2.55 m/s. In addition, only jet of air is considered. Similar nomenclature is used to define the name of test conditions as previous chapter: Jet N refers jet normally injected; Jet S refers jet injected streamwise; and Jet CS refers jet injected counter streamwise with the crossflow.

6.1 Turbulence Intensity at Outlet of the Duct

The turbulence intensity could be deduced from the fluctuation of HWA signals, which is defined as follows:

$$I = \frac{\sqrt{\overline{u'^2}}}{U} \qquad \text{(Eq. 6-1)}$$

Where U is the mean flow velocity and $\overline{u'}$ is RMS of measured flow velocity. Since the velocity is proportional to HWA signal (see Section 3.4), the turbulence intensity could be calculated as follows:

$$I = \frac{\sqrt{\overline{s'^2}}}{S} \qquad \text{(Eq. 6-2)}$$

Where S is the mean signal intensity and $\overline{s'}$ is the RMS of HWA signal. The results of same transverse jet injected with three different orientations are shown in Fig. 6.1-1.

Generally speaking, the results measured by HWA at the outlet cross section of duct are consistent with those measured by LDV at 10 D downstream of center of jet nozzle, which are presented in Section 5.3.3, even though the velocity of both the jet and the crossflow are different with each other. When jet is normally injected, it presents the lowest global turbulence intensity among the three cases. The turbulence intensity level at the corner of duct is slightly higher than that of center, inferring the effect of duct wall at this downstream.

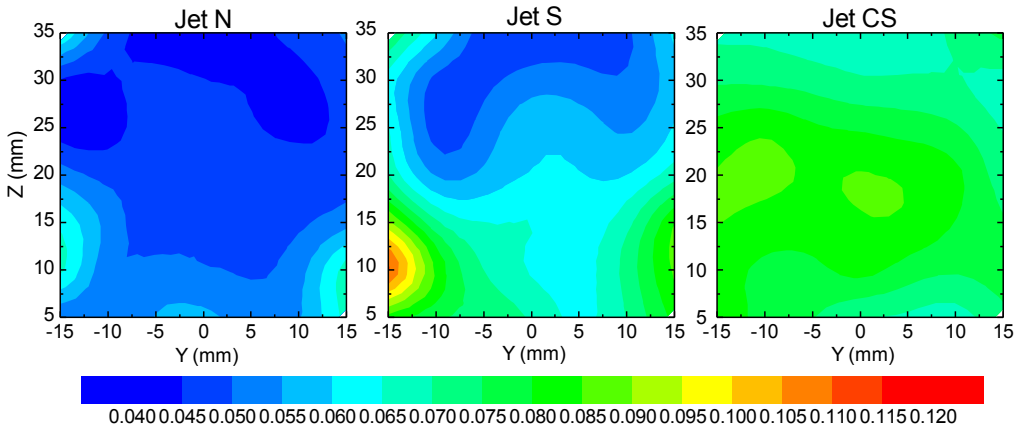

Figure 6.1-1 Turbulence intensity at outlet cross section of duct, for transverse jets with three different injection orientation, R=3.05, U_{cf}=2.55m/s

In the case of streamwise injection, the turbulence intensity level is the least uniform among the three cases, and turbulence intensity greater than 10% is measured only in this case, at bottom corner from the view of Fig. 6.1-1. The turbulence level is relative low near the opposite wall (up in the figure), and high near the injection plane (bottom in the figure). The low turbulence area presents a kidney shape, similar with the shape of CVP.

All of these phenomena confirm the poor mixing between jet and crossflow when jet is streamwise injected, even at this far downstream distance. Near the opposite wall, due to the interaction among the jet, the crossflow and the duct wall, mixing is enhanced and almost completed at the outlet cross section, thus there shows relative low turbulence intensity. Contrarily, the high turbulence intensity at other locations indicates that the interaction or mixing is still carrying on even at the outlet cross section, which is 170 mm (more than 25D) downstream of jet nozzle center.

For the jet counter streamwise injected into the crossflow, the turbulence intensity distribution at outlet cross section is more uniform than other two cases. However, the level of turbulence intensity is generally higher than the case when jet is normally injected, which is consist with previous observation by LDV TKE results. It could be concluded that counter streamwise injection would increase the turbulence intensity of flow field.

In addition, the turbulence intensity is slightly higher in the center of outlet cross section, for the case of counter streamwise injection, which is opposite with the case of normal injection.

6.2 Spectral Energy

Spectral energy of fluid velocity and autocorrelation curves of velocity fluctuations could be calculated from intermittent HWA signal. The turbulence energy spectra in the frequency domain for three cases concerned in this chapter are shown in Fig. 6.2-1, which is calculated by Fourier transformation from the HWA signal measured at the center of outlet cross section (x=170 mm, y=0 mm, z=20 mm). Here the data have been filtered by a 20 – points moving average.

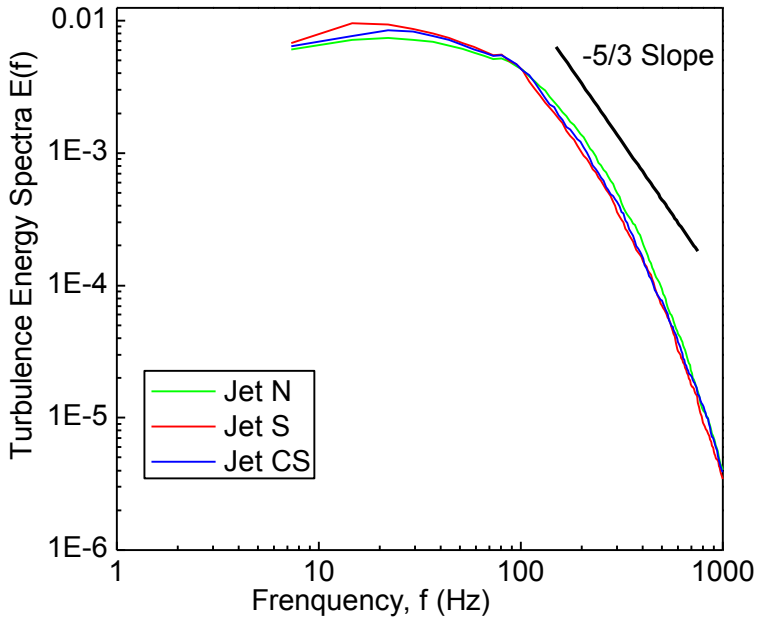

Figure 6.2-1 Turbulence energy spectra for three cases concerned in this chapter, calculated by Fourier transformation from the HWA signal measured at the center of outlet cross section (x=170mm, y=0mm, z=20mm). (Data have been filtered by a 20 – points moving average).

Generally speaking, all of the three turbulence energy spectra curves are very close to each other. Unlike those measurements at the nearfield (see Section 2.2.2), no characteristics frequency could be observed here. However, there is a clearly defined inertial subrange (150 Hz~70 0Hz) where the slope of the spectra is -5/3, for all of the three cases.

Despite the similarities of the turbulence spectra energy curves for these three cases, there are still slight differences among them. Basically, the spectra could be divided into two subranges, at the frequency 100 Hz. When the frequency is lower than 100 Hz, the turbulence energy of Jet S is slightly larger than other two cases and that of Jet N is the lowest one. Contrarily, later when the frequency is greater than 100 Hz, the turbulence energy of Jet N is slighter the largest one and that of Jet S is slighter lower than other two cases. This means turbulence energy of Jet S at this measurement point is more distributed in low frequency domain, while that of Jet N is slightly more distributed in high frequency domain. This infers mixing is more completed for the case of Jet N.

The turbulence energy spectra at other points generally present the same trend, although they are not shown here.

6.3 Eulerian Time Scale

The Eulerian integral time scale (T_E) is a measurement of the most rapid changes that occur in the fluctuations, thus it could be used to characterize the turbulence and consequently the mixing level in this study. This time scale could be calculated from the turbulence energy spectra obtained from Fourier analysis of HWA signal, as follows:

$$\frac{1}{T_E^2} = 2\pi^2 \int_0^\infty E(f) \cdot f^2 \, df \qquad \text{(Eq. 6-3)}$$

Fig. 6.3-1 shows the comparison of Eulerian integral time scale at outlet cross section of duct, for the three injection orientations considered in this section. The distribution of this time scale is even more complex than that of turbulence intensity, which is shown in Fig. 6.2-1.

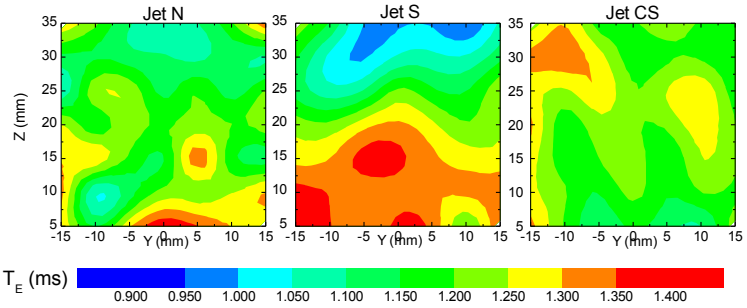

Figure 6.3-1 Eulerian integral time scale at outlet cross section of duct, for transverse jets with three different injection orientation, R=3.05, U_{cf}=2.55m/s

As shown in Fig.6.3-1, the distribution of Eulerian integral time scale at the outlet cross section of the duct is more complex than that of turbulence intensity. Nonetheless, the Eulerian integral time scale of the cases of Jet S and Jet CS is more uniform than that of case Jet S, which is consistent with the results of the turbulence intensity distribution at the same place. In addition, same as the turbulence intensity distribution, the Eulerian integral time scale is larger at the bottom than that near the opposite wall, for the case Jet S. This infers the different mixing stage for those three cases. The global mixing level of Jet S is behind of that of Jet N and Jet CS.

To conclude, the results from HWA measurements and data processing confirms previous analysis on the flow field caused by gas injection into the confined crossflow based on the observation from schlieren imaging and LDV experiments. Except those

differences in the turbulence intensity and Eulerian time scale, no obvious influence caused by various injection conditions on the spectral energy curves was found at the outlet of the duct.

CHAPTER 7

NUMERICAL SIMULATION

Numerical methods have been used to study the jet into confined crossflow as well as experimental methods, tying to reveal some more flow properties in the flow field, which is difficult to be measured by experimental methods, such as the concentration of jet gas at various locations in the flow field, when different gases instead of air is injected. This chapter will present the numerical simulation part of this study in detail.

7.1 Simulation Details

Fig. 7.1-1 shows a schematic of the computational domain, where the jet issues perpendicularly from a round pipe into the crossflow. Same as the experimental study, the crossflow is confined in a square duct, which is defined as solid walls. This simulated square duct has the same cross section with that used to perform experiments, which is 40 mm by 40 mm. The length of the simulated duct is reduced to 200 mm, aiming to save the calculation time. In the case of normal injection and streamwise injection, the center of the nozzle is 30 mm downstream of the crossflow inlet, while for the case of counter streamwise injection, the center of the nozzle is 70 mm downstream of the crossflow inlet. The nozzle has a length of 20 mm, and a diameter of 6.4 mm, which is close to that used in most of the experimental studies, and expected to allow the full development of the jet.

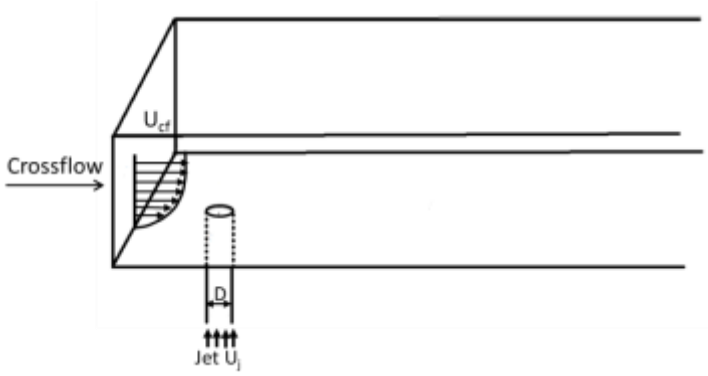

Figure 7.1-1 Schematic of simulation domain

Same coordination system has been used in this simulation domain: the crossflow is in the x-direction and the jet is in the z-direction when it's normally injected with the crossflow. The origin is located at the center of the jet exit. The crossflow velocity (U_{cf}) is adapted from LDV measurement directly, while the jet velocity (U_j) is set constant at the nozzle inlet, which is calculated from the volume flow rate measured by experiments. Consequently, the crossflow has a boundary layer thickness of 7 mm, same as that measured by experiments. The detail of the boundary conditions will be given later.

The simulations are performed at only one jet-to-crossflow momentum flux ratio: R=6.1, which are representative ratio when the confinement effect from the wall is relative strong. Jets of three different gases have been considered: air, CO_2 and CH_4. Air jet is used to compare the calculated velocity and that measured by LDV experiments. CO_2 is used to compare the calculated trajectory with that measured from schlieren imaging experiments, where CO_2 is injected mainly. Finally, CH_4 is studied as well to simulate the situation of the practical application of transverse jet of CH_4 on port fuel injection internal combustion engines.

Same as the experimental studies, three different injection orientations have been considered in the numerical study, namely normal injection, streamwise injection and counter streamwise injection. Table 7.1-1 describes the different simulations performed. The parameters include jet-to-crossflow momentum flux ratio R, injection gas, and jet exit velocity as well as injection orientation. As shown in Table 7.1-1, when different gas is injected, jet exit velocity is changed to maintain the save jet-to-crossflow momentum flux ratio.

Table 7.1-1 Conditions for the various simulations performed

Case	R	Injection Gas	Jet Exit Velocity (m/s)	Injection Orientation
Jet AN	6.1	Air	10.36	Normal
Jet AS	6.1	Air	10.36	Streamwise
Jet ACS	6.1	Air	10.36	Counter Streamwise
Jet CN	6.1	CO_2	8.41	Normal
Jet CS	6.1	CO_2	8.41	Streamwise
Jet CCS	6.1	CO_2	8.41	Counter Streamwise
Jet MN	6.1	CH_4	13.94	Normal
Jet MS	6.1	CH_4	13.94	Streamwise
Jet MCS	6.1	CH_4	13.94	Counter Streamwise

Similar rules to define the case name as that used in chapter 5 are applied here. In the case names appearing in Table 7.1, the alphabet A, C, M indicate injected gas of Air, Carbondioxide (CO_2), Methane (CH_4) respectively, while N, S, CS refer the injection orientation of Normal, Streamwise and Counter Streamwise respectively.

7.2 Numerical Details

The simulation is performed with FLUENT. The numerical scheme solves the compressible Navier-Stokes equations, neglecting the effect of gravity or any body force:

$$\frac{\partial \rho}{\partial t} + \frac{\partial \rho u_i}{\partial x_i} = 0 \qquad \text{(Eq. 7-1)}$$

$$\frac{\partial \rho u_i}{\partial t} + \frac{\partial \rho u_i u_j}{\partial x_j} = -\frac{\partial p}{\partial x_i} + \mu \frac{\partial^2 u_i}{\partial x_j x_j} \qquad \text{(Eq. 7-2)}$$

Here u_i, p and μ denote the velocities, pressure and viscosity respectively. An additional diffusion equation has been added when CO_2 or CH_4 is used as injection gas:

$$\frac{\partial \rho Y_k}{\partial t} + \frac{\partial u_i Y_k}{\partial x_i} = -\frac{\partial J_{k,i}}{\partial x_i} \qquad \text{(Eq. 7-3)}$$

Where Y_i is the local mass fraction of each specie k, and J_k is the diffusion flux of specie k, which arises due to gradient of concentration and temperature. In this simulation, this mass diffusion due to concentration gradients is modeled by dilute approximation (also called Fick's law):

$$\overrightarrow{J_k} = -\rho D_{k,m} \nabla Y_k - D_{T,k} \frac{\nabla T}{T} \qquad \text{(Eq. 7-4)}$$

Here T is the local temperature, $D_{k,m}$ is the mass diffusion coefficient for specie k in the mixture, and $D_{T,I}$ is the thermal diffusion coefficient. Notice that in this species transport model, there is no production term or source term, since there is no reaction.

Reynolds-averaged approach is used to model the turbulence. Specifically, a 'reliable k-ε' model is applied, which is a relatively recent development and differs from the standard k-ε model. The detail of this model is beyond the scope of this thesis and can be found in [93]

A pressure based solver has been selected to solve the above governing equations. This pressure-based solver employs an algorithm which belongs to a general class of methods called the projection method [94]. In the projection method, wherein the constraint of mass conservation (continuity) of the velocity field is achieved by solving a pressure (or pressure correction) equation. The pressure equation is derived from the continuity and the momentum equations in such a way that the velocity field, corrected by the pressure, satisfies the continuity. Since the governing equations are nonlinear and coupled to one another, the solution process involves iterations wherein the entire set of governing equations is solved repeatedly until the solution converges. A coupled algorithm was used to solve a coupled system of equations comprising the momentum equations and the pressure-based continuity equation. Because of the momentum and continuity equations are solved in a closely coupled manner, the rate of solution convergence significantly improves, with just a cost of memory increasing by 1.5 - 2 times that of the segregated algorithm (i.e. SIMPLE, SIMPLEC and PISO).

Although the flow is steady in this study, a transient solver was used here because it can improve the solution accuracy.

The computational mesh is unstructured and mainly consists of tetrahedral elements. The use of an unstructured mesh allows an efficient variation of the mesh size. The mesh size varies from 0.2 mm (jet pipe wall) to 2 mm. Fig. 7.2-1 shows part of the cross section of the mesh on the center plane for all the three cases considered in this study. Notice the dense area in the jet pipe, the inlet of the duct and the outlet of the duct. The total number of those elements is around 0.9 million for all of the three cases.

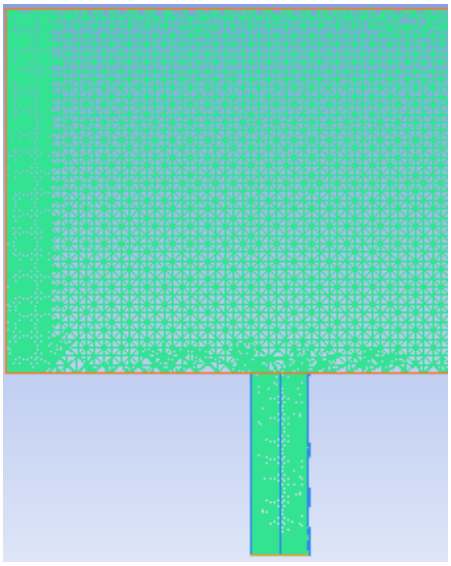

(a) case normal injection

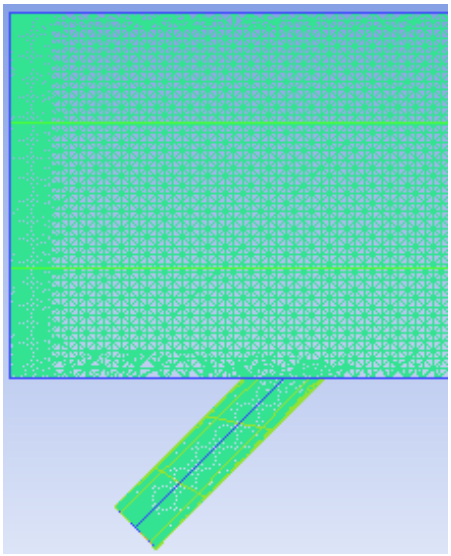

(b) case streamwise injection

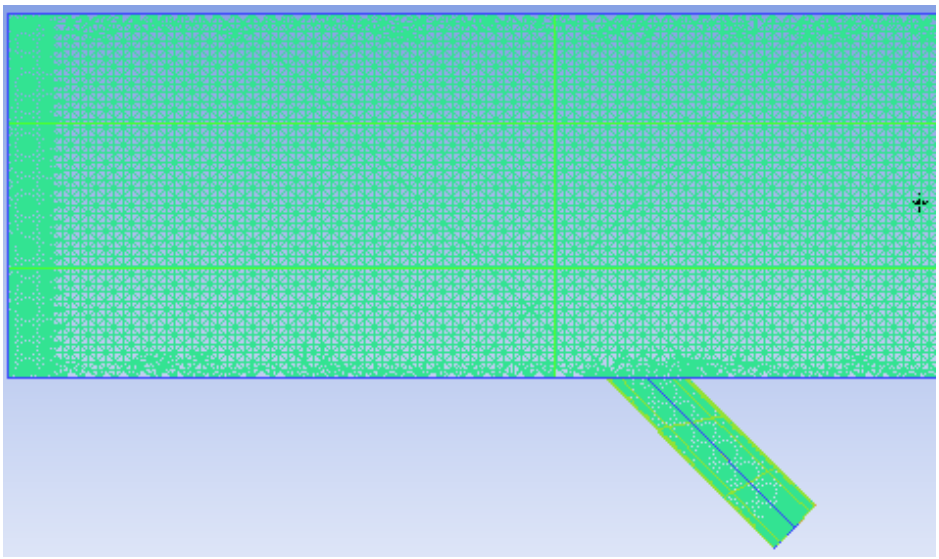

(c) case counter-streamwise injection

Figure 7.2-1 The computational mesh on the center plane for all the three cases considered in this study. Note the dense area in the jet pipe, the inlet of the duct and the outlet of the duct

The boundary conditions are specified as follows in detail. At the crossflow inlet plane, the velocities and turbulence intensity are adapted directly from the LDV measurement, which is shown in (LDV results of crossflow without injection plot). Thus the boundary layer thickness in the simulation is same as that of real case during experimental tests. The injection plane of the jet is set as mass flow inlet, since the specified velocity data from experimental measurement is not available at this small cross section. Nonetheless, the set mass flow rate is equal with that of corresponding measurements. Although the velocity is uniform at the entrance of injection pipe, which is different from the experiment set up, the velocity at the outlet of injection pipe, interfacing with the crossflow, presents a top hat profile. This is because that the enough long distance of injection pipe in the simulation allows full development of injection flow before it arrives the outlet. The outlet of the duct is set as ambient. Finally, the standard wall functions are used to specify the walls of both the duct and the injection pipe, which is based on the work of [95].

The computations are initialized with just the crossflow. As mentioned previously, a transient solver was used here. The computational time step is of the order of 1/3 D/U_{cf} (1ms), and the solution is advanced to about 0.5 second for the case of normal injection and streamwise injection and 1 second for the case of counter streamwise injection, which

is enough to allow the initial transients to exist the domain. The time-averaged quantities presented in this paper are computed after the transients exit the domain.

7.3 Calculation Results

7.3.1 Model Validation

The simulation has been firstly validated by comparing the results from the simulation to that measured from LDV experiments. Fig.7.3-1 shows the comparison of jet axis velocity between LDV measurements and simulation, case of Jet AN (recall the case name indicated in Table 7.1-1). The two jet axis velocity profiles corresponding with simulation and LDV measurements respectively show well agreement with each other. The slight difference between them could be caused either by the relative rough computational grid or by the inaccuracy of experimental measurements (i.e. inaccuracy of locating of probe volume in LDV measurements)

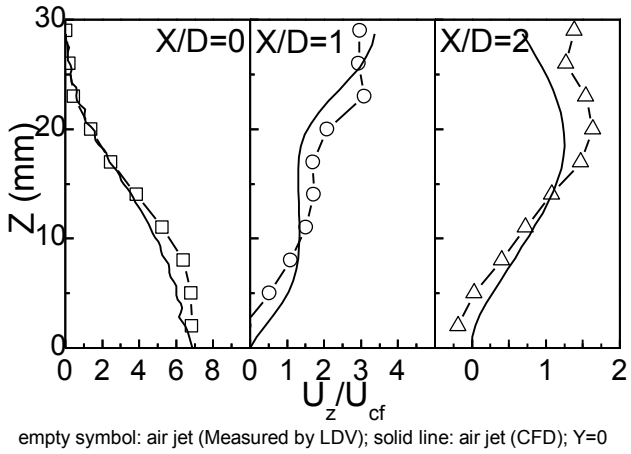

Figure 7.3-1 Comparison of jet axis velocity between LDV measurements and simulation, case Jet AN

The comparison of RMS of jet axis velocity between LDV measurements and simulation is shown in Fig. 7.3-2, with the same case as above. The difference between the results from simulation and LDV measurements is larger than that of velocity profiles, particular in the region near from the injection wall. Several factors could cause these differences. First of all, the grid density near from the injection wall, particular the region near from the outlet of injection pipe needs to be refined. However, this is limited by the

performance of the PC used in this study, thus haven't been conducted. Then the selection of turbulence model and wall function might also cause this difference. Nonetheless, this difference is still acceptable for the next studies.

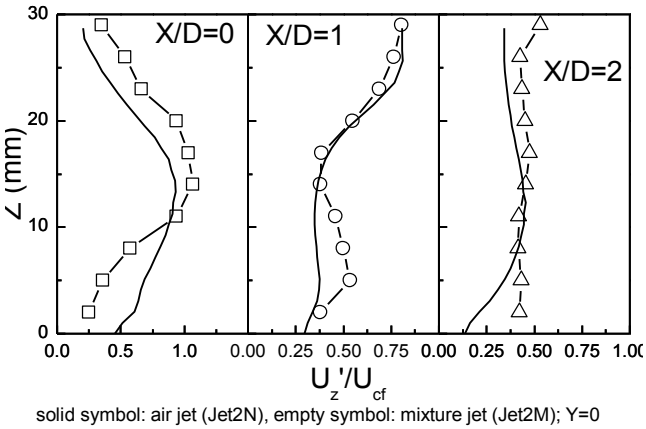

Figure 7.3-2 Comparison of RMS of jet axis velocity between LDV measurements and simulation, case Jet AN

7.3.2 Mass Fraction Distribution of Injection Gas

The mass fraction distribution of injection gas could be calculated based on this simulation model, which is difficult measured directly by experimental techniques. However, the mass fraction distribution of injection gas can reflect the mixing between the crossflow and injection jet explicitly. Thus this part is essential to fully describe the flow field.

Fig. 7.3-3 shows the mass fraction of CO_2 in the center plane for the case Jet CN. The mass fraction of injected gas is illustrated by the color contour in the plot, same as the rest part of this chapter. Recall the schlieren image for the same condition, which is shown in Fig.7.3-4, the jet trajectory resulted from calculation matches with that from schlieren image very well.

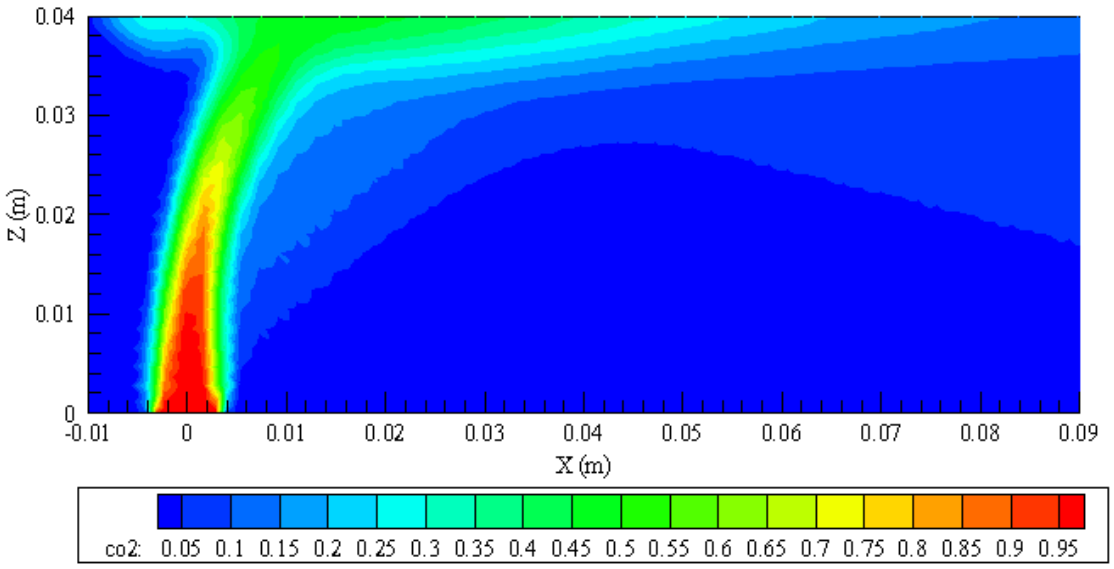

Figure 7.3-3 Mass fraction of CO_2 in the center plane, case Jet CN

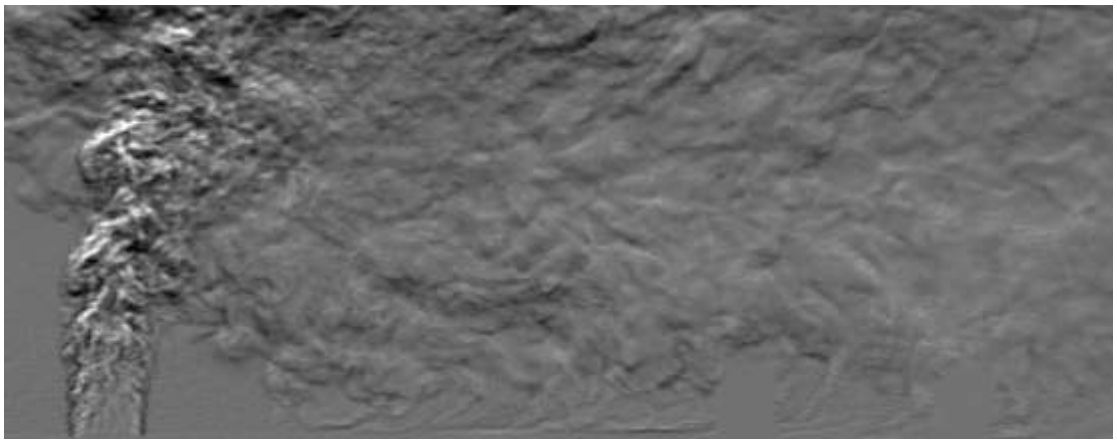

Figure 7.3-4 Instantaneous schlieren image, case Jet CN

It could be observed in both of Fig.7.3.3 and Fig.7.3.4 that large portion of CO_2 exists in the region where the jet impact on the opposite wall, which is consistence with the found in LDV observation that there exists a rotating structure, resulted from the interaction among the jet, the crossflow and the opposite wall.

In addition, in this center plane, most of the CO_2 are found near the opposite wall, while there is a large area behind the jet (could be called 'wake' region') where the mass fraction of CO_2 is lower than 5%. This means the mixing between the jet gas and the crossflow is very low here and most of CO_2 moves to the opposite wall and might come to two sides instead of coming down, and this could be confirmed by the velocity results from LDV measurement (see Chapter 5)

The calculated mass fraction of CH_4 for the case of Jet MN is shown in Fig. 7.3-5. It could be seen that in the nearfield, the jet structure is almost identical as that for the case of Jet CN (shown in Fig 7.3-5). This confirms again that in the near field the jet-to-crossflow momentum flux ratio is the dominant parameter for the development of flow field.

Nonetheless, slight difference between the mass fraction distribution of CO_2 and CH_4 for the case of Jet CN and Jet MN respectively could be found at downstream, in the 'wake region'. There the mixing between air and CH_4 appears slower than that between air and CO_2. The reason behind this observation is unclear and needs to be study further.

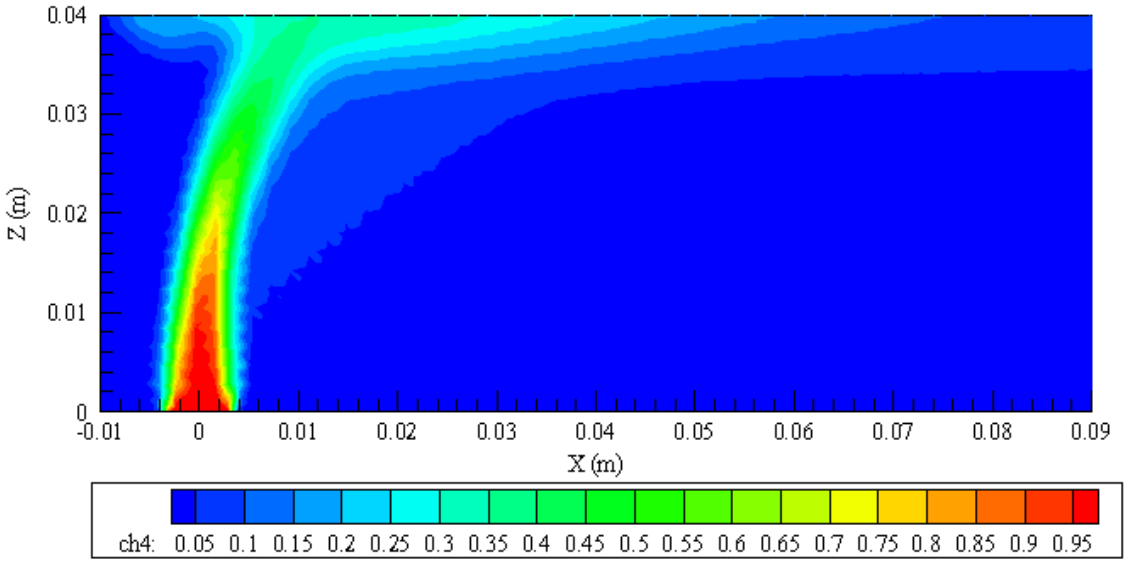

Figure 7.3-5 Mass fraction of CH_4 in the center plane, case Jet MN

Fig.7.3-6 presents the calculated mass fraction of CH_4 at different cross sections along the direction of crossflow, for the case of Jet MN. Here the development of flow field is more intuitively illustrated, compared with previous LDV results. In addition, the view is expanded to full cross section of the duct, larger than that in the LDV results.

First of all, at the injection plane, the flow is dominated by the jet penetration. Large amount of crossflow has entered the jet to dilute the jet quickly. Near the opposite wall, a layer of CH_4 can be observed, indicate the backward movement of jet gas after it impacts on the opposite wall. This is the result of the rotating flow caused by the interaction among the jet, the crossflow and the opposite wall, which has been mentioned previously. Then downstream, at the cross section X/D=1, a thin kidney shape of CH_4 mass fraction distribution can be found in the center of the duct. The hollow area between the two horns

of this kidney is a result of the upward involvement of the crossflow nearby by the counter rotated vortex pair, which is clearly shown in previous LDV measurement results. Some CH_4 distribution can be seen in the corner of the opposite wall, confirming the lateral movement of the jet caused by the confinement of the opposite wall, which has been observed by LDV measurements as well.

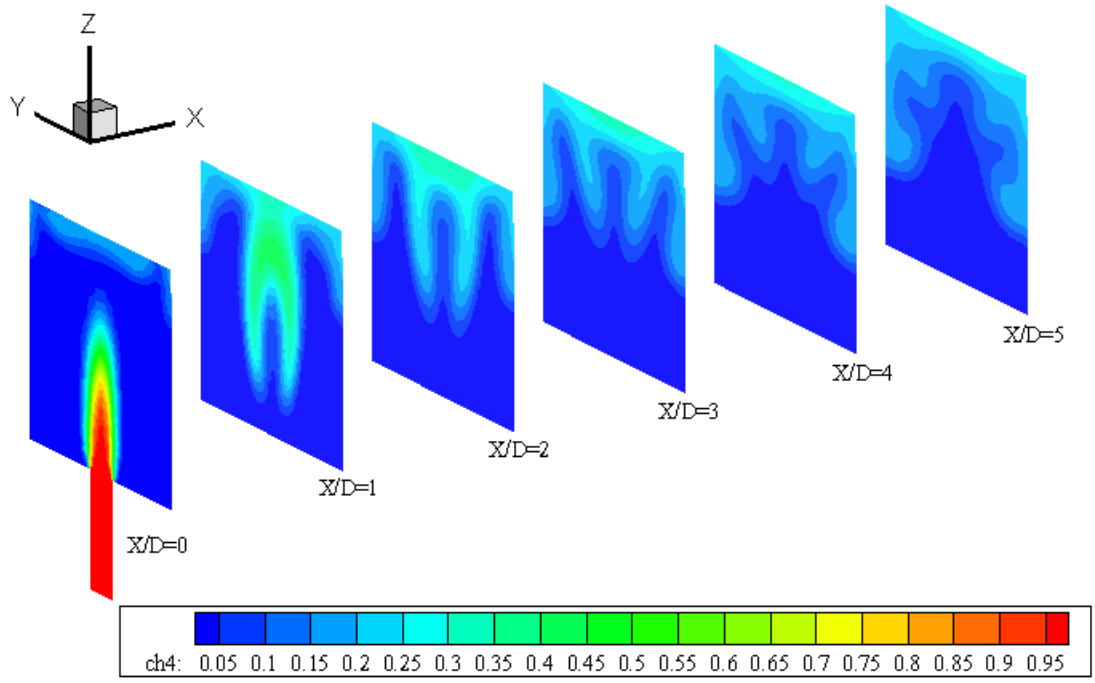

Figure 7.3-6 Mass fraction of CH_4 at different cross sections along the direction of crossflow, case Jet MN

Then more downstream, most of the jet gas seems stay at the upper part of the duct. The CVP continues to involve air from cross flow and dilute the jet. The opposite wall also plays a positive role in the mixing process between the jet and the crossflow, since it stops the penetration of the jet, and then provides more possibility for the CVP to involve the crossflow into the jet and dilute the jet. The shape of the jet is keeping change, which is apparently the result of the confinement from the duct walls.

The calculated mass fraction of CH_4 at different cross sections along the direction of crossflow for the case of Jet MS is shown in Fig. 7.3-7. Again, the mixing between the jet and the crossflow is much slower than that of case Jet MN. Unlike the case of Jet MN, in the case of Jet MS it seems that the jet round shape is not changed by the cross flow, and most of the mixing between the jet and the crossflow happens around the jet 'cylinder', as a result of concentration gradient, which is more similar with that of free jet.

In addition, there is a band-liked structure below the main jet 'streamwise inclined cylinder' structure, which is not seen in the case of Jet MN. This is either not observed in the instantaneous schlieren image captured under the same flow conditions. The boundary layer of the crossflow could contribute for this band structure. However, the forming process of this structure needs to be studied further.

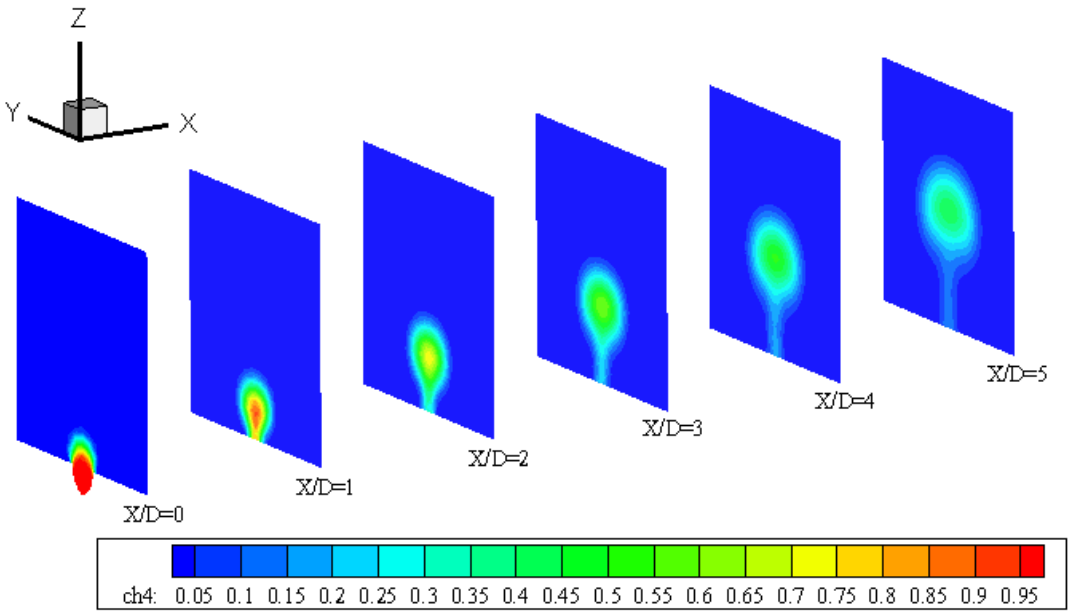

Figure 7.3-7 Mass fraction of CH_4 at different cross sections along the direction of crossflow, case Jet MS

In the case of counter streamwise injection, strong mixing between the jet and the crossflow can be observed upstream of the exit of jet, which is shown in Fig. 7.3-8. There the jet is deflected by the crossflow, and strong interaction between the jet and the crossflow happens, enhances the mixing between the jet and the crossflow. This has been observed during LDV measurements as well.

Downstream of the jet nozzle, a concentration gradient can be found. As further from the injection wall, the mass fraction of CH_4 is larger. This is a combined result from jet penetration and opposite wall confinement. In addition, the flow field become less and less symmetric after the cross section X/D= -1. This asymmetric flow field could be also observed in the case of Jet MN. The asymmetric flow has been also observed in both the LDV and HWA measurements, mentioned in Chapter 5 and Chapter 6. The mechanism behind this asymmetric is complex and hasn't been well understood.

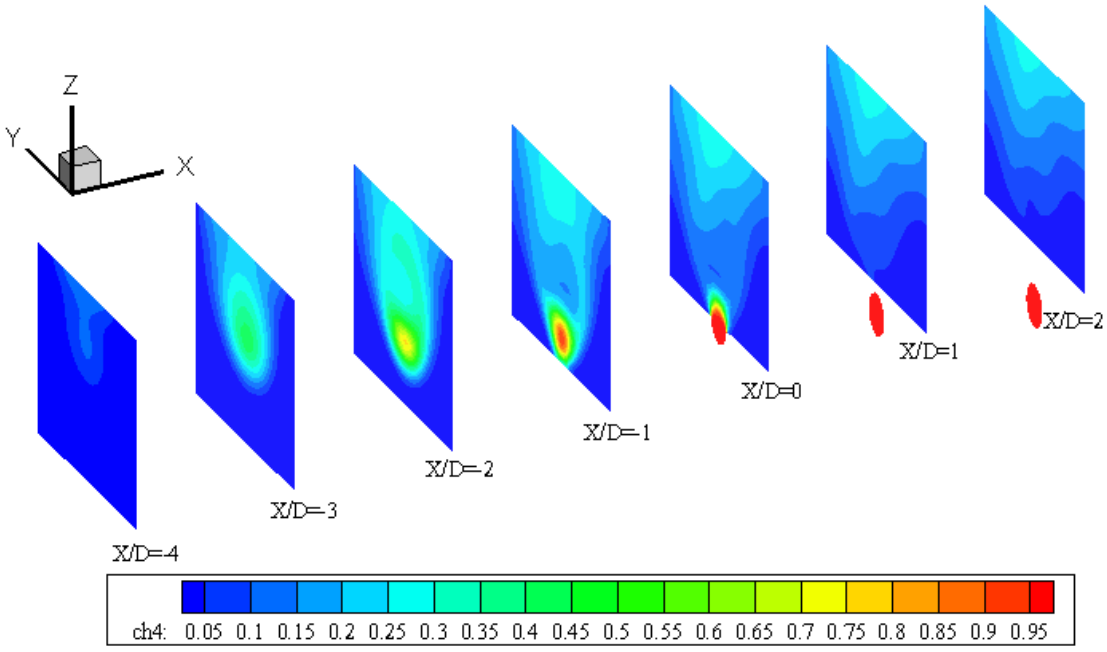

Figure 7.3-8 Mass fraction of CH_4 at different cross sections along the direction of crossflow, case Jet MCS

Same as the results from various experimental measurements, the calculated flow fields in the far downstream show that the streamwise injection can result the poorest mixing between the jet and the crossflow. For the case of normal injection and counter streamwise injection, the mixing is almost finished and the flow is close to uniform, although there are still differences between the flow fields of these two cases.

Generally speaking, these calculation results agree well with those observed by different experimental techniques. However, this model also reveals some more interesting structures in the flow field, such as the ‘band-liked’ structure appears in the mass fraction distribution results of the case Jet MS. Either they are only caused by calculation errors or they are naturally happened but not observed by the used experimental techniques needs to be studied in the future.

CHAPTER 8

CONCLUSION

The transverse injection of gas jets into a narrow square duct has been studied by schlieren imaging, time resolved point velocity measurements with LDV, turbulence measurements with HWA as well as numerical simulation, under steady conditions. The results of both the experiments measurements and numerical calculation showed the complex turbulent and three dimensional structure of the flow, induced by transverse injection. Schlieren imaging provided a powerful technique to visualize the instantaneous flow field, and has been conducted firstly to study the topology of the jets for different jet-to-crossflow momentum flux ratios, and revealed the strong effect of wall impingement on the jet for $R > 3$. Mean velocity vector plots and turbulence kinetic energy scalar fields at center plane and several cross sections were reported and analyzed in depth, based on the LDV measurements. HWA provides turbulence data at far downstream in the flow field. Moreover, the results from the numerical simulation show well agreement with the experimental results acquired, and can present the concentration field, and consequently directly show the mixing process between the jet and the crossflow.

Some remarkable and detailed results are summarized here:

- The well-known flow feature formed by the CVP has been identified in this study. When the jet is injected normally to the crossflow, the CVP starts to be formed in the very near field and persists in the far field, at least up to X/D = 10. The strong turbulence kinetic energy found in the near field of the jet suggests that maximum entrainment of crossflow happens there.

- The confinement from the duct plays a critical role in the development of flow field, particularly when R is high. It stops the transverse development of the jet, forcing it to move laterally. The mixing is greatly influenced by the confinement, since the transverse movement of CVP is also confined.
- Changing the injection orientation will change the flow pattern greatly. When the jet is injected with the same direction of the cross stream, less interaction between jet and crossflow happens, and mixing between them is very poor, until the jet impacts with the opposite wall. In the opposite case, when the jet is injected against the crossflow, strong interaction between the jet and the crossflow happens; classical structure of jet into crossflow is changed. Nonetheless, mixing is enhanced greatly and a nearly uniform flow structure is observed downstream, starting from cross section X/D=1.
- Injection of different gases has limited influence on the mean flow field if the same jet-to-crossflow momentum flux ratio is imposed.

According to the author's knowledge, this is the first study concerning gas jet injection into confined crossflow, attempting to simulate the gaseous fuel-air mixing process inside the intake port of a PFI engine using gaseous fuel. A comprehensive description of the flow pattern of jet into confined crossflow, under various injection conditions, has been obtained from the study. The main outcome is that different mixing strategies may have sensible effect on the mixture formation and the related in-cylinder combustion process and thus fuel gas injection should be optimized to improve the overall engine performance.

REFERENCES

[1] Keffer J F and Baines W D. The round turbulent jet in a cross-wind. J Fluid Mech 1963; 15: 481-496

[2] White C M, Steeper R R and Lutz A E. The hydrogen-fueled internal combustion engine: a technical review. Int J Hydrogen Energ 2006; 31: 1292-1305

[3] Korakianitis T, Namasivayam A M and Crookes R J. Natural-gas fueled spark-ignition (SI) and compression-ignition (CI) engine performance and emissions. Prog Energ Combust 2011; 37: 89-112

[4] Andreopoulos J. On the structure of jets in crossflow. J Fluid Mech 1985; 157: 163-197

[5] Margason R J. The path of a jet directed at large angles to a subsonic free stream. Report, NASA, Washington D C, TN D-4919, 1968

[6] Kamotani Y and Greber I. Experiments on a turbulent jet in a cross flow. AIAA Journal 1972; 10: 1425-1429

[7] Fric T F and Roshko A. Vortical structure in the wake of a transverse jet. J Fluid Mech 1994; 279: 1-47

[8] Kelso R M, Lim T T and Perry A E. An experimental study of round jets in cross flow. J Fluid Mech 1996; 306: 111-144

[9] Cortelezzi. L, Karagozian A R. On the formation of the counter-rotating vortex pair in transverse jets. J Fluid Mech 2001; 446: 343-373

[10]. Zhu G, Lai M C and Lee T. Penetration and mixing of radial jets in neck-down cylindrical crossflow. J Propul Power 1995; 11: 252-260

[11] Eroglu A and Breidenthal R E. Structure, penetration and mixing of pulsed jets in crossflow. AIAA Journal 2001; 39: 417-423

[12] Smith S H and Mungal M G.. Mixing structure and scaling of the jet in crossflow. J Fluid Mech 1998; 357: 83-122

[13] Lim T T, New T H and Luo S C. On the development of large-scale structures of a jet normal to a cross flow. Phys Fluids 2001; 13: 770-775

[14] Haven B A and Kurosaka M. Kidney and anti-kidney vortices in cross flow jets. J Fluid Mech 1997; 352: 27-64

[15] Trischka J W, Eskinazi S and Moussa Z M. The near field in the mixing of a round jet with a cross-stream. J Fluid Mech 1977; 80: 49-80

[16] Gopalan S, Abraham B M and Katz J. The structure of a jet in cross flow at low velocity ratios. Phys Fluids 2004; 16: 2067-2087

[17] Su L K and Mungal M G. Simultaneous measurements of scalar and velocity field evolution in turbulent crossflowing jets. J Fluid Mech 2004; 513: 1-45

[18] Meyer K E, Pedersen J M and Ozcan O. A turbulent jet in crossflow analyzed with proper orthogonal decomposition. J Fluid Mech 2007; 583: 199-227

[19] Camussi R, Guj G. and Stella A. Experimental study of a jet in a cross flow at very low Reynolds number. J Fluid Mech 2002; 454: 113-144

[20] Meyer k E, Ozcan O, Larsen P S, et al. Point and planar LIF for velocity-concentration correlation in a jet in cross flow. In “Laser Techniques for Fluid Mechanics”, 10th Intern. Symposium, Springer, 2002

[21] Carl-Jochen Winter .Hydrogen energy – Abundant, efficient, clean: A debate over the energy –system-of-change. Int J Hydrogen Energ 2009; 34: S1-S52

[22] Lapidus A I, Krylov I F and Tonkonogov B P. Current problems, natural gases motor fuel. Chem Tech Fuels Oil 2005; 41: 165-174

[23] Margason R J. "*Fifty Years of Jet in Crossflow Research*". In computational and experimental assessment of jets in cross flow, AGARD, 1993

[24] Hasselbrink E F and Mungal M G. Transverse jets and jet flames. Part 1. Scaling law for strong transverse Jets. J Fluid Mech 2001; 443: 1-25

[25] Pratte S D and Baines W D. Profiles of the round turbulent jet in a cross flow. J Hydraulics Division, ASCE 1967; 92: 53-64

[26] Broadwell J E and Breidenthal R E. Structure and mixing of a transverse jet in incompressible flow. J Fluid Mech 1984; 148: 405-12

[27] Krothapalli A, Lourenco L, and Buchlin J M. Separated flow upstream of a jet in a crossflow. AIAA Journal 1990; 28: 414-20

[28] Kelso R and Smits A. Horseshoe vortex systems resulting from the interaction between a laminar boundary layer and a transverse jet. Phys Fluids 1995; 7: 153-8

[29] Dobson G M B. Measurements of turbulence in the atmosphere by the spreading of a smoke trail. *RAE RM* No. 671, 1919

[30] Bosanquet C H and Pearson J L. The spread of smoke and gases from chimneys Transactions of the Faraday Society 1936; 32: 1249-1264

[31] Narayanan S, Barooah P and Cohen J M. Dynamics and control of an isolated jet in crossflow. AIAA Journal 2003; 41: 2316-2330

[32] Huang R F and Hsieh R H. Flow visualization and LDV measurement on near-wake of elevated jets in a crossflow. Proceeding of 4th Pacific Symposium on Flow Visualization and Image Processing, Chamonix, France, 2003

[33] Morton B R and Ibbetson A. Jets deflected in a crossflow. Exp Therm Fluid Sci 1996; 12: 112-133

[34] Gogineni S, Goss L and Roquemore M. Manipulation of a jet in a cross flow. Exp Therm Fluid Sci 1998; 16: 209-219

[35] M'Closkey, King J M , Cortelezzi L and Karagozian A R. The actively controlled jet in crossflow. J Fluid Mech 2002; 452: 325-335

[36] Coelho S L V and Hunt J C R. The dynamics of the near field of strong jets in crossflows. J Fluid Mech 1989; 200: 95-120

[37] Peterson S D and Plesniak M W. Evolution of jets emanating from short holes into crossflow. J Fluid Mech 2004; 503: 57-91

[38] Bayraktar S and Yilmax T. Experimental analysis of transverse jet using various decomposition techniques. J Mech Science & Tech 2011; 25: 1325-1333

[39] Ozcan O and Larsen P S. Laser Doppler Anemometry study of a turbulent jet in crossflow. AIAA Journal 2003; 41:1614-1616

[40] Ozcan O, Meyer K E and Larsen P S. Measurement of mean rotation and strai-rate tensors by using stereoscopic PIV. Exp Fluids 2005;39: 771-783

[41] Rivero A, Ferre J A and Giralt F. Organized motions in a jet in crossflow. J Fluid Mech 2001; 444: 117-149

[42] Gordon M and Soria J. PIV measurements of a zero-net-mass-flux jet in cross flow. Exp Fluids 2002; 33: 863-872

[43] Getsinger D R, Hendrickson C and Karagozian A R. Shear layer instabilities in low-density transverse jets. Exp Fluids 2012; 53: 783-801

[44] Megerian S, Davitian J and B Alves L S. Transverse-jet shear-layer instabilities. Part 1. Experimental studies. J Fluid Mech 2007; 593: 93-129

[45] Hasselbrink E F and Mungal M G. Transverse jets and jet flames. Part 2. Velocity and OH field imaging. J Fluid Mech 2001; 443: 27-68

[46] Fric T F. Structure in the near field of the transverse jet. PhD thesis, California Institute of Technology Pasadena, California, 1990

[47] Doligalski T L, Smith C R and Walker J D. Vortex interactions with walls. Annual Review of Fluid Mechanics, 1994; 26: 573-616

[48] Blanchard J N, Brunet Y and Merlen A. Influence of a counter rotating vortex pair on the stability of a jet in a cross flow: an experimental study by flow visualizations. Exp Fluids 1999; 26: 63-74

[49] Jendoubi S and Strykowski P J. Absolute and convective instability of axisymmetric jets with external flow. Phys Fluids 1994; 6: 3000-3010

[50] Sullivan P and Pollard A. Coherent structure identification form the analysis of hot-wire data. Meas Sci Technol 1996; 7: 1498-1516

[51] Sykes R I, Lewellen W S and Parker S F. On the vorticity dynamics of a turbulent jet in a crossflow. J Fluid Mech 1986; 168: 393-413

[52] Claus R W and Vanka S P. Multigrid calculations of a jet in crossflow. J. Propulsion Power 1990; 8: 425-431

[53] Kim S W and Benson T J. Calculation of a circular jet in crossflow with a multiple-time-scale turbulence model. Intl J Heat Mass Transfer 1992; 35: 2357-2365

[54] Demuren A O. Characteristics of three-dimensional turbulent jets in crossflow. Intl J Engng Sci 1993; 31: 899-913

[55] Yuan L L, Street R and Ferziger J H. Large-eddy simulations of a round jet in crossflow. J Fluid Mech 1999; 379: 71-104

[56] Wegner B, Huai Y and Sadiki A. Comparative study of turbulent mixing in jet in cross-flow configurations using LES. Int J Heat Fluid Fl 2004; 25: 767-775

[57] Andreopoulos J. Heat transfer measurements in a heated jet pipe flow issuing into a cold cross stream. Phys Fluids 1983; 26: 3201-3210

[58] Andreopoulos J and Rodi W. Experimental investigation of jets in a crossflow. J Fluid Mech 1984; 138: 93-127

[59] Muppidi S and Mahesh K. Study of trajectories of jets in crossflow using direct numerical simulations. J Fluid Mech 2005; 530: 81-100

[60] Muppidi S and Mahesh K. Direct numerical simulation of round turbulent jets in crossflow. J Fluid Mech 2007; 574: 59-84

[61] Cottet G H and Koumoutsakos P D. Vortex methods: theory and practice. Meas Sci Technol 2001; 12: 12-354

[62] Marzouk Y M and Ghoniem A F. Vorticity generation mechanisms and correct boundary conditions for transverse jet simulation. Second MIT Conference on Computational Fluid and Solid Mechanics, Cambridge, USA, collected in Computational Fluid and Solid Mechanics, 2003

[63] Vermeulen P J, Grabinski P and Ramesh V. Mixing of an acoustically excited air jet with a confined hot crossflow. J Eng Gas Turb Power, ASME Transactions 1992; 114: 46-54

[64] Shapiro S, King J, M'Closkey R.T, and Karagozian A R. Optimization of controlled jets in crossflow. AIAA Journal 2006; 44: 1292-1298

[65] Johari H, Pacheco T M and Hermanson J C. Penetration and mixing of fully modulated turbulent jets in crossflow. AIAA Journal 1999; 37: 842-850

[66] Schuller T, King J, Majamaki A and Karagozian A R. An experimental study of acoustically controlled gas jets in crossflow. Bulletin of the American Physical Society, 1999; 44: 111

[67] Das L M, Gulati R, and Gupta P K. A comparative evaluation of performance characteristics of a spark ignition engine using hydrogen and compressed natural gas as alternative fuels. Int. J. Hydrogen Energy 2000; 25: 783-793

[68] Bauer G G, and Forest T W, Effect of hydrogen addition on performance of methane-fueled vehicles. Part 1:effect on SI engine performance. Int J Hydrogen Energy 2001; 26: 55-70

[69] Ma F H, Liu H Q, et al. Combustion and emission characteristics of a port-injection HCNG engine under various ignition timings. Int J Hydrogen Energy 2008; 33: 816-822

[70] Homan H S. An experimental study of reciprocating internal combustion engines operated on hydrogen. Ph.D. Thesis, Cornel University, 1978

[71] Homan H S, DE Boer P C and McLean W J. The effect of fuel injection on NOx emissions and undesirable combustion for hydrogen-fuelled piston engines. Int J Hydrogen Energy 1983; 8: 131-146

[72] Wong Y K and Karim G A. An analytical examination of the effects of hydrogen addition on cyclic variations in homogeneously charged compression-ignition engines. Int J Hydrogen Energy 2000; 25: 1217-1224

[73] http://en.wikipedia.org/wiki/Schlieren

[74] Settles G S. "*Schlieren and Shadowgraph techniques*", Springer, Verlag Berlin Heidelberg NewYork, ISBN 3-540-66155-7, pp 25-65, 2001

[75] Philbert M, Surget J and Veret C. "*Shadowgraph and Schlieren*", Chap. 12 of Handbook of Flow Visualiation,. Hemisphere Pub., Washionton, ISBN 1-560-32417-1 ed. 1. pp. 189-217, 1989

[76] Goldstein R J and Kuehn T H. "*Optical systems for flow measurement – shadowgraph, schlieren, and interferometric techniques*", Chap. 8 of Fluid mechanics measurements. Springer, Verlag, Berlin, ISBN 1-56032-306-X, pp. 377-397, 1983

[77] Weinberg F J. "*Optics of flames: including methods for the study of refractive index fields in combustion and aerodynamics*". Butterworths, London, 1963

[78] Vasiliev L A. "*Schlieren methods*". Isarel Program for Scientific Translations, New York, 1971

[79] Barnes N F and Bellinger S L. Schlieren and shadowgraph equipment for air flow analysis. JOSA (Journal of the Optical Society of America), 1945; 35(8): 497-509

[80] Speak G S and Walters D J. Optical considerations and limitations of the schlieren method. ARC R&M 2859, Brithsh Aero. Research Council, 1950

[81] Ojeda-Castaneda J. Foucault, wire, and phase modulation tests, Chap. 8 of "*Optical shop Testing*". John Wiley & Sons, Inc., Hoboken, New Jersey, ISBN 978-0-471-48404-2, pp. 265-288, 1991

[82] Albrecht H E, Borys M, Damaschke N and Tropea C. "*Laser Doppler and Phase Doppler Measurement Techniques*". Springer, Verlag Berlin Heidelberg New York, ISBN 3-540-67838-7, pp. 27-78, 2003

[83] Goldstein R J and Kreid D K. Measurement of laminar flow development in a square duct using a laser-Doppler flowmeter. ASME J of Appl Mech 1967; 34:813-818

[84] Stein H D and Pfeifer H J. A Doppler difference method for velocity measurements. Metrologia 1969; 5:59-61

[85] Rudd M J. A new theoretical model for the laser Doppler meter. J Phys E Sci Instrum 1969; 2: 55-58

[86] Chang I C. Acoustooptic devices and applications. IEEE Transactions and Sonics and Ultrasonics 1976; 23:1-22

[87] Bruun H H. "*Hot-Wire Anemometry: Principles and Signal Analysis*". Oxford University Press, USA, ISBN 0198563426, 1995

[88] Lomas C G. "*Fundamentals of Hot Wire Anemometry*". Cambridge University Press, Cambridge, ISBN 0521283183, 2011

[89] Compte-Bellot G. "*Hot-wire Anemometry*". The Handbook of Fluid Dynamics edited by R.W. Johnson, Taylor & Francis, ISBN 0849325099, 1998

[90] Wilke C R. A viscosity equation for gas mixtures. J. Chem Phys 1950; 18: 517

[91] Longmire E K and Eaton J K. Structure of a particle-laden round jet. J Fluid Mech 1992; 236: 217-257

[92] Karagozian A R. Transverse jets and their control. Prog Energy Combust 2010; 36: 531-553

[93] Shih T H, Liou W W, Shabbir A, Yang Z, and Zhu J. A new eddy-viscosity model for high Reynolds number turbulent flows - Model development and validation. Computers Fluids 1995; 24(3):227-238

[94] Chorin A J. Numerical solution of Navier-Stokes equations. Math Comput 1968; 22:745-762

[95] Launder B E and Spalding D B. The Numerical Computation of Turbulent Flows. Comput Method Appl M 1974; 3:269-289